High-Precision Timing and Polarimetry of PSR J0437−4715

Willem van Straten

A Dissertation
Presented in fulfillment of the requirements
for the degree of
Doctor of Philosophy
at Swinburne University Of Technology

July 2003

Ray Stantz:	“Hey, where do these stairs go?”
Peter Venkman:	“They go up.”

— **Ghostbusters** (Reitman 1984)

Abstract

This thesis reports on the recent results of a continuing, high-precision pulsar timing project, currently focused on the nearby, binary millisecond pulsar, PSR J0437−4715. Pulse arrival time analysis has yielded a remarkable series of constraints on the physical parameters of this system and evidence for the distortion of space-time as predicted by the General Theory of Relativity.

Owing to the proximity of the PSR J0437−4715 system, relative changes in the positions of the Earth and pulsar result in both annual and secular evolution of the line of sight to the pulsar. Although the changes are miniscule, the effects on the projected orbital parameters are detectable in our data at a high level of significance, necessitating the implementation of an improved timing model.

In addition to producing estimates of astrometric parameters with unparalleled precision, the study has also yielded the first three-dimensional orbital geometry of a binary pulsar. This achievement includes the first classical determination of the orbital inclination, thereby providing the unique opportunity to verify the shape of the Shapiro delay and independently confirm a general relativistic prediction.

With a current post-fit arrival time residual RMS of 130 ns over four years, the unrivaled quality of the timing data presented herein may eventually contribute to the most stringent limit on the energy density of the proposed stochastic gravitational wave background. Continuing the quest for even greater timing precision, a detailed study of the polarimetry of PSR J0437−4715 was undertaken. This effort culminated in the development of a new, phase-coherent technique for calibrating the instrumental response of the observing system.

Observations were conducted at the Parkes 64-m radio telescope in New South Wales, Australia, using baseband recorder technologies developed at York University, Toronto, and at the California Institute of Technology. Data were processed off-line at Swinburne University using a beowulf-style cluster of high-performance workstations and custom software developed by the candidate as part of this thesis.

Acknowledgments

The work presented in this thesis composes one phase in the continuing collaboration of a dedicated group of people. Instrumentation and software have been developed, observations have been conducted, and ideas have been contributed by collaborators from Swinburne University of Technology, the California Institute of Technology, the Australia Telescope National Facility (ATNF), and the Space Geodynamics Laboratory (SGL) at York University, Toronto. Although most of my contribution to the research was completed while living in Melbourne, the majority of this dissertation was written upon my return to Canada. Throughout this time, I relied quite heavily on the support of my family and friends on both continents. There are many people whom I wish to thank.

The major component of the motivation and direction in this work derives from the ambitious vision of my supervisor, Matthew Bailes. His infectious enthusiasm and encyclopedic knowledge on the subject of pulsars has proved invaluable over the past five years. I thank Matthew for his patience, tolerance, and guidance that left ample room for me to chase the questions and problems that captured my attention and imagination.

I would also like to thank Matthew Britton for being my co-supervisor, mentor, and friend. Matthew's interests, knowledge, and ability span a variety of subjects. With kind words of cogent advice, he encouraged me to branch out in a number of different directions and endured my most ignorant questions. Matthew and his wife, Downapha, always shared warmly of their hospitality, especially during their wedding in Khanom and later in Pasadena.

My colleagues and friends from the Swinburne pulsar group also greatly enriched my experience in Australia. Russell Edwards is a most imaginative and intellectual collaborator and friend. Maurizio Toscano combines scholarly eloquence with devilish mischievousness. Stephen Ord and I have shared many casual, philosophical, and technical discussions, both on the long road to Parkes and at the pub. I am grateful to everyone for trading ideas and opinions on everything from object-oriented programming to Zen Bhuddism, and for helping to maintain a healthy balance of sanity and lunacy during the many long days and late nights at the telescope.

Before I left for Australia, I spent a month at Caltech, during which time Stuart Anderson and Rick Jenet introduced me to pulsar data reduction and massively parallel computing. I am particularly grateful to Stuart for his detailed lessons on the various technical and conceptual aspects of observing. As the principal developers of the Caltech Parkes Swinburne Recorder (CPSR), he and John Yamasaki made the long haul to Parkes to install CPSR and have continued to provide technical support and consultation on the timing project. Bryan Jacoby also made the trip to share in both observing runs and fun in Melbourne. I am particularly indebted to Shri Kulkarni for volunteering expert advice during the preparation of my first paper.

Dick Manchester provided an experienced perspective throughout this work. In addition to sharing scientific counsel, proof reading, and organizing regular teleconferences with the Australian pulsar astronomy community, Dick pioneered the transfer of our timing analysis and archival software to the linux operating system. This work greatly eased the transition when the new Dell workstation cluster was purchased at Swinburne. I am grateful to Simon Johnston for the opportunity to collaborate with him and Michael Kramer on the single-pulse polarization studies of the Vela pulsar. Simon's energetic influence and our discussions on radio polarimetry stimulated my growing interest in the subject. I also wish to thank to my thesis referees, Jim Cordes and Don Backer. Your insightful commentary and criticism is greatly appreciated.

The observations described in this thesis would not have been possible without the excellent support of the Parkes Observatory staff. John Reynolds was always quick to respond to questions, offer support, consultation, and assistance, and to organize maintenance when required. Under his direction, the reliability of the facility steadily and noticeably improved. The accuracy of our timing data is in large part due to the careful attention paid by Brett Preisig to the monitoring of the Parkes Hydrogen maser. In addition to providing general technical and engineering support, Harry Fagg instructed me on the calibration of the CPSR sampling clock phase. Gina Spratt maintained the various computing resources that we required during our observing runs, which were made much more pleasant by the friendly hospitality of Janette Cole and Shirley Ingram. I would especially like to thank John Sarkissian for managing and conducting the regular observations of PSR J0437−4715 from which a significant portion of the data presented in this thesis are derived. His enthusiasm and dedication to the project surpass all expectations and is greatly appreciated. The Parkes Observatory is part of the Australia Telescope which is funded by the Commonwealth of Australia for operation as a National Facility managed by CSIRO.

My first three and a half years of study were funded by the Commonwealth Scholarship and Fellowship Plan, administered by IDP Education Australia. Swinburne University provided much needed financial assistance in 2001.

I've been exceedingly fortunate to have lived with excellent people during my time in Melbourne. For madness and inspiration, I thank my housemates, dear friends, and warlords of space rock, Josh Beagley and Steve Brick. For his steadfast friendship and straight-up advice, I thank Simon Danckert; our weekends in Aries Inlet were a great source of renewed vitality. Thanks also to Dave Walker, Georgia Halliday, and Lucy Sullivan for simply being awesome housemates and friends, and to Meaghan Walsh for her generous kindness and support.

On returning home to write up this dissertation, I found new strength in my old circle of friends. Thank you, Jeffrey Buchanan, for reminding me about who we aim to be, and for helping me to find part-time employment in Sarnia. I especially wish to thank my brothers, Adam and Joel, for keeping it real. Also, thanks for lending me your computer, Joel. I am fortunate to have always known the love and support of my parents, Hinke and Willem. Thank you for your encouragement and patience over all these years. The final revisions on this work were completed while living in Groningen with my closest and dearest friend and loving partner, Asha Rawlings.

Declaration

This thesis contains no material that has been accepted for the award of any other degree or diploma. To the best of my knowledge, this thesis contains no material previously published or written by another author, except where due reference is made in the text of the thesis. All work presented is primarily that of the author. Matthew Bailes took part in the planning, supervision, and execution of the pulsar timing observations and data analysis presented herein. He also designed and managed the facilities without which this work would not be possible and provided guidance and suggestions for the content and editing of all related publications. Beginning in May 2000, John Sarkissian, Gina Spratt, and Harry Fagg performed regular timing observations of PSR J0437−4715. Russell Edwards, Matthew Britton, Stephen Ord, and Maurizio Toscano also assisted with observations made during regularly scheduled sessions. The original baseband data reduction software was developed by Josh Kempner, Dan Stinebring, Maurizio Toscano, Matthew Bailes, and Matthew Britton. Dick Manchester, Russell Edwards, and Craig West have also made contributions to the body of software used in this thesis.

Willem van Straten

28 November, 2003

Contents

List of Figures

List of Tables

Chapter 1

Introduction

1.1 Pulsars

Since their discovery in 1967 (Hewish et al. 1968), pulsars have continued to challenge and fascinate both observers and theorists alike. They were originally dubbed LGM, or "Little Green Men", by the astronomers who happened upon a remarkable, regularly-pulsed radio signal from space. And although the association with extraterrestrial intelligence was promptly discounted, perhaps the accepted physical explanation is no less exotic. For it was soon proposed that the pulsating radio signal originated from a rapidly spinning, highly magnetized neutron star, born during a cataclysmic supernova explosion (Gold 1968).

The existence of neutron stars had been hypothesized more than 30 years before the discovery of the pulsar (Baade & Zwicky 1934) as one possible state that a star may assume at the end of its main-sequence lifetime. Having spent its nuclear fuel of lighter elements, the outward radiation pressure driven by the release of fusion energy ceases to support the stellar material against contraction under the force of gravity. Depending upon its initial mass, the exhausted progenitor star will end in one of three degenerate states: a white dwarf; a neutron star; or a black hole.

The gravitational contraction of a stellar core smaller than the Chandrasekhar (1931) limit of approximately 1.4 solar masses ($M_\odot$) results in the formation of a white dwarf. Though the heat produced during collapse is not sufficient to ignite further nuclear fusion, the atoms in the star will become completely ionized. The Fermi pressure of the degenerate electron gas increases rapidly and opposes further gravitational contraction, resulting in an approximately Earth-sized object, a white dwarf. As it radiates away its residual thermal energy, the white dwarf will gradually cool and fade out of sight. Its ionic constituents will depend largely upon both its initial mass and evolutionary history. For instance, in a binary system, the progenitor may be disrupted by Roche lobe overflow and sustained mass loss to its more compact companion. With insufficient core density to initiate helium fusion to carbon, the resulting low-mass white dwarf will be primarily composed of degenerate helium.

In those stars with a core mass of approximately 1.4 – 3 $M_\odot$, the electron degeneracy pressure does not grow as quickly as the inward pressure due to gravity. As the electrons are confined to an increasingly small space, their kinetic energies become sufficient to initiate inverse beta decay. Each electron fuses with a proton in the ionic nuclei, producing a neutron and electron neutrino. The neutrinos stream out of the core, carrying thermal energy away from the star and thereby accelerating the rate of gravitational collapse and inverse beta decay. When the core density surpasses the neutron drip point ($\sim 4.3 \times 10^{11}$ g cm^{-3}), the Fermi energies of the neutrons exceed the strong nuclear force and they begin to occupy continuum states (Baym, Pethick & Sutherland 1971). The free neutrons form Cooper pairs and, when the star cools below the neutron degeneracy temperature, undergo Bose condensation to enter a neutron superfluid phase.

Approximately 20 km in diameter, the resulting neutron star achieves a density of about 10^{14} g cm^{-3}, greater than that of the atomic nucleus. However, it has been proposed that matter may exist at even higher densities. Strange matter, a self-bound plasma of up, down, and strange quarks, may be the ground state of the hadrons (Itoh 1970). Based on this conjecture, evolutionary arguments have been presented for the existence of both neutron stars with quark interiors, known as quark stars, and stars completely composed of stable quark matter, known as strange stars (Alcock, Farhi & Olinto 1986; Belczynski, Bulik & Kluźniak 2002). However, as the existence of strange matter remains purely hypothetical, the neutron star continues to be the most favoured basis for pulsar models.

The compactness of a neutron star is given by $\mathcal{C} \equiv Gm/Rc^2 \sim 0.2$, where m and R are the star's mass and radius, respectively. Relative to objects such as the Sun ($\mathcal{C}_\odot \sim 2 \times 10^{-6}$) the compactness of a neutron star is close to the theoretical maximum of 0.5, corresponding to that of a black hole. These are created in the supernova implosion of a stellar core with mass greater than ~ 3 $M_\odot$, during which gravity overwhelms even the neutron degeneracy pressure and the star collapses into a singularity behind an event horizon. Extreme phenomenon such as black holes and neutron stars were considered to be not much more than mere theoretical fancy before the discovery of the radio pulsar. The pulsar therefore provided the first direct observation into the realm of nature described by the equation of state of super-dense matter and the non-linear, strong-field regime of general relativity.

Like a celestial radio lighthouse, a pulsar generates a narrowly focused beam of radio emission at the poles of its powerful magnetic field. The magnetic axis is not necessarily aligned with the spin axis, and the beam traces out a cone with every rotation of the neutron star. As observed from Earth, the intensity of the pulsar's emission peaks every time the beam swings around to face us. The period between pulse peaks, P, is therefore equal to the spin period of the underlying neutron star. Assuming that magnetic dipole radiation is primarily responsible for the loss of rotational energy, measurement of the rate at which the pulsar spins down permits an estimate of the magnetic field strength, which can be as high as 10^{13} Gauss (cf. the average geomagnetic field strength of 1 G). From the extremely high brightness temperature, $T \sim 10^{25}$ Kelvin (K), of the observed radiation it has been inferred that a coherent plasma process must be responsible for the emission (Melrose 1992), a conjecture supported by the recent detection of coherent emission from pulsars (Jenet, Anderson & Prince 2001b).

Although the precise mechanism by which the radio emission is generated remains in debate, the pulsar magnetosphere is generally believed to contain a dense corotating plasma (Goldreich & Julian 1969) composed primarily of ultra-relativistic electrons and positrons generated by pair cascade (Sturrock 1971; Daugherty & Harding 1982). Similar to the best vacuum that may be obtained with laboratory ion pumps, the charged particle density in the pulsar magnetosphere ($\sim 10^{11}\mathrm{cm}^{-3}$) is about one billion times that found in the Earth's inner plasmasphere. These particles remain trapped on closed magnetic field lines and corotate with the pulsar out to the light cylinder radius, the distance from the neutron star spin axis, $r_{\rm lc}$, at which the rotational velocity, $2\pi r_{\rm lc}/P$, equals the speed of light, c. Beyond the light cylinder, closed magnetic field lines cannot be causally maintained and the plasma escapes in a relativistic magnetohydrodynamic (MHD) wind. This wind is believed to consist of electrons, positrons, and possibly ions, which emit coherent curvature, synchrotron and/or cyclotron radiation as they are accelerated along the open field lines which spiral away from the poles (Ruderman & Sutherland 1975; Cheng & Ruderman 1980). The outward flow of relativistic particles may shock the cold interstellar medium (ISM), resulting in collisional excitation of the hydrogen surrounding the pulsar. The Hα nebula generated by this interaction is known as a pulsar wind nebula (PWN) (Kulkarni & Hester 1988). Conversely, the inward flow of relativistic particles from the acceleration zones may impact upon the polar caps of the neutron star surface, heating these regions up to X-ray temperatures (Arons 1981; Hibschman & Arons 2001; Zavlin et al. 2002).

Interestingly, this description of the pulsar magnetospheric polar region as an ultra-relativistic cosmic particle accelerator may also provide the answer to another outstanding problem in astrophysics. Since the mid-1990s, numerous detections of ultra-high energy cosmic ray (UHECR) events have continued to challenge the notion that cosmic rays are of extragalactic origin. Cosmic rays are the most energetic particles in the universe and are detected by the giant airshowers of secondary particles created when they collide with the Earth's atmosphere. Although their origin and nature is currently unknown, it is expected that a cosmic ray proton with energy greater than $\sim 5 \times 10^{19}$ eV ($\sim$ 8 Joules!) will lose energy by interacting with the cosmic microwave background through photopion production. Consequently, it is believed that UHECR must originate within a $\sim$ 50 Mpc radius, and it has been proposed that neutron stars may be their mysterious source. Most recently, Blasi, Epstein & Olinto (2000) have suggested that UHECR might be iron nuclei stripped from young, highly magnetized neutron stars and accelerated to ultra-high energies by the pulsar's relativistic MHD wind. Another model has been presented in which protons are accelerated in magnetic reconnection sites outside of the magnetospheres of young millisecond pulsars born during the accretion-induced collapse of a white dwarf (de Gouveia Dal Pino & Lazarian 2000). Recent observations of the pulsar wind nebula surrounding PSR B1509-58 made with the Chandra X-Ray Observatory (Gaensler et al. 2002) lend credence to the candidacy of young pulsars as the energetic sources of ultra-relativistic particles raining down on Earth.

1.2 Pulsar Timing

Some fundamental questions remain about the nature of the pulsar, its internal structure, and the complex physics taking place in its magnetosphere and surrounding environment. For these reasons alone, pulsars remain an intrinsically interesting field of study. However, pulsars have also been shown to have exceptional long-term rotational stability (Kaspi, Taylor & Ryba 1994, see also Figure 6.4), allowing the clockwork nature of the pulsed radio emission to be utilized as a unique astrophysical probe. Like a formidable celestial flywheel, the pulsar's rotational stability derives from its huge moment of inertia. During the gravitational collapse of the progenitor stellar core, a large fraction of its angular momentum is conserved, producing a neutron star with an initial spin period of the order of tens of milliseconds. Rotational energy is gradually lost to magnetic dipole/multipole radiation and the radial outflow of the pulsar MHD wind, which carries away angular momentum. These contributions to the spin-down torque on the neutron star result in a population of pulsars normally found with spin periods ranging from ~ 33 ms to ~ 3 s, with the slowest pulsar known at $P \sim 8.5$ s (Young, Manchester & Johnston 1999).

The fastest pulsar ever discovered, with a spin period of ~ 1.6 ms (Backer et al. 1982), is also the first to be recognized as belonging to a special class of pulsars, known as the millisecond pulsars (MSP). The MSP population differs from the "normal" population in a number of ways (see Figure 1.1). Normal pulsars have period derivatives of the order of 10^{-14} to 10^{-16}, from which may be inferred surface magnetic field strengths of $\sim 10^{12}$ G and characteristic spin-down ages of the order of Megayears. MSPs, on the other hand, have smaller period derivatives, $\sim 10^{-19}$ to 10^{-20}, much weaker surface magnetic field strengths, $\sim 10^{8}$ G, and spin-down ages of the order of Gigayears.

Due to these primary observational differences, millisecond pulsars are thought to be the result of a unique evolutionary process. It is believed that they are spun up to their rapid rotation rates by the accretion of matter and angular momentum from a binary companion (Smarr & Blandford 1976; Alpar et al. 1982). This conjecture is well-supported by the large percentage of MSPs found in binary systems (see Figure 1.1), many of which contain a low-mass companion such as a white dwarf. However, it remains in question whether the accretion episode occurs before or after the supernova explosion during which the neutron star is formed. In one model, a normal pulsar lives out its life with a main sequence companion, which eventually expands beyond its Roche lobe and transfers some fraction of its mass to the neutron star, spinning it up. In light of this probable evolutionary history, MSPs are suitably

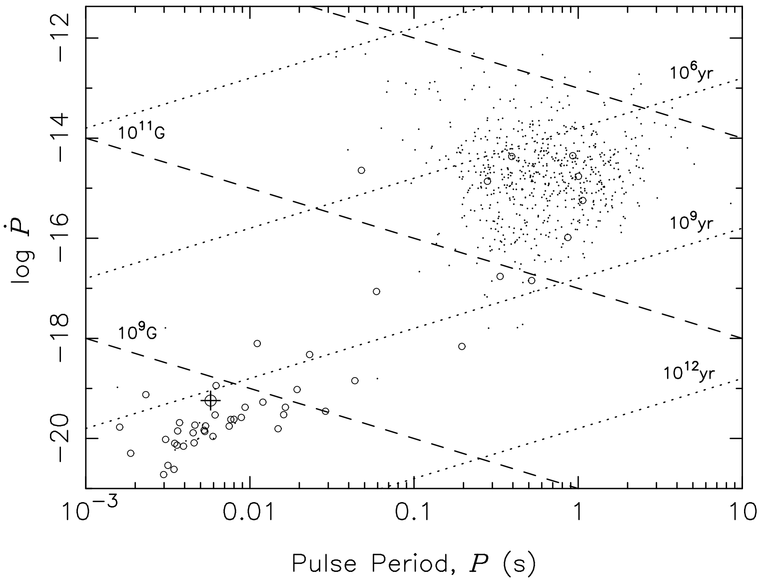

Figure 1.1: The above distribution of pulse period, P, versus $\dot{P}$ demonstrates the distinction between "normal" (upper right) and "millisecond" (bottom left) pulsar populations. A total of 702 pulsars are plotted, out of which 46 are found in a binary system, as shown using a circle. Note the large fraction of millisecond pulsars found binary systems. The millisecond pulsar, PSR J0437−4715, is marked with a target symbol. Dotted lines plot constant characteristic spin-down age, $\tau_c = P/2\dot{P}$, and dashed lines plot constant surface magnetic field strength.

known as recycled pulsars. In the accretion-induced collapse model, a white dwarf is found in a binary system with a main sequence companion. The accretion process tips the white dwarf mass over the Chandresekhar limit, the white dwarf implodes and a millisecond pulsar is born. Regardless of the exact formation scenario, it has been suggested that the low inferred magnetic field strengths of MSPs may be a consequence of magnetic field burial during the accretion episode (Taam & van den Heuvel 1986).

The long-term rotational stability of millisecond pulsars has been shown to be comparable to the best atomic time standards here on Earth (Taylor 1991; Kaspi, Taylor & Ryba 1994). The observed radio signal may therefore be treated as a highly accurate astrophysical frequency standard. The shape of the observed radio intensity as a function of pulse phase is known as the pulse profile. Although this profile generally fluctuates considerably from pulse to pulse, an average profile may be formed by integrating the received pulse train modulo the apparent topocentric pulsar spin period; a process known as folding. When folded over a few hundred pulses, the average profile is generally quite stable (Helfand, Manchester & Taylor 1975; Rankin & Rathnasree 1995). By integrating over long periods of time, the effects of system noise may be diminished to produce a standard profile with a high signal-to-noise ratio (S/N). The phase of any given pulse train relative to the epoch of its observation may be determined by fitting the average profile to the high S/N

standard, yielding an estimate of the pulse time of arrival (TOA) in the reference frame of the observatory (see Section 3.1). The TOA is the fundamental datum in an experimental treatment known as pulsar timing.

A wealth of astrophysical information has been derived from pulsar timing, a technique that is primarily sensitive to changes in the observatory–pulsar line of sight. For instance, the first extrasolar planetary system was discovered around the pulsar, PSR B1257+12, by detecting its wobble about the system's centre of mass (Wolszczan & Frail 1992). Similarly, the motion of the Earth around the Sun induces Doppler variations of pulse TOA that depend strongly on the direction to the pulsar in the sky. These variations have been modeled and utilized for the purposes of precision astrometry, first yielding estimates of pulsar position (Manchester & Peters 1972) and proper motion (Manchester, Taylor & Van 1974). Accurate position estimates are necessary in order to identify the pulsar at other wavelengths, such as optical or X-ray, and measurements of pulsar proper motion and spin-down age have been used to associate pulsars with the supernova remnants of their birth events (see Caraveo (1993) for a comprehensive review). Although the pulsar may currently lie at some distance from the centre of the nebula, the inferred associations help to support the currently accepted model of pulsar formation.

The distance to a pulsar may be estimated using a variety of techniques. One method is based upon the determination of the total column density of free electrons along the line of sight to the pulsar, known as the dispersion measure (DM). The group velocity of radio waves propagating through the dispersive ISM varies as a function of frequency and, consequently, the pulsed emission from higher frequencies will arrive earlier than that from lower frequencies. The time delay depends on the difference between the observing frequencies, the distance to the pulsar, d, and the density of free electrons along the line of sight, n_e. Both d and n_e are related to the DM by the integral,

$$DM = \int_0^d n_e dl. \tag{1.1}$$

The DM may be measured from TOA estimates taken at different observing frequencies and, using a model of the Galactic free electron density (Taylor & Cordes 1993), the distance to the pulsar may be estimated. Alternatively, a model-independent distance estimate may be derived from the annual trigonometric parallax of the pulsar, which was first successfully measured using Very Long Baseline Interferometry (VLBI) (Gwinn et al. 1986; Bailes et al. 1990) and later accomplished by the high-precision timing of an MSP (Ryba & Taylor 1991). Using the parallax distance, the average density of free electrons along the line of sight to the pulsar may be estimated and used to restrict the model of the ISM. Pulsar distances also constrain estimates of their birth-rate and, when combined with a determination of proper motion, can be used to estimate the space velocity of the pulsar perpendicular to the line of sight. These velocity estimates contribute to our understanding of the pulsar natal kick, a recoil suggested to arise from asymmetry in the supernova explosions from which they originate. In binary pulsar systems, space velocities may also help to differentiate between recycled pulsar and accretion-induced collapse scenarios of millisecond pulsar formation (Tauris & Bailes 1996).

1.3 Pulsar Polarimetry

The radio emission from pulsars typically contains a large fraction of polarized radiation. Thus, pulsar polarimetry provides insight into the magnetic field geometry and the nature of the emission mechanism. For instance, in slow pulsars the position angle, ψ, of the linearly polarized component generally follows a nearly S-shaped curve as a function of pulse phase, leading Radhakrishnan & Cooke (1969) to develop the rotating vector model (RVM) of the pulsar dipole magnetic field. In this model, ψ is expected to vary as (Manchester & Taylor 1977),

$$\tan(\psi - \psi_0) = \frac{\sin\alpha\sin\phi}{\sin\zeta\cos\alpha - \cos\zeta\sin\alpha\cos\phi}, \tag{1.2}$$

where ψ_0 is a reference position angle, ζ is the angle between the rotation axis and the line of sight, α is the angle between the magnetic and rotation axes, and ϕ is the pulsar rotational longitude with respect to the magnetic meridian. This model has proven quite successful in describing the observed position angle sweep of slow pulsars, enabling the characterization of the magnetic field orientation with respect to both the spin axis and the line of sight from Earth. Sharp discontinuities in the S-shaped flow of position angle variation have been attributed to transitions in the dominance of orthogonal modes of emission (Stinebring et al. 1984).

Following the regular occurrence of double and triple component profiles, components of the pulse profiles of slow pulsars are often classified as either core or conal (Rankin 1983a; Lyne & Manchester 1988). The central, core component typically has a high fraction of circular polarization, which may also reverse sense across the component. In slow pulsars, the core component generally has a steeper spectral index than the conal emission region, leading to noticeable changes in pulse morphology as a function of observing frequency. Millisecond pulsars have more complex polarimetric profiles that are not well-described by the RVM, suggesting the existence of multipole magnetic field structure in the emission region (Thorsett & Stinebring 1990; Xilouris et al. 1998).

Pulsar polarimetry can also provide information about the nature of the Galactic magnetic field. The tenuous, magnetized plasma of the ISM induces frequency-dependent Faraday rotation of the position angle, ψ. The change in position angle is given by $\Delta\psi = RM\lambda^2$, where λ is the wavelength of the radiation and RM is the rotation measure, given by the integral,

$$RM = \frac{e^3}{2\pi m_e^2 c^4}\int_0^d n_e B_{||} dl. \tag{1.3}$$

Here, e and m_e are the electron charge and mass, respectively, and $B_{||}$ is the component of the Galactic magnetic field parallel to the line of sight. Measurements of the position angle of a source at different observing frequencies enable determination of the RM. Combined with a DM estimate, the RM can be used to ascertain $\langle B_{||} \rangle$, the average strength of the Galactic magnetic field component along the line of sight to the pulsar.

1.4 Tests of General Relativity

The first pulsar found in a binary system, PSR B1913+16 (Hulse & Taylor 1975), also happens to exist in one of the most relativistic systems ever discovered. Through pulsar timing, Taylor & Weisberg (1982) were able to model the dynamics of this double neutron-star binary pair and demonstrate that the orbital period is decreasing as predicted by the General Theory of Relativity (GR). Their measurement of the orbital decay provided the first indirect proof of the existence of gravitational waves and is considered to be a major milestone in the verification of Einstein's theory of gravity.

Einstein first demonstrated the validity of his theory with its proposal in 1915, when he correctly derived the rate of Mercury's perihelion advance. The semi-major axis of the orbital ellipse traced by Mercury precesses around the Sun by approximately 44 seconds of arc per century, a phenomenon which remains unexplained by Newton's theory of gravity. The same precession is seen much more dramatically in the PSR B1913+16 system, where the the rate of periastron advance is approximately 4.2 degrees per year.

The General Theory of Relativity was also used to predict the apparent bending of light in a gravitational field, a phenomenon first observed by Sir Arthur Eddington (1919). Eddington traveled to Principe Island, off the coast of West Africa, to observe the positions of the stars in the Hyades cluster as the Sun passed near the line of sight to them during a solar eclipse. The measured deviations of the stellar positions proved to be in accordance with Einstein's prediction, and the young scientist gained considerable overnight fame.

Einstein also predicted that the passage of time depends upon the strength of the gravitational field in which it is measured. That is, a clock in the curved space near a massive object will run more slowly than a clock in flat, or empty, space. One consequence of this time dilation is that light will be red-shifted as it climbs out of a gravitational potential. For example, if light starts at the surface of the Earth and travels outward to a greater height, it will be found to have a lower frequency and, correspondingly, lower energy than it had upon emission. This effect was first observed by Pound & Rebka, Jr. (1960). They fired very high energy gamma-rays from radioactive iron (Fe^{57}) up the 21.6 m elevator shaft in the Jefferson Tower Physics Building at Harvard University. At the top of the shaft, similar iron nuclei were used to absorb the gamma-rays. However, as predicted, the gamma-rays at the top of the shaft had a (slightly) lower frequency than the natural frequency of the absorbing Fe^{57} atoms, and the efficiency of absorption was decreased. By moving the iron absorber with the appropriate velocity, the Doppler shifted gamma-rays were observed to be more readily absorbed, and the scientists were able to show that the fractional change in the gamma-ray frequency was within 10 percent of the general relativistic prediction. Gravitational time dilation also affects the pulsar "clock" as it climbs in and out of the potential of its companion. This effect is most readily detected when the companion is massive and the eccentricity of the orbital ellipse is high, so that the distance between the pulsar and its companion changes significantly during one orbit.

Soon after the first gravitational red-shift experiment, Shapiro (1964) used Einstein's theory to show that the speed of light also depends upon the strength of the gravitational field through which it is propagating. That is, light travels faster through flat space than it does through the curved space near a massive object. The amount by which the light is retarded depends on both the mass of the gravitating object and the distance to the object. Only four years later, Shapiro et al. (1968) demonstrated this phenomenon by bouncing radar signals off Mercury and Venus and measuring the change in transit time as the line of sight between these planets and the Earth passed near the Sun. An additional delay was detected and shown to vary as predicted by Shapiro using the General Theory of Relativity. Accordingly, this retardation is known as the Shapiro delay.

On its way to Earth, the signal from a pulsar may be retarded by the gravitating mass of its companion. This Shapiro delay varies with binary phase as the distance between the companion and the line of sight between the pulsar and the Earth changes. In a highly-inclined system, the line of sight passes near to the companion at superior conjunction, and the Shapiro delay increases sharply. In less inclined systems, the change in Shapiro delay is more gradual. The functional form, or "shape", of the Shapiro delay is therefore related to the inclination of the orbit, and its peak-to-peak magnitude, or "range", is determined by the companion mass.

The masses of the pulsar and its companion often remain poorly constrained due to the unknown orbital inclination angle (see the discussion regarding the mass function in Section 3.2). However, where two or more general relativistic effects can be measured, the component masses of the binary system may be determined. High-precision pulsar timing has yielded a limited number of such measurements. For instance, the rate of periastron advance, $\dot{\omega}$, and the time dilation and gravitational redshift, γ, have been measured in the PSR B1913+16 (Taylor & Weisberg 1982), PSR B1534+12 (Wolszczan 1991), and PSR B2127+11C (Deich & Kulkarni 1996) systems. There have also been two significant detections of the Shapiro delay in the highly inclined neutron star–white dwarf binary system, PSR B1855+09 (Ryba & Taylor 1991) and the double neutron star system, PSR B1534+12 (Stairs et al. 1998). In systems with a low-mass companion, especially those with less inclined, nearly circular orbits, the shape, $s \equiv \sin i$, and range, $r \equiv Gm_2/c^3$, of the Shapiro delay become degenerate with the Keplerian orbital parameters. For this reason, an attempt at measuring this effect in the PSR J1713+0747 system provided only weak, one-sided limits on these parameters (Camilo, Foster & Wolszczan 1994).

In many of these cases, GR has been assumed correct and utilized in order to determine or limit the component masses of the binary system. Population statistics of neutron star mass determinations aid in the development of plausible pulsar formation scenarios, and also provide insight into the evolution of binary systems (Bhattacharya & van den Heuvel 1991; Thorsett & Chakrabarty 1999). Mass estimates may also be used to constrain the poorly understood equation of state of the extremely dense neutron star matter (Lattimer & Prakash 2001). Where more than two general relativistic effects can be measured, as in the PSR B1913+16 and PSR B1534+12 systems, the set of equations describing the system is over-determined. In this case, the gravitational theory used to derive the equation set may be tested for self-consistency. By this means, the PSR B1913+16 and PSR B1534+12 timing experiments have provided the most rigorous proofs of the self-consistency of GR in the strong-field regime. However, no independent means of determining either the orbital geometry or the component masses is available in either of these experiments.

Independent verification may be obtained by determining the orientation of a binary pulsar system using only classical geometric constraints. Sections 3.2 and 4 describe such an alternative means in which the orbital inclination angle is ascertained by utilizing purely kinematic and geometric effects. This classical determination of the orbital inclination permits an independent prediction of the shape of the Shapiro delay and a unique test of GR. Combined with a significant detection of the Shapiro delay, the technique may also be used to estimate the component masses in the binary system. This method is applied to the nearby binary millisecond pulsar, PSR J0437−4715.

1.5 PSR J0437−4715

Discovered in the Parkes 70cm survey (Johnston et al. 1993; Manchester et al. 1996), PSR J0437−4715 remains the closest and brightest millisecond pulsar known. It is also the first MSP to have its X-ray emission detected and studied in detail (Becker & Trümper 1993). A number of properties make this pulsar an excellent candidate for high-precision timing. Owing to its relative proximity and correspondingly small dispersion measure ($DM \sim 2.65\,\mathrm{pc\,cm^{-3}}$), random fluctuations of electron density along the line of sight will be comparatively small (Backer et al. 1993). Therefore, the contribution of turbulence in the ISM to the arrival time residual noise of this pulsar is expected to be small (see Section 6.1.2). In addition, the narrow main peak of the total intensity profile (see Figure 1.2), short spin period ($\sim$ 5.75 ms), and relatively high flux ($\sim$ 90 mJy at 1.4 GHz) of this pulsar combine to yield highly accurate arrival time estimates from modest integration lengths (see Section 3.1).

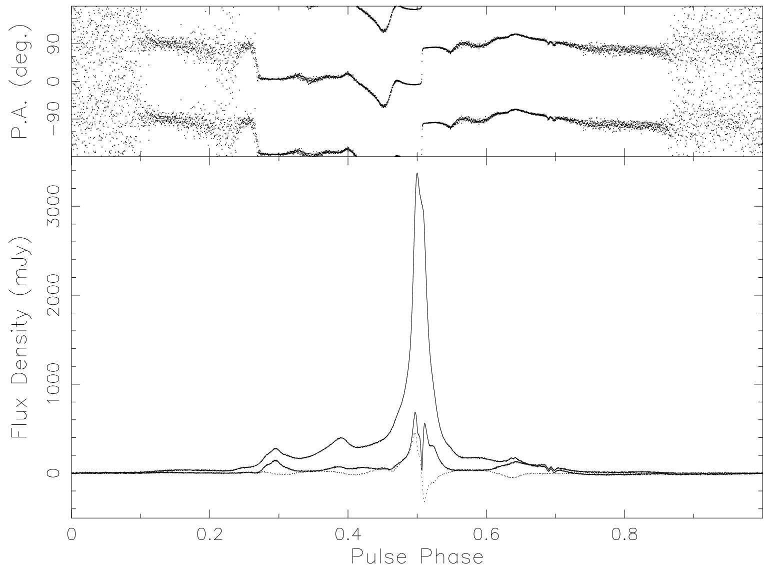

Figure 1.2: Mean polarimetric pulse profile of PSR J0437−4715 at 1510 MHz. The bottom panel displays the total intensity, Stokes I (upper solid line), the linearly polarized component, L (lower solid line), and the circularly polarized component, Stokes V (dotted line). The position angle, ψ, is shown in the upper panel.

However, this is only part of the story. As discussed in Section 5.2, the polarized component of the pulsed emission can distort the total intensity profile and systematically alter arrival time estimates. Although this mixing is invertible with precision polarimetric calibration, this has proven to be a non-trivial and elusive goal. The large swings in both position angle and the sense of circular polarization near the peak of PSR J0437−4715's central pulse (see Figure 1.2) therefore present a significant challenge. This problem has provided the main impetus behind the development of new calibration techniques (Britton et al. 2000) and sophisticated theoretical representations of the propagation and reception of electromagnetic radiation (Britton 2000). In light of both its precision timing potential and its polarimetric pathology, this thesis is devoted entirely to the study of this unique pulsar.

Optical observations indicate that PSR J0437−4715 is most likely bound to a low-mass helium white dwarf companion (Bell, Bailes & Bessell 1993; Danziger, Baade & Della Valle 1993; Bailyn 1993). The orbit is nearly circular and, as shown in Section 3.3, general relativistic contributions to the evolution of the binary system are negligible. However, owing to the relative proximity and large proper motion of the system, variations of the apparent orbital parameters are dominated by three main kinematic effects. The heliocentric orbit of the earth induces periodic variations of both the projected semi-major axis, x, and longitude of periastron, ω, an effect known as the annual-orbital parallax (Kopeikin 1995). In addition, secular evolution of x and ω (Kopeikin 1996) and an apparent orbital period derivative (Damour & Taylor 1991) arise from the system's large proper motion, μ.

A first estimate of μ was made by pulse time of arrival analysis of filter bank data (Bell et al. 1995). The pulsar proper motion compared well with that derived by optical observations of the white dwarf companion (Danziger, Baade & Della Valle 1993), further strengthening the argument for the binary association. With a post-fit arrival time residual root-mean-square (RMS) of σ_τ=2.7 μs, the Bell et al. result also confirmed the existence of a bow-shock PWN in the direction of the pulsar proper motion. This nebula was later imaged and modeled by Fruchter (1995); who suggested that the pulsar's velocity may be oriented out of the plane of the sky at an angle of approximately 37 degrees. Bell & Bailes (1996) note that the proper motion contribution to orbital period derivative dominates over those terms arising from general relativity, acceleration in the galactic potential, and galactic differential rotation, permitting an independent distance estimate, d_β (see Section 3.3.2). They anticipate that the accuracy of d_β will improve with time as $t^{2.5}$ and will, for PSR J0437−4715, surpass that derived from the annual trigonometric parallax in approximately five years (Bell & Bailes 1996). Sandhu et al. (1997) first determined the annual parallax, π, and an improved estimate of μ through TOA analysis of data from the Caltech autocorrelation spectrometer (FPTM). Noting the negligibility of any relativistic contribution, Sandhu et al. also used the proper motion contribution to $\dot{x}$ to set an upper limit on the orbital inclination, $i < 43°$. Despite a factor of five decrease in σ_τ to 500 ns, it was recognized that the accuracy of the analysis was limited by:

1. residual dispersion smearing in each frequency channel;

2. incomplete correction of digitization artifacts; and

3. polarization calibration errors.

In order to fully appreciate the significance of these three main areas of concern, it will prove useful to review both the observational challenges and instrumentation commonly encountered in pulsar astronomy.

1.6 Apparatus of Pulsar Observations

Various technical hurdles present themselves to pulsar observers. The primary challenge arises from the relative weakness of pulsar signals (see Section 2.1.3), which have flux densities between approximately 0.1 and 5000 mJy at 400 MHz. In order to increase the signal-to-noise ratio, long integration times, large bandwidths, and sensitive equipment with low system temperatures must be utilized (see Equation 2.6). The observation of pulsars therefore necessitates cutting-edge receiver design, which typically includes a cryogenically-cooled receiver system with stable response over a wide range of frequencies. However, with an increase in bandwidth, the amount of dispersion smearing observed across the band also increases (see Section 2.4.2).

Therefore, the observing system must also be able to correct for the effects of interstellar dispersion. This is usually achieved by dividing the wideband signal into a number of narrow sub-bands, or channels, in which the dispersion smearing is either decreased or may be considered negligible. To perform this task, three main categories of conventional instrumentation have been employed: filterbanks, spectrometers, and baseband recording/processing systems.

A filterbank system consists of an array of N narrow bandpass analog filters, each tuned to evenly spaced frequency intervals across the observing band. The received radio frequency (RF) signal is mixed to an intermediate frequency (IF) that matches the operating range of the filterbank. The IF is then multiplexed to each of the N filters, the outputs of which are square-law detected, averaged, and digitized. The digitized power may be folded using a predictive model of pulse phase and/or recorded to tape for off-line data reduction at a later time. The end result is a set of N pulse profiles which may be shifted by the relative dispersion delays between each channel before summing the power across the band.

Filterbank systems have proven to be a powerful tool in the search and study of pulsars (see, for example, Edwards et al. (2001)). However, they suffer from some fundamental limitations. For instance, depending upon the DM of the observed pulsar, there remains some degree of residual dispersion smearing across each of the channels in a filterbank. Also, as the rise-time of each filter is inversely proportional to the width of its bandpass, there exists a fundamental limit to the time resolution that may be achieved with a filterbank system. Ideally, one would balance the dispersion smearing and rise-time in each channel. However, this would necessitate a different set of filters for each DM range of interest; an unrealistic requirement.

Digital spectrometers offer a little more flexibility in this respect. There are two main classes of this type of backend: the FFT spectrometer and the autocorrelation spectrometer, an example of which is the Caltech Fast Pulsar Timing Machine (FPTM) (Navarro 1994). In these systems, the RF signal is mixed to baseband and digitally sampled at the Nyquist frequency. The digital data are then divided into segments from which either the Fast Fourier Transform (FFT) or autocorrelation as a function of lag (ACF) is computed. In the former case, each FFT is square-law detected to yield the power spectral density (PSD). The PSD or ACF estimates are then folded modulo the topocentric pulse period. In the latter case, the average PSD is computed from the average ACF after folding. (By the Wiener-Khinchin theorem, the average PSD is simply the Fourier transform of the average ACF.) Both systems yield the average power as a function of frequency and pulse phase. As with the filterbank data, the pulse profile in each frequency channel is shifted to compensate for dispersion delay before further integrating the power across the band. The width of each channel in a digital spectrometer is inversely proportional to the number of points in the FFT or number of lags computed in the autocorrelation function, N. The “rise time” in each channel is therefore proportional to N times the Nyquist sampling interval. By choosing an appropriate value of N, the residual dispersion smearing in each channel may be balanced with the minimum time resolution.

Both filterbanks and digital spectrometers are used to perform what is known as incoherent dedispersion. That is, dispersion delays are removed from the detected power of each frequency channel before integrating the total power across the band. These systems suffer to some extent from residual dispersion smearing across the smallest band in which the power is detected. By utilizing a fundamentally different approach, in which the undetected voltage waveform is corrected, the dispersion smearing may effectively be completely eliminated. This technique is known as phase-coherent dispersion removal, or coherent dedispersion (see Section 2.4.2). Note that, in this context, "phase-coherent" describes a system in which the phase information of the received electromagnetic radiation is preserved. This differs from the more widely used definition of phase coherence which describes the degree to which two signals maintain a fixed phase relationship with each other.

Coherent dedispersion may be performed either in real-time, using specially-designed digital signal processing (DSP) hardware, or during a stage of off-line data reduction, using a high-performance computing facility and custom-designed software. In the latter case, a baseband recorder is used to store a digitized version of the undetected voltage waveform for later use. As the received signal must be sampled and stored at the Nyquist rate, baseband recording necessitates high-speed digital equipment with large storage capacities, such as magnetic tape media. For this reason, early baseband recording/processing systems were limited to much smaller bandwidths than available using the conventional instrumentation (correlators and filterbanks) of the time (e.g. 125 kHz (Hankins 1971), 1.25 MHz (Hankins & Boriakoff 1978), and 250 kHz (Stinebring & Cordes 1983)). An early hardware coherent dedisperser, based on an integrated circuit that performs the Chirp-Z transform, was able to process a bandwidth of 1.5 MHz in real-time (Hankins, Stinebring & Rawley 1987).

Despite the decrease in S/N due to the (currently) smaller available bandwidths, the application of phase-coherent dispersion removal can vastly improve the accuracy of arrival time estimates. As previously mentioned, a system that performs incoherent dedispersion is limited by its individual channel bandwidth. The residual smearing in each sub-band broadens the average pulse profile, thereby increasing the arrival time estimation error (see Equation 3.3). In addition, the power from all radio frequencies within each sub-band of an incoherent system is improperly assigned the centre frequency of the channel. The presence of a sufficiently narrow scintillation band within a sub-band will bias the output of that channel toward the radio frequency of the scintillation maximum, thereby systematically distorting the average pulse profile and corrupting arrival time estimates. By properly assigning and correcting all radio frequencies within the observing band, the technique of coherent dedispersion does not suffer from these errors.

In addition, data reduction on cluster computing facilities offers two main advantages over the use of custom-designed, hardware-based observing systems. First, software algorithms are more easily developed than hardware components, affording greater flexibility in design. For instance, the spectral leakage of the discrete

Fourier transform may be improved in software by the use of a variety of apodizing functions. Increasingly sophisticated radio frequency interference (RFI) excision algorithms may also be employed in software. Second, the computational power of baseband data processing software closely follows the continual growth of affordable, commercial computing and data storage technologies, which are becoming increasingly available at institutions around the world.

By the mid-1990s, a number of baseband recording/processing systems were in use at observatories around the world. The Princeton Mark IV system, capable of continuously two-bit sampling a 10 MHz bandpass (Shrauner 1997; Stairs 1998; Stairs et al. 2000) was in use at the Arecibo and Jodrell Bank observatories. Also at Arecibo, the Caltech Baseband Recorder (CBR) could also two-bit sample a 10 MHz bandpass. The Wide Bandwidth Digital Recording (WBDR) system, capable of recording a 50 MHz bandpass (Jenet et al. 1997) and the S2 VLBI recorder, a 16 MHz system (Wietfeldt et al. 1998), were both used at Parkes. Versions of the coherent Berkeley Pulsar Processor (cBPP), a real-time hardware coherent dedisperser developed at Berkeley and capable of correcting a bandpass of up to 112 MHz (depending on pulsar DM), were installed at Green Bank, Effelsberg, and Arecibo (Backer et al. 1997).

The work presented in this thesis is based on observations made using two different baseband recorder technologies: the S2 VLBI Record Terminal (S2-RT), and the Caltech Parkes Swinburne Recorder (CPSR) (van Straten, Britton & Bailes 2000), a 20 MHz system similar in design to the CBR (see Section 2.3). The data reduction and analysis software developed and used in this work addresses the three main areas of concern outlined in Section 1.5, implementing:

1. phase-coherent dispersion removal (Hankins & Rickett 1975);

2. two-bit quantization error corrections (Jenet & Anderson 1998); and

3. arrival time estimation from the polarimetric invariant profile (Britton 2000).

A complete description of the observing instrumentation and processing techniques is presented in Chapter 2. The computation and analysis of arrival time estimates are described in Chapter 3, which also includes an account of the additions made to the standard pulsar timing model. The new model is applied in Chapter 4 to yield a geometric determination of the PSR J0437−4715 orbital inclination and thereby provide an independent confirmation of the shape of the general relativistic Shapiro delay introduced by the pulsar's companion. In Chapter 5, it is shown that phase-coherent data analysis provides the opportunity for superior calibration of the system's polarimetric response. A new calibration technique is developed and applied to observations of PSR J0437−4715. The main findings of this work are summarized in Chapter 6, following a discussion of both outstanding problems and possible future research directions.

Chapter 2

The Data Path

This thesis presents the primary results of both timing and polarimetry observations of PSR J0437−4715 made at the Parkes Observatory. However, the baseband data processing system developed for this work has been utilized in a variety of other applications. In addition to regular timing observations of a number of pulsars, the software has been used in single-pulse polarimetry and HI studies. It has also been applied to the reduction of baseband data from a number of other observatories, including the ATNF Compact Array, Arecibo, Tidbinbilla, Urumqi, and the Westerbork Synthesis Radio Telescope. Therefore, the signal processing method is described in detailed but general terms, covering the complete data reduction path from the reception of the pulsar's radio signal to the integration of the mean polarimetric pulse profile. In each section, the relevant mathematical representations are briefly reviewed while discussing both the equipment used and the algorithms implemented in software.

2.1 Reception of Electromagnetic Radiation

The phenomenon of radio may be understood as a transverse electromagnetic wave. For a plane-propagating wave, there exist two independent solutions to Maxwell's equations, representing two orthogonal senses of polarization. Receiver systems must differentiate between these two senses in order to fully describe the vector state of the observed radiation. A dual-polarization receiver is therefore designed with two receptors, or probes, which are ideally sensitive to orthogonal polarizations. As linear dipole probes are most commonly used, a Cartesian basis will be employed throughout this thesis. In this basis, the radiation propagates in the direction of the $\hat{\boldsymbol{z}}$ axis, and the electric field is measured by its projection along the $\hat{\boldsymbol{x}}$ and $\hat{\boldsymbol{y}}$ axes.

Some receivers employ waveguide structures (for example, a quarter waveplate) in order to convert from linear to circular polarization. The theories and techniques developed for linear feeds apply equally well to circularly polarized feeds after a change of mathematical basis (see Section 2.4.4). Regardless of feed design, the electric field component of the radiation impinging on the receiver feed horn induces a voltage in each of the receptors. The voltage signal from each receptor is a real-valued function of time, or process, that may be represented by its associated analytic signal.

2.1.1 The Analytic Signal

The analytic signal, also known as Gabor's complex signal, is a complex-valued representation of a real-valued process that provides its instantaneous amplitude and phase. In order to define the analytic signal associated with a process, $x(t)$, it is first necessary to define the Hilbert transform (Papoulis 1965),

$$\hat{x}(t) \equiv \frac{1}{\pi} \int_{-\infty}^{\infty} \frac{x(\tau)}{t-\tau}\, d\tau. \tag{2.1}$$

The discontinuity in $\hat{x}(t)$ at $t = \tau$ is avoided by taking the Cauchy principal value. The analytic signal associated with $x(t)$ is then defined by

$$z(t) = x(t) + \mathrm{i}\hat{x}(t). \tag{2.2}$$

As it is derived from the real-valued process, the analytic signal does not contain any additional information. However, the analytic signals from two orthogonal senses of polarization, $z_1(t)$ and $z_2(t)$, permit calculation of the coherency matrix,

$$\boldsymbol{\rho} = \langle \boldsymbol{z}(t) \otimes \boldsymbol{z}^\dagger(t) \rangle, \tag{2.3}$$

where $\boldsymbol{z}(t) = (z_1(t), z_2(t))$ is a column 2-vector, $\boldsymbol{z}^\dagger(t)$ is the Hermitian transpose of $\boldsymbol{z}(t)$, the $\otimes$ symbol represents the vector direct (or outer) product, and the angular brackets denote time averaging. As discussed in Section 5.2, the coherency matrix is directly related to the average Stokes parameters, commonly used to describe the polarization state of observed radiation. The analytic signal therefore proves to be a useful representation in radio polarimetric studies and in the theoretical description of quadrature down-conversion (see Section 2.2.1).

2.1.2 The Quadrature Filter

The Hilbert transformation of Equation 2.1 may also be written as the convolution, $\hat{x}(t) = h(t) * x(t)$, where

$$h(t) = \frac{1}{\pi t},$$

and the $*$ symbol is used to represent the convolution operation,

$$h(t) * x(t) \equiv \int_{-\infty}^{\infty} x(\tau) h(t-\tau) d\tau. \tag{2.4}$$

$x(t)$	$X(\nu)$
$\cos(2\pi\nu_0 t)$	$\frac{1}{2}(\delta(\nu+\nu_0)+\delta(\nu-\nu_0))$
$\sin(2\pi\nu_0 t)$	$\frac{\mathrm{i}}{2}(\delta(\nu+\nu_0)-\delta(\nu-\nu_0))$
$h(t)=(\pi t)^{-1}$	$H(\nu)=\begin{cases} -\mathrm{i} & \nu>0 \\ \mathrm{i} & \nu<0 \end{cases}$
$\pi(t)=\mathrm{sinc}(\pi\Delta\nu t)$	$\Pi(\nu/\Delta\nu)=\begin{cases} 0 & \|\nu/\Delta\nu\|>1/2 \\ 1/2 & \|\nu/\Delta\nu\|=1/2 \\ 1 & \|\nu/\Delta\nu\|<1/2 \end{cases}$

Table 2.1: Useful Fourier Transform pairs. The left column lists functions of time. In the right column, the corresponding Fourier transform is given as a function of oscillation frequency, ν. The filters, $H(\nu)$ and $\Pi(\nu)$, are known as the quadrature and rectangle functions, respectively.

By the convolution theorem, this transformation is equivalent to $\hat{X}(\nu)=H(\nu)X(\nu)$, where

$$H(\nu)=\begin{cases} -\mathrm{i} & \nu>0 \\ \mathrm{i} & \nu<0 \end{cases} \tag{2.5}$$

is the Fourier transform of $h(t)$, known as the quadrature filter (Papoulis 1965). Referring to the other commonly used functions and their Fourier transforms in Table 2.1, it is trivial to show that the Hilbert transform of $\cos(\nu_0 t)$ is equal to $\sin(\nu_0 t)$, enabling the quadrature filter to be understood as a 90° phase shifter. Using the quadrature filter, it can also be shown that the Fourier transform of the analytic signal, $Z(\nu)$, is equal to zero for ν less than zero:

$$\begin{aligned} Z(\nu) &= X(\nu)+\mathrm{i}\hat{X}(\nu) \\ &= X(\nu)+\mathrm{i}H(\nu)X(\nu) \\ &= \begin{cases} 2X(\nu) & \nu>0 \\ 0 & \nu<0 \end{cases} \end{aligned}$$

Conversely, the analytic signal associated with $x(t)$ may be produced by suppression of the negative frequencies in $X(\nu)$.

2.1.3 The Signal-to-Noise Ratio

Flux density is a measure of the power received per unit area, per unit frequency interval, from a source of electromagnetic radiation. In radio astronomy, the standard unit of flux density is the Jansky (Jy), where $1\,\mathrm{Jy}=10^{-26}\,\mathrm{W\,m^{-2}\,Hz^{-1}}$. The intensity of a pulsar signal is generally much weaker than that of the radio noise induced by the thermal motion of electrons in the receiver system and the background radio noise from the Galaxy (or sky). The combined noise flux of the receiver and sky is called the system temperature, $T_{\rm sys}$. Note that the terms: "intensity", "flux", "power", "flux density", and "temperature" are loosely interchanged in many texts. The use of the word "temperature" derives from the relationship, $P = kT$, between the temperature of a blackbody, T, and the radio noise power that it generates per unit of bandwidth, P, defined by Boltzmann's constant, $k = 1.3807 \times 10^{-23}\,{\rm J\,K^{-1}}$ (Kraus 1986). As a consequence of this proportionality, $T_{\rm sys}$ is commonly expressed in Kelvin.

The signal-to-noise ratio, S/N, is the ratio of the signal power to the system noise power and, for a time-averaged periodic signal, is given by

$$S/N = \frac{KS\sqrt{N_{\rm pol} t_{\rm obs} \Delta\nu}}{T_{\rm sys}}, \tag{2.6}$$

where K is the sensitivity of the radio telescope in Kelvin per Jansky, S is the flux density of the signal in Jansky, $N_{\rm pol}$ is the number of polarizations observed (one or two), $t_{\rm obs}$ is the duration over which the signal is averaged or integrated, and $\Delta\nu$ is the bandwidth of the observing instrumentation. Through Equation 2.6, the system temperature may be related to the Noise Equivalent Flux Density (NEFD), which is defined by the flux required to produce a S/N of unity after one second of integration. Antenna sensitivity is given by (Kraus 1986)

$$K = \frac{\eta_A A_0}{2k}, \tag{2.7}$$

where A_0 is the collecting area of the primary reflector and η_A is the aperture efficiency. Equations 2.6 and 2.7 motivate the use of a large dish with cryogenically cooled receivers in order to maximize S/N. Accordingly, all of the data presented in this thesis are derived from observations made using the 64 m radio telescope at the Parkes Observatory. The 20 cm timing observations were made using both the H-OH receiver and the centre element of the Multibeam receiver. Both receivers are dual-polarization systems with orthogonal linear (dipole) receptors. The Multibeam receiver has a frequency range of 1230 MHz to 1530 MHz, and an average noise temperature of 23.5 K (measured over a 64 MHz bandpass at 1394.5 MHz). The H-OH receiver has a frequency range of 1200 MHz to 1800 MHz, and an average noise temperature of 28 K (Reynolds 2003). Each receiver was interfaced with one of two different baseband recorder backends: an S2 VLBI Record Terminal (S2-RT) (Cannon et al. 1997) coupled with an ATNF Data Acquisition System (DAS) digitizer; and the Caltech Parkes Swinburne Recorder (CPSR) (van Straten, Britton & Bailes 2000), based on a similar recorder described by Jenet et al. (1997). The epoch during which each combination of receiver and backend was used is summarized in Table 2.2.

Table 2.2: Dates and equipment used

Date Range			Receiver	Backend
1997 Jul 11	$\rightarrow$	1998 Mar 03	S2-A[a]	Multibeam
1998 Mar 04	$\rightarrow$	1998 Mar 05	S2-A[a]	H-OH
1998 Apr 25	$\rightarrow$	1998 Apr 29	S2-D[b]	H-OH
1998 Aug 20	$\rightarrow$	1999 Aug 08	CPSR	H-OH
1999 Aug 10	$\rightarrow$		CPSR	Multibeam

a S2 Recorder with analog filters
b S2 Recorder with digital filters

2.2 Down-Conversion

By the Nyquist Theorem, a signal must be sampled at a rate equal to twice its bandwidth in order to completely represent the information discretely. Therefore, subject to the finite recording rate of digital observatory equipment, a radio astronomy experiment must be constrained to observe a limited portion of the radio spectrum. The intermediate process by which the signal from the receiver is band-limited and made ready for baseband recording is known as down-conversion.

Consider the incoming radio signal, $x(t)$, and its Fourier transform, $X(\nu)$, known as the spectrum, or spectral density of $x(t)$. The band-limited signal of interest, $x_b(t)$, is parameterized by its centre frequency, ν_0, and bandwidth, $\Delta\nu$. Baseband down-conversion is the process by which the spectral information originally contained in the range $[\nu_0 - \Delta\nu/2,\ \nu_0 + \Delta\nu/2]$ is shifted down to $[0,\ \Delta\nu]$. It is worth noting that this definition of baseband differs slightly from the more widely accepted use in the telecommunications industry, where baseband refers to the original band of frequencies of a signal before it is used to modulate a carrier of much higher frequency.

The spectral information is shifted to baseband by demodulating or mixing the radio frequencies (RF) with a local oscillator (LO). This is equivalent to multiplying the signal, $x(t)$, with a pure tone, $l(t) = a\cos(2\pi\nu_l t) + b\sin(2\pi\nu_l t)$. By application of the convolution theorem, and reference to Table 2.1, mixing may also be understood as a convolution with a pair of (complex) delta functions in the frequency domain. This understanding proves useful in the following sections.

In addition to mixing to lower frequencies, the signal must also be band-limited before analog-to-digital conversion. Otherwise, power from frequencies higher than the Nyquist frequency will be reflected back into the band of interest, a pollution known as aliasing. The ideal low-pass filter is represented by the rectangle function (see Table 2.1) so that a bandpass filter with centre frequency, ν_0, and bandwidth, $\Delta\nu$, is given by

$$\Pi\left(\frac{|\nu| - \nu_0}{\Delta\nu}\right). \tag{2.8}$$

Note that the absolute value of ν in the first term of the above equation creates a bandpass window at both positive and negative frequency values.

Down-conversion therefore refers to the combined operation of mixing and band-limiting. The following sections describe in detail two commonly used methods of down-conversion: dual-sideband (DSB) and single-sideband (SSB). These are also represented graphically in Figures 2.1 and 2.2. The process of down-conversion is performed separately and (ideally) identically on each of the two orthogonal senses of polarization from the receiver feed.

2.2.1 Dual-Sideband Down-Conversion

During dual-sideband down-conversion (DSB, see Figure 2.1), also known as quadrature mixing, the voltages from the receiver are split equally into two signal paths. One signal is mixed with a local oscillator, producing

$$i(t) = x(t)\cos(2\pi\nu_0 t + \theta).$$

The other signal is mixed with the same local oscillator phase-shifted by 90 degrees,

$$q(t) = x(t)\cos(2\pi\nu_0 t + \theta - \pi/2) = x(t)\sin(2\pi\nu_0 t + \theta).$$

Both $i(t)$ and $q(t)$ are low-pass filtered with a cutoff frequency of $\nu_c = \Delta\nu/2$, producing $i_b(t) = i(t) * \mathrm{sinc}(\pi\Delta\nu t)$ and $q_b(t) = q(t) * \mathrm{sinc}(\pi\Delta\nu t)$. The low-pass filtered signals are then digitally sampled at the Nyquist rate of $2\nu_c = \Delta\nu$. The signals, $i_b(t)$ and $q_b(t)$ are known as the in-phase and quadrature components, respectively, of $x(t)$ with respect to ν_0.

During playback, the analytic signal associated with $x(t)$ is formed by taking:

$$\begin{aligned} z_b(t) &= i_b(t) + \mathrm{i}q_b(t) \\ &= [x(t)\cos(2\pi\nu_0 t) + \mathrm{i}x(t)\sin(2\pi\nu_0 t)] * \mathrm{sinc}(\pi\Delta\nu t) \\ &= [x(t)e^{2\pi\mathrm{i}\nu_0 t}] * \mathrm{sinc}(\pi\Delta\nu t) \end{aligned}$$

where the distributive property of convolution has been applied and the arbitrary phase angle, θ, has been set to zero without loss of generality. In the Fourier domain,

$$Z_b(\nu) = X(\nu + \nu_0)\Pi(\nu/\Delta\nu).$$

That is, the spectrum of $z_b(t)$ is equivalent to the band-limited portion of $x(t)$ centred at ν_0. The negative frequency components, centred at $-\nu_0$, have been suppressed by low-pass filtering, forming the analytic signal associated with $x(t)$.

The CPSR utilizes an analog dual-channel quadrature down-converter with four 10 MHz anti-aliasing low-pass filters in order to simultaneously perform DSB down-conversion of two 20 MHz bandpasses; one from each of the linear polarizations from the receiver feeds. The mixer LO is provided by an external signal generator.

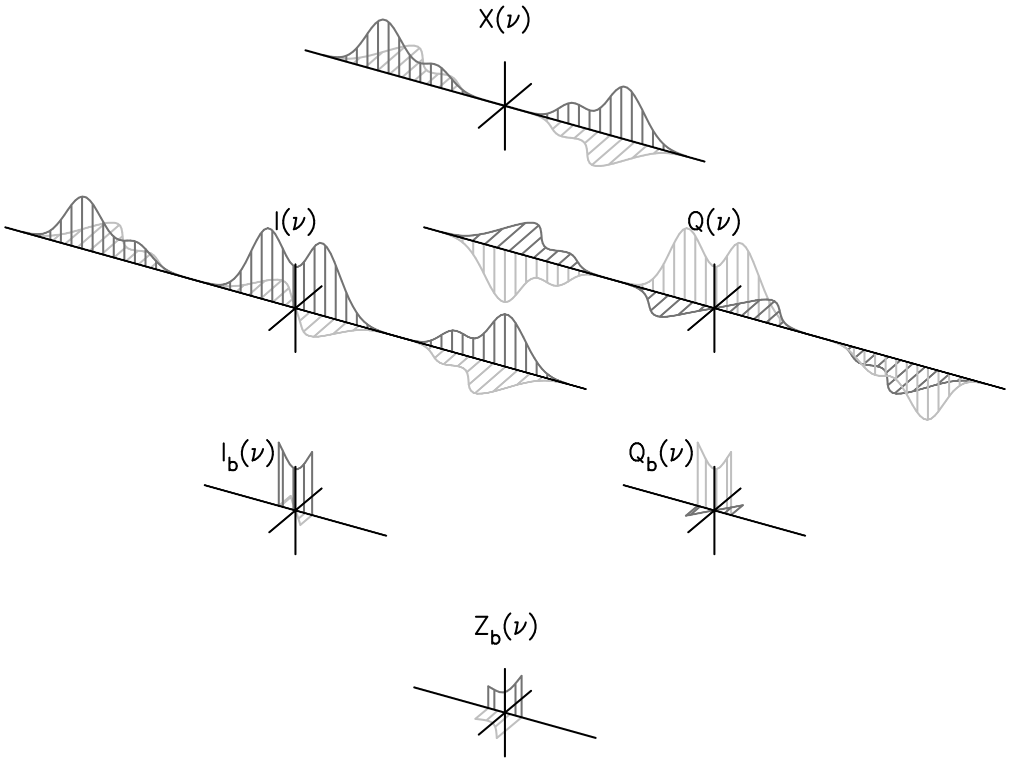

Figure 2.1: During dual-sideband down-conversion (DSB), the real signal, $\mathbf{X}(\nu)$, is split during mixing into its in-phase, $\mathbf{I}(\nu)$, and quadrature, $\mathbf{Q}(\nu)$, components before low-pass filtering. The centre frequency and bandwidth of interest are ν_0 and $\Delta\nu$, respectively. Each of the signals, $\mathbf{I}_b(\nu)$ and $\mathbf{Q}_b(\nu)$, have bandwidth $\Delta\nu/2$. The complex signal, $\mathbf{Z}_b(\nu)$=$\mathbf{I}_b(\nu)$+i$\mathbf{Q}_b(\nu)$, is the band-limited analytic signal associated with $\mathbf{X}(\nu)$.

2.2.2 Single-Sideband Down-Conversion

During single-sideband down-conversion (SSB, see Figure 2.2), the signal of interest, $x(t)$, is first bandpass filtered, producing $x_b(t)$ where $X_b(\nu) = X(\nu)\Pi((|\nu| - \nu_0)/\Delta\nu)$. The band-limited signal is then mixed with a LO with frequency, ν_1, producing $x_m(t) = x_b(t)\cos(2\pi\nu_1 t + \theta)$, where ν_1 set to either $\nu_0 + \Delta\nu/2$ (lower-sideband) or $\nu_0 - \Delta\nu/2$ (upper-sideband). After another stage of low-pass filtering, $x_u(t)$ is then digitally sampled at the Nyquist rate, $2\Delta\nu$. As bandpass filtering is performed before mixing, the filter used in the first stage must be tunable over the range of interesting centre frequencies, unlike the low-pass filter in a DSB down-converter. For this reason, DSB is often the more economical means of down-conversion.

During playback, the analytic signal associated with $x(t)$ may be formed in practice by taking the real-to-complex Fast Fourier Transform (FFT)[1], followed by the complex-to-complex inverse FFT. Most real-to-complex FFT implementations automatically omit the redundant negative frequencies ($F(-\nu) = F^*(\nu)$) from their

[1]The Fastest Fourier Transform in the West (FFTW) is used in the reduction software. See `http://www.fftw.org`.

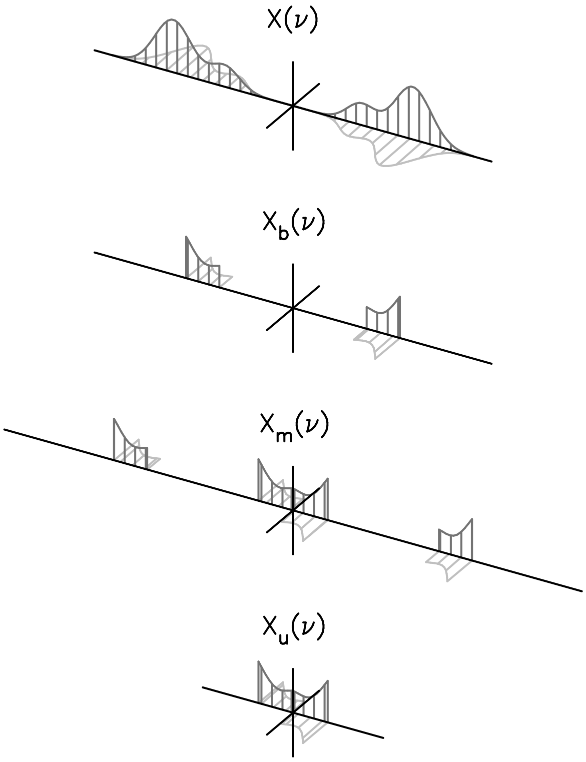

Figure 2.2: During single-sideband down-conversion (SSB), the real signal, $\mathbf{X}(\nu)$, is bandpass filtered before mixing. The centre frequency and bandwidth of interest are ν_0 and $\Delta\nu$, respectively. The band-limited signal, $\mathbf{X}_b(\nu)$, may be mixed with a local oscillator set to $\nu_0 + \Delta\nu/2$ (lower-sideband) or $\nu_0 - \Delta\nu/2$ (upper-sideband, shown here). The resulting signal, $\mathbf{X}_m(\nu)$, is low-pass filtered, producing $\mathbf{X}_u(\nu)$ with bandwidth $\Delta\nu$.

output, implicitly producing the analytic signal (see Section 2.1.2). Since the main data-reduction operation (see Section 2.4.2) is performed in the Fourier domain, the cost of calculating the analytic signal is transparent.

A combination of analog filters and frequency translators is used to perform SSB down-conversion on each of two linear polarizations before presenting the two 16 MHz bandpasses to the ATNF DAS digitizer. As listed in Table 2.2, the analog filters were replaced by digital filters in April of 1998.

2.3 Digitization

The band-limited voltage wave-form, $x_b(t)$, is an analog signal that must be converted into digital form before it may be recorded on digital media and manipulated using digital electronics. The process of analog-to-digital (A/D) conversion is most directly parameterized by the sampling rate, r, the number of bits per sampled datum, n_b, and the set of $Q-1$ sampling thresholds, $x_k; 0 < k < T$, where $Q = 2^{n_b}$ is the total number of unique digitizer output states.

As previously mentioned, the sampling rate is directly related to the bandwidth of the observation by the Nyquist Theorem, that is, $r = 2\Delta\nu$. In the DSB case, two channels representing the real and imaginary components of the analytic signal are sampled at half the Nyquist rate; however, the total number of samples produced per time interval is identical to SSB. The CPSR system performs DSB down-conversion and the 20 MHz bandpass is digitized with a sampling interval of $t_s = 50$ ns. As will be shown in Section 3.3, the RMS residual of this high-precision pulsar timing experiment is currently less than 130 ns. Therefore, an error in the sampling clock phase, $\epsilon_s \lesssim 50$ ns, will make a non-trivial contribution to the residual timing noise. The signal generator used to provide the sampling clock is phase-locked to a hydrogen maser frequency standard, the "station 1-Hz". However, the absolute phase of the generator is not preserved when its settings are changed or when its power is cycled. Therefore, beginning in May 2000, the relative phase between sampling clock and station 1-Hz was regularly calibrated to better than 5 ns accuracy using a digital oscilloscope.

The station 1-Hz is in turn monitored with reference to the Coordinated Universal Time (UTC) standard broadcast by the Global Positioning System (GPS). The Parkes Totally Accurate Clock (TAC) records the difference, $\Delta_{\mathrm{C(1)}} =$ UTC(PKS)-UTC(GPS), every five minutes, resulting in a daily average estimate, $\langle\Delta_{\mathrm{C(1)}}\rangle$, with a standard deviation of 6 ns (pre-October 2000) and 4 ns (post-October 2000) (Reynolds 2001). The difference between UTC(GPS) and International Atomic Time (TAI), $\Delta_{\mathrm{C(2)}}$, is monitored by the International Bureau of Weights and Measures (BIPM) and published monthly in the BIPM *Circular T*. (Note that UTC differs from TAI only by an integral number of seconds.) According to BIPM, TAI should not lose or gain more than 100 ns per year and the daily estimate of the mean, $\langle\Delta_{\mathrm{C(2)}}\rangle$, has an error of the order of 10 ns. Using the TAC and BIPM tables of corrections, the time estimates derived from the observatory sampling clock may be retroactively corrected to reflect UTC with an accuracy of approximately 20 ns.

The number of bits per sample and the values of the sampling thresholds are related to the dynamic range of the system. The dynamic range of an A/D converter is the ratio of the maximum signal power, or saturation level, to the system noise power. This is similar to the definition of S/N, except that dynamic range is based on the system noise power when no signal is present. As shown in Appendix A, the average instantaneous S/N of PSR J0437−4715 is approximately 0.16. Therefore, the incoming noise waveform may be sampled with low dynamic range and n_b may be small.

The total data rate, R_T, is simply the product of the sampling rate and the number of bits per sample, $R_T = rn_b$. Therefore, given the maximum recording capacity in bits per second of the digital storage medium, a trade-off must be made between bandwidth and dynamic range, such that the S/N is maximized. The S/N is proportional to the square root of the bandwidth (see Equation 2.6) and the fractional loss in S/N due to halving the bandwidth is $1\text{-}2^{-1/2} \sim 0.293$. Referring to Table 2 of Jenet & Anderson (1998), the fractional S/N lost by sampling with two instead of four bits is $\sim$0.126. Therefore, two-bit sampling is utilized and the total data rate for CPSR is

$$R_T = 4(\text{channels}) \times 2\,\text{bits/sample} \times 20\,\text{Msamples/s} = 20\,\text{MB/s},$$

where the four analog input channels represent the in-phase and quadrature components of the two orthogonal senses of polarization.

The $Q-1$ sampling thresholds, x_k, define the range of values of the incoming voltage, $x_b(t)$, that correspond to one of the Q digitized output states. Each digitized state is later assigned an output value, y_k. The sampling thresholds and digitized output values are chosen in order to minimize signal distortion and quantization noise (Jenet & Anderson 1998). As the experimental aim is to measure the power as a function of pulse phase, x_k and y_k are optimized in order to produce unbiased power estimates. For a two-bit sampler, $Q = 4$, and the optimal sampling thresholds are given by $x_3 = -x_1 = 0.9674\,\sigma_n$ and $x_2 = 0$, where σ_n^2 is the average power of the input signal, $x_b(t)$ (Jenet & Anderson 1998). The optimal assignment of the output levels, y_k, is discussed in detail in Section 2.4.1.

The system and sky temperatures change as a function of time, and it is necessary to monitor the both the mean, $\langle x_b(t)\rangle$, and the power, σ_n^2, of the input signal in order to maintain optimal sampling thresholds. An on-line program performs this monitoring task by interfacing with the CPSR raw data buffer and sending level-setting commands to the CPSR Fast Flexible Digitizer (FFD) over a RS-232 serial port connection.

Synchronized to the external sampling clock, the FFD is used to two-bit sample each of the four 10 MHz bandpasses. Digitized data are sent via 16-bit parallel digital connection to a Sun Ultra SPARC 60 with 512 MB RAM and a commercially available Direct Memory Access (DMA) card (Engineering Design Team's PCD20 DMA card). Control software running on the Sun workstation stripes the incoming data to six 8.5 GB SCSI disks. From disk, approximately one-minute (1 GB) segments of data are gathered and written to one of four DLT 7000 tape drives. As each continuous one-minute block is written to one tape, only one drive is required during playback. As each DLT 7000 tape can store up to 35 GB, 32 one-minute blocks are written to each tape, allowing up to 2 hours between tape changes.

The ATNF DAS two-bit samples each of the two 16 MHz bandpasses, corresponding to the two orthogonal polarizations. The DAS monitors the power of the incoming analog signal and every ten seconds updates its sampling thresholds. Therefore, no additional monitoring software is required while the S2/DAS system is in use. The digitized data are sent from the DAS to the S2-RT User Interface Card (UIC) at a rate of 16 MB/s, along with a synchronization clock signal and the station 1-Hz. On the S2-RT, UTC time stamps, synchronization codes, and auxiliary user information are written with the digitized data to an array of eight S-VHS tape recorders. A single S2 tape-set (consisting of eight S-VHS tapes) can record up to 500 GB of data, for an unattended record time of up to 8.5 hours.

As the S2 system records data onto S-VHS tapes, the cost of storage media is quite low. However, the playback terminal (S2-PT) is not as cost efficient and requires specialized engineering skills for both maintenance and repair. Although the capabilities of the S2 Tape-to-Computer Interface (Wietfeldt et al. 1998) were expanded to use network resources more efficiently, the playback method proved to be detrimental to both the transport units and the overall playback terminal performance. Therefore, the decision was made to switch to a new baseband recorder technology. The CPSR was designed in cooperation with colleagues at Caltech and installed at Parkes in August of 1998. It consists entirely of commercially available components and is also easier to wire up and operate, compared to the S2/DAS.

This convenience of operation was vitally important to the observing strategy undertaken at the beginning of the year 2000. As the three-dimensional modeling of the orbital geometry presented in Section 3 requires excellent day-of-year coverage, it was decided to increase the frequency of our observations. Assistance was enlisted from the technical staff at Parkes, and the much simpler interface to CPSR greatly reduced the probability of experimental error.

The complete recording process is presented in Figure 2.3. Both the Multibeam and H-OH receivers serve at different times as the Prime Focus Receiver. The RF signal from the receiver is mixed to an intermediate frequency (IF) before it is sent from the Focus Cabin to the Observatory Control Rack. Here, the IF is further amplified or attenuated and, if more than one backend is used for observing, split into the required number of signal paths. Depending upon the operating range of the baseband down-converter, the IF may be shifted by mixing before presentation to the Baseband Down-Conversion system. Either SSB or DSB down-conversion is performed, depending on the Baseband Recorder used. The baseband signal is then two-bit sampled in synchronization with the Sampling Clock, and recorded to tape.

2.4 Reduction

Data are read from tape and subsequently processed off-line at Swinburne University using a beowulf-style cluster of high-performance workstations. This cluster underwent a number of upgrades and expansions over the course of this thesis. Table 2.3 lists the new equipment added to the cluster during each upgrade, including the additional storage and computing capacity.

CPSR data are transferred to disk using a DLT 7000 tape drive and commercially available tape robot. Each S2 tape-set is transferred to disk using the S2 Tape-to-Computer Interface, S2-TCI (Wietfeldt et al. 1998). Data reduction software is executed in parallel on the cluster using the `mpich` Message Passing Interface (MPI) library (Gropp et al. 1996). The data reduction algorithm is outlined in the flowchart in Figure 2.7, and described in detail in the following sections.

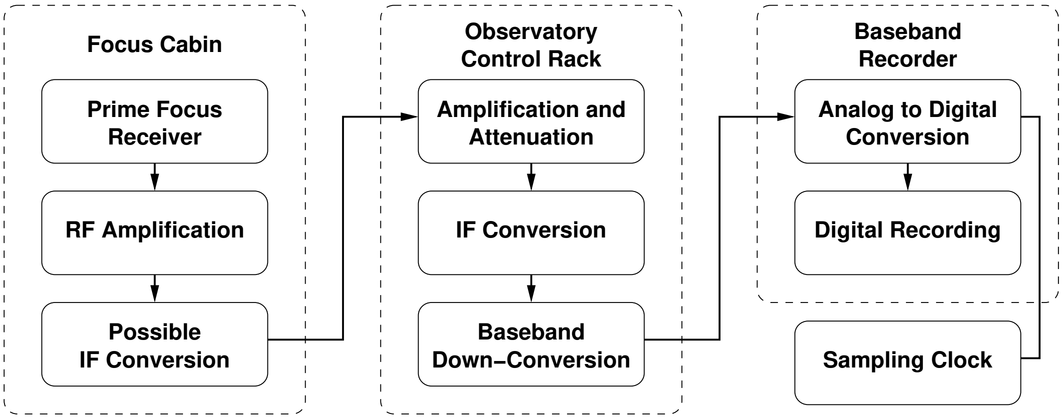

Figure 2.3: Overview of baseband recording. Although only one signal path is shown from receiver to recording, two orthogonal senses of polarization are received and propagated along separate signal paths. The specifics of the observing configuration (for example, the number of IF conversions) may vary between different receiver and recorder combinations.

Table 2.3: Computing facility expansions

Date	Equipment Added	Storage (GB)	Gflops
1998 Jan	16 Digital 500 MHz ev56	180	16
1998 Dec	8 Digital 600 MHz ev56	22	9.6
1999 Mar	41 Compaq 500 MHz ev6	880	41
2000 Jan	Compaq ES450 4×667 MHz ev67 + 1TB RAID	1,110	5.3
2001 Jan	16 Dell Dual PIII 933 MHz	340	59.7

The actual performance of each machine did not scale linearly with the theoretical Gflops rating. For instance, the ev6 chip includes both divide and square-root operators that accelerate its performance, effectively increasing its computing power to approximately twice that of the ev56 processor.

2.4.1 Dynamic Output Level Setting

The pulsar signal is a source of amplitude-modulated wide-band noise, and may be treated statistically as a non-stationary stochastic process. The instantaneous power, σ^2, fluctuates on the time-scale of the pulsar period, which is necessarily much shorter than the interval over which the estimate of σ_n is calculated, where σ_n is the average power estimate on which the optimized sampling thresholds are based. The fluctuation of σ away from σ_n results in a slight deviation away from the optimal state of two-bit sampling, and therefore increases the level of distortion. To compensate for this deviation during playback, each two-bit digital datum is re-interpreted in the context of a local estimation of the undigitized power and assigned an optimal output floating-point value such that the distortion to the output signal power is minimized (Jenet & Anderson 1998).

During this process of dynamic output level setting, the data is divided into consecutive segments of L digitized samples. In each segment, the number of states, M, that correspond to undigitized voltage levels between x_1 and x_3 (low voltage states) are counted. The undigitized power, σ^2, in this segment of L points is then estimated by inverting

$$\Psi = \frac{M}{L} = \int_{-x_3}^{x_3} P(x)dx. \tag{2.9}$$

Where $P(x)$ is the probability density function of the analog signal, $x_b(t)$. Assuming that x_b is distributed normally,

$$P(x) = \frac{1}{\sqrt{2\pi}\sigma} \exp\left(-\frac{x^2}{2\sigma^2}\right), \tag{2.10}$$

and Equation 2.9 may be re-written as

$$\Psi = \mathrm{erf}\left(\frac{x_3}{\sqrt{2}\sigma}\right), \tag{2.11}$$

where the error function,

$$\mathrm{erf}(x) = \frac{2}{\sqrt{\pi}} \int_0^x e^{-y^2} dy. \tag{2.12}$$

Equation 2.11 is solved for σ by inverting the error function. In order to obtain a statistically meaningful estimate of σ, L must large enough that estimation errors ($\propto L^{-1/2}$) are small. However, $L \times t_s$ must also be smaller than the shortest time-scale over which σ is expected to fluctuate. As will be discussed in Section 2.4.2, this minimum time-scale is given by the dispersion smearing time, t_d. For PSR J0437$-$4715, which has a dispersion measure of approximately $2.65\,\mathrm{pc\,cm^{-3}}$, observed with a bandwidth of 20 MHz and centre frequency of 1413 MHz, Equation 2.15 yields $t_d \sim 155\mu$s, so that $L \leq 3100$ points. The chosen value of $L = 512$ yields power estimation errors of the order of 4%.

The inverse error function is determined using an iterative technique (the Newton-Raphson method), and it is computationally prohibitive to perform this calculation for every L-point segment of data. However, given fixed L, there are a limited number of possible values of $\Psi = M/L$, where $0 < M \leq L$, and the use of a lookup table containing the output levels corresponding to each given value of M greatly improves the efficiency of this calculation.

The values of M corresponding to each segment of L digitizer samples are stored in parallel with the output, two-bit corrected time samples. Under certain circumstances, these values may be utilized during a second stage of digitization correction known as "scattered power correction" (Section 2.4.4). It is also useful to store in the header of each reduced archive data file a histogram of occurrences of M, which may be used as a diagnostic tool when later assessing the quality of the baseband recording.

2.4.2 Coherent Dedispersion

As mentioned in Section 1.6, the primary data reduction task performed in software is phase-coherent dispersion removal (Hankins 1971; Hankins & Rickett 1975). In this context, dispersion refers to the broadening of the pulse profile that arises from the frequency-dependent group velocity of electromagnetic radiation propagating in the interstellar medium (ISM). By modeling the ISM as a cold, tenuous plasma, Hankins & Rickett (1975) derive a dispersion frequency response function,

$$H(\nu+\nu_0) = \exp\left(\mathrm{i}\frac{2\pi D\nu^2}{\nu_0^2(\nu+\nu_0)}\right), \tag{2.13}$$

that may be used to invert the effect of the ISM. Here, ν_0 is the centre frequency of the observation and the dispersion, D, is related to the more commonly used dispersion measure, DM, by (Backer et al. 1993)

$$DM\,(\mathrm{pc\,cm^{-3}}) = 2.410331(2)\times 10^{-4} D\,(\mathrm{s\,MHz^2}). \tag{2.14}$$

The dispersion measure is, in turn, given by the integral of the free electron density along the line of sight to the pulsar (Section 1.2).

Pre-detection, or phase-coherent, dispersion removal is performed by convolving the data with the inverse of the dispersion impulse response function. By the discrete convolution theorem, this operation may be more efficiently performed in the frequency domain by multiplication with the inverse of the discrete form of Equation 2.13 (Bracewell 1986). However, the discrete convolution theorem is valid only under the assumption that the input data are periodic, with period equal to the length of the transform. That is, $x_b(t_k) = x_b(t_{k+lN})$, where N is the number of points in the transform (necessarily equal to the size of the discrete frequency response function, $H^{-1}(\nu_k)$) and l is an arbitrary integer. The discrete convolution operation therefore results in cyclical convolution, as described in Chapter 18 of Bracewell (1986) and § 13.1 of Numerical Recipes (Press et al. 1992, hereafter NR).

By comparing Figure 2.4 of this text with Figure 13.1.3 of NR, it can be seen that each time sample output by the cyclical convolution operation will depend upon the $n_d^+ = rt_d^+$ points preceding it and the $n_d^- = rt_d^-$ points following it, where r is the rate at which $x_b(t)$ is sampled. Therefore, the first n_d^+ points in the cyclical convolution product will be erroneously mixed with data wrapped around from the end of the data segment, and the last n_d^- points of the result will be erroneously mixed with time samples from the beginning of the input segment (see also Figure 18.4 of Bracewell (1986)). To compensate for this effect, the polluted points (called the wrap-around region) from the result of each transformation are simply discarded, a technique that forms part of the overlap-save method of discrete convolution. This

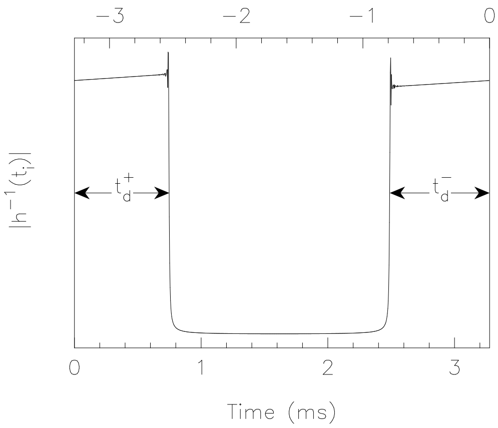

Figure 2.4: The magnitude of the dedispersion impulse response function, $|h^{-1}(t_i)|$, is calculated from the inverse FFT of the frequency response function, $H^{-1}(\nu_k)$. For this example, ν_0=600 MHz, $\Delta\nu$=20 MHz, DM=2, and N=65536 points. The smearing in the upper half of the band, $t_d^+ = 750\mu$s, and lower half of the band, $t_d^- = 788\mu$s, result in asymmetry about $t = 0$. Note that t_d^+ and t_d^- correspond to m_+ and m_- in Figure 13.1.3 of Numerical Recipes.

method, depicted in Figure 2.5, also accounts for the fact that the duration of the impulse response function is generally much shorter than that of the time-series to be convolved.

The duration, or rise time, of the dispersion impulse response function is called the sweep or smearing time, t_d (note that $t_d = t_d^- + t_d^+$). It is equivalent to the width of a band-limited delta-function after passage through the ISM, and is a function of the bandwidth, $\Delta\nu$, and centre frequency, ν_0, such that

$$t_d = D(\nu_{\min}^{-2} - \nu_{\max}^{-2}), \tag{2.15}$$

where $\nu_{\min} = \nu_0 - \Delta\nu/2$, and $\nu_{\max} = \nu_0 + \Delta\nu/2$ are given in MHz. Coherent dedispersion restores the original delta-function by advancing the signal from lower frequencies and delaying the signal from higher frequencies so that all coincide with the arrival of the signal from the centre frequency. Noting the quadratic form of Equation 2.15, it can be seen that the lowest frequency must be advanced by an amount greater than the delay applied to the highest frequency. This results in asymmetry of $h(t_i)$ around $t = 0$, such that $n_d^+ < n_d^-$, and must be accounted when discarding wrap-around points from the result of each cyclical convolution operation.

As $n_d = n_d^- + n_d^+$ points are discarded, N must be greater than n_d and is chosen by maximizing the efficiency,

$$\mathcal{E} = \frac{N - n_d}{\mathcal{O}_{\rm FFT}(N)} \tag{2.16}$$

where $\mathcal{O}_{\rm FFT}(N)$ is the order of the FFT operation, assumed to be $N \log N$ when N is a power of two. In practice, $\mathcal{O}_{\rm FFT}(N)$ will be dominated by the physical parameters of the computing workstation, such as cache size. For instance, when the memory

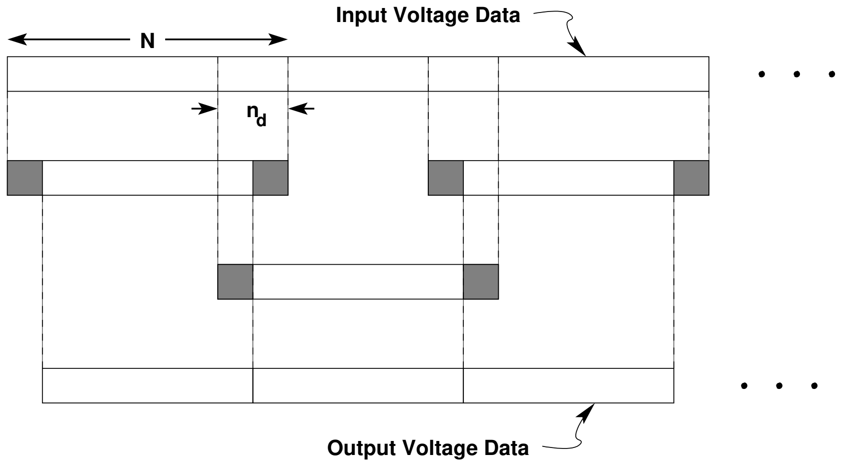

Figure 2.5: During overlap-save, the input data (top) are divided into over-lapping segments of N points. The amount by which they overlap is the number of non-zero points, n$_d$, in the discrete dedispersion impulse response function. Each N-point segment is separately transformed into the Fourier domain, multiplied by the discrete dedispersion frequency response function, $H^{-1}(\nu_k)$, and transformed back into the time domain (middle). Polluted points from the wrap-around region (shaded grey) are discarded before copying the result into the output dataset (bottom).

required to store the transform (and its plan) exceeds the cache size, the overhead of cache page-swapping will adversely affect performance.

2.4.3 Coherent Filterbank Dedispersion

Coherent dedispersion allows the original temporal resolution of the digitized dataset to be retained. However, this high time resolution is often integrated away into an average profile with phase bin interval much larger than the sampling interval, t_s. It therefore proves useful to trade some time resolution for frequency resolution by dividing the observed band into a number of sub-bands, or channels. There are a number benefits to be gained by forming a “synthetic” or “software” filterbank. First, the smearing time, t_d, in each sub-band is reduced, resulting in smaller n_d and required transform length, N, thereby improving the efficiency of data reduction (see Equation 2.16). Second, by retaining frequency resolution, the measured polarization may be better calibrated using post-detection techniques (see Section 5.2). Finally, individual sub-bands containing narrow-band radio-frequency interference (RFI) may be discarded, or a better estimate of DM may be used at a later time to correct the dispersion delays between each sub-band before further integrating in frequency.

During synthetic filterbank construction, the time-series of discretely sampled voltages, $x_b(t_i)$, is divided into N_c sub-bands using the FFT. In the simplest case, the data are divided into non-overlapping segments of N_c complex points (or $2N_c$ real points). Each segment is transformed into the Fourier domain, where each of

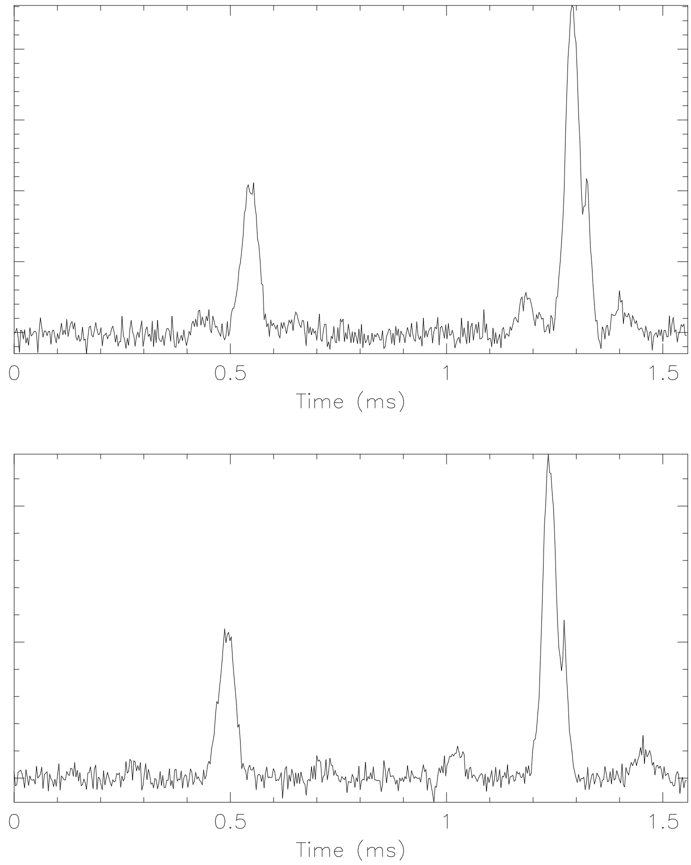

Figure 2.6: Corruption due to spectral leakage. PSR B1937+21 was observed at 1405 MHz using 64 MHz of the CPSR-II band. The observation was processed using a synthetic filterbank with 128 channels (top panel) and 64 channels (bottom panel). With $DM \sim 71.04$, the dispersion delay between neighbouring channels ($\sim$ 114 μs and 228 μs, respectively) can be readily seen between the main peak and the leakage artifacts to either side of it.

the N_c complex spectral values, $X_b(\nu_k)$, is treated as a time-sample in one of N_c independent analytic signals, each with bandwidth, $\Delta\nu' = \Delta\nu/N_c$, and sampling rate, $r' = r/N_c$. Phase-coherent dispersion removal is then separately performed on each of the N_c resulting time-series using unique dedispersion frequency response functions, each tuned to the centre frequencies, ν_k, of the output filterbank channels.

This method of synthetic filterbank formation suffers from spectral leakage, as described in Section 13.4 of NR. Owing to the square time-domain window function inherent to the discrete Fourier transform, a significant amount of power (up to $\sim$20%) from neighbouring frequency components is convolved into each output filterbank channel. When the inter-channel dispersion delay is large, the artifacts of spectral leakage can be readily seen as delayed images of the pulse profile, as shown in Figure 2.6.

The spectral leakage function may be improved by the application of a tapering function in the time domain, a technique known as "data windowing". However, the corresponding physical bandwidth of the spectral leakage function (NR, Figure 13.4.2) may also be decreased by increasing the length of the Fourier transform by a factor, N. Where $K = N \times N_c$, each K-point segment of data is transformed into the Fourier domain, and the result is divided into N_c non-overlapping segments of N spectral points. Each segment is inverse transformed back into the time domain, producing N time samples from N_c independent time-series, or filterbank channels.

Phase-coherent dispersion removal may be performed simultaneously with this synthetic filterbank technique. While in the Fourier domain, each of the N_c spectral segments is multiplied by a unique dedispersion frequency response function. In this case, N must naturally be chosen to match the size of the response function. As the inverse transform size (N) must be the same in each sub-band, the size of the response function must be large enough to accommodate the maximum smearing time, $t'_d = D(\nu_{\rm min}^{-2} - \nu'^{-2}_{\rm max})$, corresponding to the sub-band with the lowest centre frequency, where $\nu_{\rm min} = \nu_0 - \Delta\nu/2$, and $\nu'_{\rm max} = \nu_{\rm min} + \Delta\nu/N_c$. Owing to the quadratic form of Equation 2.15, $t'_d \gtrsim t_d/N_c$. Although the smearing is less severe in those sub-bands with higher centre frequencies, simplicity dictates that $n'_d = r't'_d \gtrsim n_d/N_c^2$ wrap-around points are discarded from the result of each of the N_c inverse transforms (cyclical convolution products). Each K-point segment of data in the original time-series must therefore overlap by $N_c \times n_d$ points.

Note that the size of the first FFT, $K = N_c \times N > n_d/N_c$, is roughly **inversely** proportional to the number of filterbank channels, N_c. As smaller transform lengths improve processing efficiency, N_c should be chosen to be as large as possible without sacrificing the desired time resolution of the resulting time-series. This remains true only up to the limit where the resulting time resolution, $t'_s = 1/r'$, becomes larger than t'_d (ie. where $n'_d \leq 1$).

Coherent filterbank dispersion removal may be summarized by the following algorithm:

1. Divide the time-series into segments of K points ($K = N_c \times N$) that overlap by $N_c \times n_d$ points (cf. top of Figure 2.5).

2. For each segment, perform the K-point FFT, and divide the result into N_c non-overlapping segments, or sub-bands, of N points.

3. For each of the N_c sub-bands, $k = 1$ to $k = N_c$:

   (a) multiply the N-point spectrum by the dedispersion frequency response function specific to centre frequency, ν_k;

   (b) perform an N-point inverse FFT;

   (c) discard the n'_d points from the wrap-around region;

   (d) copy the remaining points into the $k^{\rm th}$ time-series.

2.4.4 Detection and Integration

Typically, only the total intensity pulse profile is utilized for the purposes of pulsar timing. However, as discussed in Section 5.2, the polarimetric response of a receiver can significantly alter the observed total intensity, thereby systematically skewing estimates of pulse time-of-arrival (TOA). Apart from the concerns of high-precision timing, the characteristics of the pulsar's polarized radiation may offer insight into the emission mechanism, the geometry of the pulsar's magnetic field, and the magnetic field of the ISM. Therefore, it is a vital part of pulsar astronomy to retain and accumulate all of the polarization information, commonly represented using the Stokes parameters.

It proves useful to organize the four, real-valued components of the Stokes parameters into scalar and vector components, writing $[S_0, \boldsymbol{S}]$, where S_0 is the total intensity, $\boldsymbol{S} = (S_1, S_2, S_3)$, is the polarization vector, and $S_0, S_1, S_2,$ and S_3 correspond to the more commonly used Stokes I, Q, U, and V, respectively (Britton 2000; Hamaker 2000). The Stokes parameters may be mapped onto a point in the Poincare sphere by $\boldsymbol{p} = \boldsymbol{S}/S_0$, and related to the coherency matrix (Equation 2.3) by (Britton 2000)

$$\boldsymbol{\rho} = (S_0\mathbf{I} + \boldsymbol{S} \cdot \boldsymbol{\sigma})/2, \tag{2.17}$$

where $\mathbf{I}$ is the 2×2 identity matrix, and $\boldsymbol{\sigma}$ is a 3-vector whose components are the Pauli spin matrices. In the Cartesian (linear) basis, these are

$$\boldsymbol{\sigma}_1 = \begin{pmatrix} 1 & 0 \\ 0 & -1 \end{pmatrix} \quad \boldsymbol{\sigma}_2 = \begin{pmatrix} 0 & 1 \\ 1 & 0 \end{pmatrix} \quad \boldsymbol{\sigma}_3 = \begin{pmatrix} 0 & -\mathrm{i} \\ \mathrm{i} & 0 \end{pmatrix}. \tag{2.18}$$

By expanding Equation 2.3, the Stokes parameters are given in the linear basis by

$$\mathrm{I} \equiv S_0 = \quad \rho_{11} + \rho_{22} \quad = \langle |z_1(t)|^2\rangle + \langle |z_2(t)|^2\rangle \tag{2.19}$$

$$\mathrm{Q} \equiv S_1 = \quad \rho_{11} - \rho_{22} \quad = \langle |z_1(t)|^2\rangle - \langle |z_2(t)|^2\rangle \tag{2.20}$$

$$\mathrm{U} \equiv S_2 = \quad \rho_{21} + \rho_{12} \quad = 2\mathrm{Re}[\langle z_2(t) z_1^*(t)\rangle] \tag{2.21}$$

$$\mathrm{V} \equiv S_3 = \quad (\rho_{21} - \rho_{12})/\mathrm{i} \quad = 2\mathrm{Im}[\langle z_2(t) z_1^*(t)\rangle], \tag{2.22}$$

and may be calculated in the circular basis by cyclic permutation of the indices of $\boldsymbol{\sigma}$, such that $(1,2,3) \rightarrow (3,1,2)$, (ie. (Q,U,V) $\rightarrow$ (V,Q,U) in Equations 2.20 to 2.22).

When detecting synthetic filterbank data, the coherency matrix is formed as a function of frequency, resulting in $\bar{\mathbf{P}}(\nu_k)$ (Section 5.2). Each element of this matrix, $\bar{P}_{mn}(\nu_k)$, is the Fourier transform pair of the average correlation function, $\bar{\rho}_{mn}(\tau_i)$ (Papoulis 1965), and $\bar{\mathbf{P}}(\nu)$ may be understood as the spectral density of the coherency matrix, $\boldsymbol{\rho} = \bar{\boldsymbol{\rho}}(0)$. Now, in general, the magnitude of the cross correlation, $|\rho_{12}(\tau_i)|$, is a small fraction of the total intensity. Therefore ρ_{12} (and $\rho_{21} = \rho_{12}^*$) will not be affected by the sharp non-linearity in response, $\check{\rho}(\rho)$ (Jenet & Anderson 1998, Figure 1), that occurs in the region, $\rho \gtrsim 0.9$, where $\check{\rho}$ and ρ are the digitized and undigitized normalized correlation functions, respectively.

However, the normalized auto-correlations, $\rho_{11}(\tau)/\rho_{11}$ and $\rho_{22}(\tau)/\rho_{22}$, are equal to 1 at $\tau = 0$ (by definition) and suffer from an additional digitization artifact known as scattered power. The coherency products, $\bar{P}_{11}(\nu_k)$ and $\bar{P}_{22}(\nu_k)$, may be "scattered power corrected" using the technique described by Jenet & Anderson (1998) and the values of M retained during the dynamic output level setting stage (Section 2.4.1). These are used to approximate the slope,

$$A = \left.\frac{d\check{\rho}}{d\rho}\right|_{\rho=0} \tag{2.23}$$

for each of the two autocorrelation products. It should be noted that this correction is performed before any averaging of the detected time-samples occurs.

Time-averaging is performed as a function of topocentric pulse phase during a process commonly called folding. Apparent topocentric pulse phase is determined using a polynomial approximation to the pulsar timing model, $\mathcal{P}_\phi(t)$, generated using the `tempo` software package (http://pulsar.princeton.edu/tempo; see also Taylor & Weisberg (1989)). The time-series of interest, $Y(t_i)$, is folded by integrating each of its samples into one of n equally spaced phase bins, $Y(\phi_k)$, where bin number, k, is given by

$$k = (n\mathcal{P}_\phi(t_i)) \bmod n, \tag{2.24}$$

so that $0 \le k < n$. Here, $\mathcal{P}_\phi$ has dimensionless phase (turns) and the mod operator returns the remainder after division.

Normally, a number of time-series, Y_i (such as all of the four Stokes parameters in each of the N_c sub-bands), will be folded in parallel with one count, $N(\phi_k)$, of the number of time-samples accumulated in each phase bin. The average pulse profile of each process is then given by

$$\langle Y_i(\phi_k)\rangle = Y_i(\phi_k)/N(\phi_k). \tag{2.25}$$

The start and end times, t_0 and t_N, of the integrated data are used to assign the mean time of the zero phase bin, given by

$$\tau_0 = \mathcal{P}_\phi^{-1}(\mathcal{P}_\phi((t_0 + t_N)/2) \bmod 1) \tag{2.26}$$

Under the assumption that the polynomial, $\mathcal{P}_\phi$, and its inverse may be calculated to arbitrarily high accuracy, the accuracy of τ_0 is given by the accuracy of the observatory sampling clock.

An overview of the data reduction process described in this section is presented in Figure 2.7. Following the flow of this diagram, the digitized data are played back from magnetic tape (DLT 7000 or S-VHS) using an automatic data transfer system (DLT 7000 tape robot and control software or S2-TCI) and written to storage devices mounted on the workstation cluster. The two-bit data are later read from disk and sent in large segments to multiple processing nodes via high-speed ethernet. On

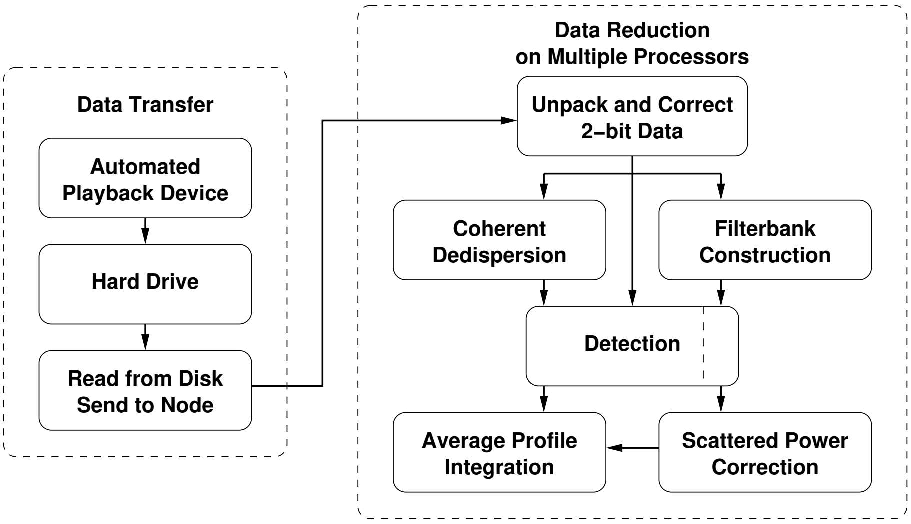

Figure 2.7: Overview of baseband data reduction. As indicated by the dashed line in the Detection stage, scattered power correction may be performed only when a synthetic filterbank has been constructed.

each node, the data are converted to a floating point representation of the voltage waveform received at the telescope, and corrected for non-linearity of the digitization process. Following completion of this procedure, a number of data reduction options are available. The signal may be detected, or coherently dedispersed, or a synthetic filterbank may be formed. During filterbank construction, each sub-channel may be simultaneously dedispersed. Data are then detected, producing either the total intensity, the Stokes parameters, or the coherency matrix, as desired. After detection of the coherency matrix, filterbank data may be further corrected for the scattered power digitization artifact. The detected timeseries are then folded by averaging the samples modulo the topocentric pulse period.

The above process results in an uncalibrated average pulse profile. As described in the following chapter, each resulting pulse profile is fitted to a standard template in order to measure the pulse time of arrival. From these arrival time estimates are derived the physical information of interest in a pulsar timing experiment.

Chapter 3

Arrival Time Analysis

3.1 Arrival Time Estimation

The process described in the previous section produces an uncalibrated pulse profile averaged over some arbitrary length of time. For CPSR, the standard size of one raw data file is 1 GB, equivalent to approximately 53.7 s of recording time. A 32-channel synthetic filterbank was used to reduce a large portion of the data, and each 53.7 s, 32-channel archive was written to disk and stored for later analysis. There are a number of advantages to maintaining a relatively short time interval for archived data. For instance, archives may be corrupted by spurious effects, such as wide-band RFI; and shorter integrations may be discarded at a later stage without serious loss of data. Certain observational parameters, such as the parallactic angle, may also vary with time and result in changes to the polarimetric pulse profile. When averaged over a sufficiently long timescale, irreversible corruption such as depolarization may take place. Also, when timing a relatively new pulsar, the ephemeris on which the polynomial, $\mathcal{P}_\phi(t)$ (see Section 2.4.4), is based may not accurately reflect the physical parameters of the pulsar system. In this case, $\mathcal{P}_\phi(t)$ may drift and no longer represent the actual topocentric pulse phase, resulting in smearing of the integrated pulse profile on longer timescales. By maintaining shorter integration lengths, effects due to parallactic angle rotation and $\mathcal{P}_\phi$ drift may be corrected before further integrating in time.

In general, the average total intensity pulse profile is utilized for the purposes of pulsar timing. However, as discussed in Section 5.2, the total intensity (or Stokes I) may be corrupted by instrumental mixing with the other Stokes parameters. High-precision timing is therefore intrinsically dependent upon high-precision polarimetric calibration. Alternatively, calibration may be robustly circumvented by forming an average pulse profile based on the polarimetric invariant interval (Britton 2000),

$$S_{\rm inv}^2 = \mathrm{I}^2 - \mathrm{Q}^2 - \mathrm{U}^2 - \mathrm{V}^2. \tag{3.1}$$

which remains invariant under those linear transformations of the electric field vector

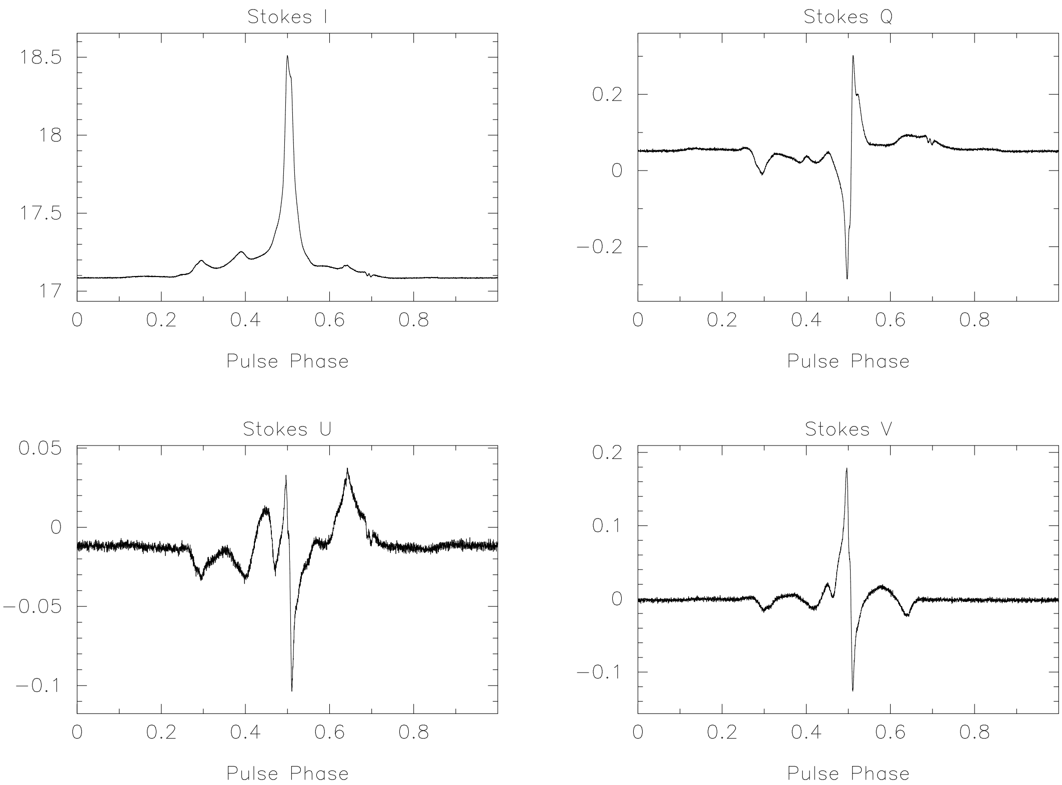

Figure 3.1: Average Stokes parameters as a function of pulse phase at 1413 MHz, integrated over approximately 4.6 hours. Polarimetric calibration was performed using the phase-coherent matrix convolution technique introduced in Section 5.2. Note that the off-pulse baseline in each of the profiles (approximately 17.1 uncalibrated flux units in Stokes I) is due to the system temperature.

commonly encountered in radio astronomy. The mean invariant profile, $\langle S_{\rm inv}(\phi_k)\rangle$, will remain unaffected by changes in the system response, including (among many other factors) the rotation of the receiver feeds with respect to the sky, or parallactic angle, ψ_I. Note that each of the Stokes parameters (I,Q,U,V) consists of the sum of the pulsar signal and the system temperature, $T_{\rm sys}$ (see Figure 3.1). Consequently, the $T_{\rm sys}$ baseline must be removed from each of the Stokes parameter profiles before calculation of the invariant interval.

The mean invariant profile, $\langle S_{\rm inv}(\phi_k)\rangle$, is formed in each of the 32 sub-bands of each 53.7 s archive before removing the inter-channel dispersion delay and further integrating in frequency and time, producing single-channel, hour-long average invariant profiles. A selection of these hour-long integrations was chosen to be further integrated into a high signal-to-noise standard, $\langle {\rm S}(\phi_k)\rangle$, representing the mean profile from ~ 100 hours of observing time. Each hour-long integrated profile, $\langle {\rm P}_j(\phi_k)\rangle$, represents a noisier version of the standard, and may be modeled as

$$\langle {\rm P}_j(\phi_k)\rangle = \Delta T_{\rm sys} + b\langle {\rm S}(\phi_k - \phi)\rangle + \sigma(\phi_k), \tag{3.2}$$

where $\Delta T_{\rm sys}$ is the offset in system temperature (or baseline) between the standard and the profile, b is an intensity scale factor, ϕ is the phase shift required to align the profile and the standard, and $\sigma(\phi_k)$ is a Gaussian noise function. Estimates of $\Delta T_{\rm sys}$, b, ϕ, and the formal errors in each of these estimates are obtained by a least-squares fit in the Fourier domain (Taylor 1992).

From the pulse phase shift, ϕ, an estimate of the pulse time-of-arrival (TOA) is simply given by $\tau = \tau_0 + \phi P$, where τ_0 is the epoch of the zero phase bin, as in Equation 2.26, and P is the mean topocentric pulse period. The theoretical TOA estimation error, $\sigma_{i(\tau)}$, is approximately given by

$$\sigma_{i(\tau)} \approx \frac{1}{2}\frac{Pw}{S/N}, \tag{3.3}$$

where P and w are the pulse period and duty cycle, respectively, and S/N is proportional to the intensity of the pulsar signal (see Equation 2.6). For PSR J0437−4715, the average estimated error for each hour-long integration is around 100 ns. A set of pulse arrival times with formal error estimates, $\mathcal{T} = \{\tau_i, \sigma_{i(\tau)}\}$ was produced for PSR J0437−4715 using each of the hour-long average invariant profiles over a 3.4 year time-span.

3.2 The Timing Model

Physical parameters of the PSR J0437−4715 system are derived from the arrival time data by fitting them to a timing model using least-squares minimization. The timing model begins with a description of the spinning pulsar and incorporates the various delays experienced by the pulsed radiation during its propagation from the pulsar to earth. Pulse phase as a function of the proper time in the pulsar reference frame, T, is simply given by the Taylor series expansion,

$$\phi(T) = \phi_0 + \nu(T - T_0) + \frac{1}{2}\dot{\nu}(T - T_0)^2 + \frac{1}{6}\ddot{\nu}(T - T_0)^3 + \ldots, \tag{3.4}$$

where ϕ_0 is the pulse phase at time, T_0, $\nu = 1/P$ is the mean pulse (or spin) frequency, $\dot{\nu}$ is its first time derivative, etc.

The arrival time estimates, $\mathcal{T}$, are made in the reference frame of the observatory sampling clock, or topocentric reference frame. It is in modeling the transformation of topocentric time to proper time at the pulsar that most of the information of physical interest is derived from $\mathcal{T}$. To first order, the transformation depends solely on the geometric distance between Earth and the pulsar, and the time required for the radiation to travel this distance. In order to calculate this distance and remove the kinematic effects of the Earth's motion, the position of the observatory, $\boldsymbol{r}$, is conventionally specified with respect to the inertial reference frame of the Solar System barycentre (SSBC). The pulsar's position, $\boldsymbol{r}_p$, is given with respect to the binary system barycentre (BSBC). (In the case of a solitary pulsar, $\boldsymbol{r}_p$=0.) The vector pointing from the SSBC to the BSBC is specified by $\boldsymbol{d}=d\boldsymbol{K_0}$, where d is the distance between the SSBC and BSBC and $\boldsymbol{K_0}$ is a unit vector pointing in the direction of the pulsar, as defined by the right ascension, α, and declination, δ. The geometric distance between the pulsar and observatory is therefore simply given by $D_G = |\boldsymbol{d} + \boldsymbol{r_p} - \boldsymbol{r}|$. The vector, $\boldsymbol{d}$, is of course much larger than either of $\boldsymbol{r_p}$ or $\boldsymbol{r}$, and the distance may be approximated by (Kopeikin 1995)

$$D_G \simeq d - \boldsymbol{r}\cdot\boldsymbol{K_0} + \boldsymbol{r_p}\cdot\boldsymbol{K_0} + \frac{1}{2d}[(\boldsymbol{r}\times\boldsymbol{K_0})^2 + (\boldsymbol{r_p}\times\boldsymbol{K_0})^2] - \frac{1}{d}(\boldsymbol{r}\times\boldsymbol{K_0})(\boldsymbol{r_p}\times\boldsymbol{K_0}). \quad (3.5)$$

In general, the distance to the pulsar, d, is unknown and the first term may be dropped from consideration by redefinition of ϕ_0 in Equation 3.4. Note that any $\dot{d}$ will simply manifest itself as an unknown Doppler shift of the measured spin period and, if applicable, measured orbital period. The geometric propagation time delay under consideration is therefore given by $\Delta_G = (D_G - d)/c$, where c is the speed of light. The second and third terms in Equation 3.5 result in the Roemer delays, $\Delta_{R\odot}$ and Δ_{Rp}, in the Solar System and pulsar binary system, respectively. The fourth term is the annual (trigonometric) parallax, the fifth term is the orbital parallax, and the last term, known as the annual-orbital parallax (Kopeikin 1995), will be discussed in more detail below. Notice that all of the parallax terms become less significant as the distance to the pulsar increases. In fact, no pulsar timing experiment has yet been reported to include a determination of the orbital parallax of a binary system, and the measurement of annual-orbital parallax presented by van Straten et al. (2001) is the first and only such detection to be made to date.

The proper motion of the pulsar, $\boldsymbol{\mu} = (\mu_\alpha \equiv \dot{\alpha}\cos\delta, \mu_\delta \equiv \dot{\delta})$, causes the unit vector, $\boldsymbol{K_0}$, to vary with time. This variation results in a position error that grows linearly with time, most significantly manifesting itself as a changing Solar System Roemer delay, $\Delta_{R\odot}$. Recently, Kopeikin (1996) demonstrated that the changing binary system Roemer delay, Δ_{Rp}, will be significant for pulsars with large proper motion. The secular evolution of Δ_{Rp} manifests itself as a change in the projected binary system parameters, as discussed below.

The position of the observatory with respect to the SSBC, $\boldsymbol{r}$, must be known with great accuracy for the purposes of high-precision pulsar timing. The Earth's barycentric position, $\boldsymbol{r}_\oplus$, is calculated using the DE200 Solar System ephemeris (Standish 1990) maintained by NASA's Jet Propulsion Laboratory (JPL). The vector pointing from the Earth's centre of mass to the observatory is calculated using the position of the telescope in the International Terrestrial Reference Frame (ITRF), as determined using geodetic Very Long Baseline Interferometry (VLBI), and the Earth's rotation angle about the pole, UT1. The International Earth Rotation Service (IERS) maintains a table of TAI-UT1 corrections, published monthly in the IERS *Bulletin B*. These are retroactively applied to the determination of $\boldsymbol{r}$.

In addition to the geometric time delay in the Solar System, the masses of the Sun and planets result in general relativistic propagation effects. The timing model must therefore calculate and compensate for both the Einstein delay, $\Delta_{E\odot}$, arising from gravitational redshift and time dilation effects, and the Shapiro delay, $\Delta_{S\odot}$, due to the retardation of light in warped spacetime.

In the case of a binary system, the pulsar's position, $\boldsymbol{r}_p$, may be modeled to yield information about the nature of its orbit. The conventional three-dimensional description of a binary orbit is specified using seven Keplerian orbital parameters: the semi-major axis of the orbital ellipse, a; the eccentricity of the orbital ellipse, e; the orbital inclination, i; the longitude of the ascending node, Ω; the longitude of periastron, ω; the epoch of periastron, T_0; and the orbital period, P_b. However, astrometric observations generally provide only partial information about the binary motion of a star. For instance, in a visual binary, motion may be measured only in the projection of the orbit onto the plane of sky. For spectroscopic and radio pulsar binaries, it is possible to detect only stellar motion along of the line of sight. Consequently, a complete three-dimensional description of a stellar binary system is not generally possible. In pulsar timing experiments, the rotation about the line of sight, Ω, is omitted from the model and both i and a are absorbed into the projected semi-major axis, $x = a\sin(i)$. The five remaining Keplerian orbital parameters describe a classical binary system that may be readily determined from a first order Doppler analysis of the arrival time data.

When only the projected semi-major axis, x, is known, Kepler's third law may be re-expressed in terms of x and related to the component masses by Newton's law, producing the mass function,

$$f(m_p, m_c, i) = \frac{4\pi^2}{G}\frac{x^3}{P_b^2} = \frac{(m_c \sin i)^3}{(m_p + m_c)^2}, \tag{3.6}$$

where m_p is the mass of the pulsar and m_c is the mass of the companion. Given only the mass function, the component masses remain unknown due to the undetermined inclination angle. However, a minimum companion mass may be derived by assuming a minimum pulsar mass and setting $\sin i = 1$.

As mentioned in Section 1.4, the component masses may in some cases be determined by measurement of two or more general relativistic effects in the binary system. Relativistic corrections to the timing model may be applied in a theory-independent manner using the post-Newtonian treatment introduced by Damour & Deruelle (1986). Their model (hereafter, the DD model) incorporates various post-Keplerian orbital parameters, such as the orbital period derivative, $\dot{P}_b$, and the advance of periastron, $\dot{\omega}$. It also includes the Shapiro delay induced by the pulsar companion, Δ_S, parameterized by the shape, $s \equiv \sin(i)$, and range, $r \equiv Gm_2/c^3$, where m_2 is the mass of the companion.

With the binary motion thus parameterized, $\boldsymbol{r}_p$, may be calculated as a function of time and substituted into the expression for Δ_G. The transformation from pulsar proper time, T, to proper time at the observatory, τ, is then given by

$$T = \tau - \tau_0 - \Delta_G + \Delta_{E\odot} + \Delta_{S\odot} + \Delta_S \tag{3.7}$$

Substitution of T into Equation 3.4 produces the timing model, $\phi(\tau)$. Physical parameters of the system are derived from $\mathcal{T}$ by minimizing the objective function,

$$\chi^2 = \sum_{i=1}^{N} \left(\frac{\phi(\tau_i) - n_i}{\sigma_i} \right)^2 , \tag{3.8}$$

where $n_i = ([\phi(\tau_i){+}0.5] \mod 1)$ is the nearest integer pulse number at τ_i and $\sigma_i = \sigma_{i(\tau)}/P$. The timing model (Taylor & Weisberg 1989) and least-squares fitting algorithm is implemented in the program, `tempo`, maintained by the Princeton and ATNF pulsar groups (http://pulsar.princeton.edu/tempo). Written in Fortran 77, `tempo` performs the retroactive clock and observatory position corrections, and implements various different models to describe the pulsar binary system. However, the last two terms in Δ_G (the orbital and annual-orbital parallaxes) are largely insignificant in most pulsar timing experiments, and they are not included in `tempo` by default. Therefore, the DD model was extended to include the effects of both the annual-orbital parallax (Kopeikin 1995) and the changing binary system Roemer delay caused by proper motion (Kopeikin 1996).

The annual-orbital parallax manifests itself as an annual, periodic variation of both the projected semi-major axis, x, and the longitude of periastron, ω, such that:

$$x^{\rm obs}(t) = x^{\rm int}[1 - \frac{\cot i}{d} \boldsymbol{J'} \cdot \boldsymbol{r}(t)], \tag{3.9}$$

$$\omega^{\rm obs}(t) = \omega^{\rm int} - \frac{\csc i}{d} \boldsymbol{I'} \cdot \boldsymbol{r}(t), \tag{3.10}$$

where $\boldsymbol{I'} = \cos\Omega \boldsymbol{I_0} + \sin\Omega \boldsymbol{J_0}$, $\boldsymbol{J'} = -\sin\Omega \boldsymbol{I_0} + \cos\Omega \boldsymbol{J_0}$, (and $\boldsymbol{K'} = \boldsymbol{K_0}$) are the basis vectors in the reference frame rotated by Ω about the line of sight, $\boldsymbol{K_0}$. For the definitions of the commonly-used triad of basis vectors, ($\boldsymbol{I_0}$, $\boldsymbol{J_0}$, $\boldsymbol{K_0}$), consult Figure 4.1, where $\boldsymbol{\Omega'} = -\boldsymbol{J'}$. Note that the superscripts "obs" and "int" refer to the observed and intrinsic values, respectively. The proper motion results in secular evolution of x and ω, such that the observed values are described by:

$$x^{\rm obs}(t) = x^{\rm int}[1 + \cot i \, \boldsymbol{J'} \cdot \boldsymbol{\mu}(t - t_0)], \tag{3.11}$$

$$\omega^{\rm obs}(t) = \omega^{\rm int} + \csc i \, \boldsymbol{I'} \cdot \boldsymbol{\mu}(t - t_0). \tag{3.12}$$

Equations 3.9 to 3.12 were added to `tempo` by implementing a new binary model, called the Damour, Deruelle, and Kopeikin (DDK) model. This addition necessitated the introduction of two new model parameters: the longitude of the ascending node, Ω (new `tempo` key-word: `KOM`); and the orbital inclination, i (new `tempo` key-word: `KIN`). Note that, because i may vary from 0 to π radians in a full, three-

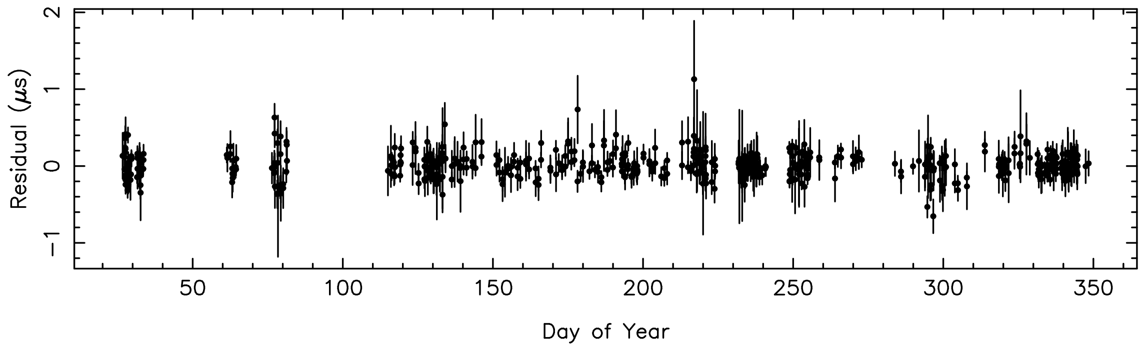

Figure 3.2: Day-of-year arrival time residuals of data taken between July 1997 and December 2000 and fit using the DDK model. The intensive, almost daily, coverage starting at approximately day 115 is a result of the regular timing observations made by the Parkes Observatory staff since the beginning of May 2000.

dimensional model of the pulsar orbit, the shape parameter, $s \equiv \sin(i)$ (`tempo` key-word: `SINI`), no longer sufficiently describes the orientation. Therefore, the `SINI` parameter is ignored in the DDK model, and the shape is calculated from the value of i specified by `KIN`. Also, when using the DDK model, only Equations 3.9 and 3.10 are active by default. To activate Equations 3.11 and 3.12, the `K96` flag must be enabled (with a corresponding value of 1) in the `tempo` parameter file.

The longitude of the ascending node, Ω, defines the orientations of $\boldsymbol{I'}$ and $\boldsymbol{J'}$, thereby determining the day-of-year when $\boldsymbol{J'} \cdot \boldsymbol{r}$ reaches its maximum in Equation 3.9. The annual-orbital parallax timing signature therefore provides a direct constraint on Ω that greatly benefits from excellent day-of-year coverage of arrival time estimates (see Figure 3.2). Furthermore, under certain circumstances, the `K96` flag can be used to constrain the relationship between i and Ω:

1. First, general relativistic and other contributions to $\dot{x}$ must be negligible; so that the observed $\dot{x}$ is dominated by the system's proper motion contribution, as calculated in Equation 3.11.

2. Second, $\dot{x}$ and $\boldsymbol{\mu}$ must be measurable; the accuracy of their estimation determines the degree to which i and Ω may be constrained.

Under these circumstances, which will be called the "$i(\Omega)$ conditions", the `K96` flag may be enabled and the `XDOT` model parameter omitted in the `tempo` parameter file, forcing the timing model to compensate for the observed $\dot{x}$ signature through Equation 3.11. Given the separately determined and non-covariant estimations of $\boldsymbol{\mu}$ and Ω, the correct $\dot{x}$ can be achieved only by proper choice of i. Therefore, Equations 3.9 through 3.12 may be used to provide a purely geometric constraint on the inclination angle in binary systems with small intrinsic $\dot{x}$.

3.3 Modeling Results

The fitting procedure implemented by `tempo` is used to yield estimates of the physical parameters of the PSR J0437−4715 system, including their formal one sigma (1σ) errors. Before development of the DDK model, the best-fit parameters from the DD model were used to provide preliminary estimations of the expected values of certain post-Keplerian parameters, such as $\dot{x}$ and $\dot{P}_b$. The general theory of relativity predicts that (Taylor & Weisberg 1982)

$$\dot{P}_b^{\rm gr} = -\frac{192\pi}{5}\, T_\odot^{5/3} n^{5/3} f(e)\, m_p\, m_c\, M^{-1/3}, \tag{3.13}$$

and

$$\dot{\omega}^{\rm gr} = 3\, T_\odot^{2/3} n^{5/3} (1-e^2)^{-1} M^{2/3}, \tag{3.14}$$

where m_p and m_c are the masses of the pulsar and its companion, respectively, $M = m_p + m_c$ is the total system mass, $n = 2\pi/P_b$ is the orbital angular frequency, $T_\odot \equiv GM_\odot/c^3 = 4.925490947\mu$s is a commonly used constant, and

$$f(e) = (1-e^2)^{-7/2}\left(1 + \frac{73}{24}e^2 + \frac{37}{96}e^4\right). \tag{3.15}$$

Assuming that relativistic spin-orbit coupling is negligible, $\dot{x}$ may be related to $\dot{P}_b$ by simple application of Kepler's Third Law ($P_b^2 \propto x^3$), so that

$$\dot{x}^{\rm gr} = \frac{2}{3}\frac{x}{P_b}\dot{P}_b^{\rm gr}. \tag{3.16}$$

Substituting the binary parameters from the DD model in Table 3.1 yields: $\dot{P}_b^{\rm gr} = -4.1 \times 10^{-16}$, $\dot{\omega}^{\rm gr} = 0.017^\circ{\rm yr}^{-1}$, and $\dot{x}^{\rm gr} = -1.8 \times 10^{-21}$. The observed value, $\dot{x} = (7.88 \pm 0.01) \times 10^{-14}$, is many orders of magnitude larger than the general relativistic contribution, and the first $i(\Omega)$ condition (see the end of Section 3.2) is satisfied. The accuracies with which the observed $\dot{x}$ and $\boldsymbol{\mu} = (\mu_\alpha, \mu_\delta)$ are determined (see Table 3.1) satisfy the second $i(\Omega)$ condition. Therefore, the DDK model may be used with the `K96` flag in order to constrain the relationship between i and Ω. In fact, in the PSR J0437−4715 system, the proper motion vector is nearly parallel to $\boldsymbol{J'}$, so that $\delta i/\delta\Omega$ is close to zero, and i may be estimated with much greater accuracy than that of Ω. The precision of the Ω estimate is in turn improved by the excellent day-of-year coverage of the arrival time data (see Figure 3.2).

The partial derivatives of χ^2 (Equation 3.8) with respect to i and Ω are small, and the curvature of the χ^2 surface is not constant. Therefore, the $\Delta\chi^2 \equiv \chi^2(\Omega, i) - \chi^2_{\rm min}$ surface is mapped in the vicinity of the global minimum, $\chi^2_{\rm min}$, as shown in Figure 3.3. Here, $\chi^2(\Omega, i)$ is the value of χ^2 minimized by variation of the remaining model parameters, given constant i and Ω. Projections of the $\Delta\chi^2 = 1$ contour provide the 1σ confidence intervals of i and Ω included in Table 3.1.

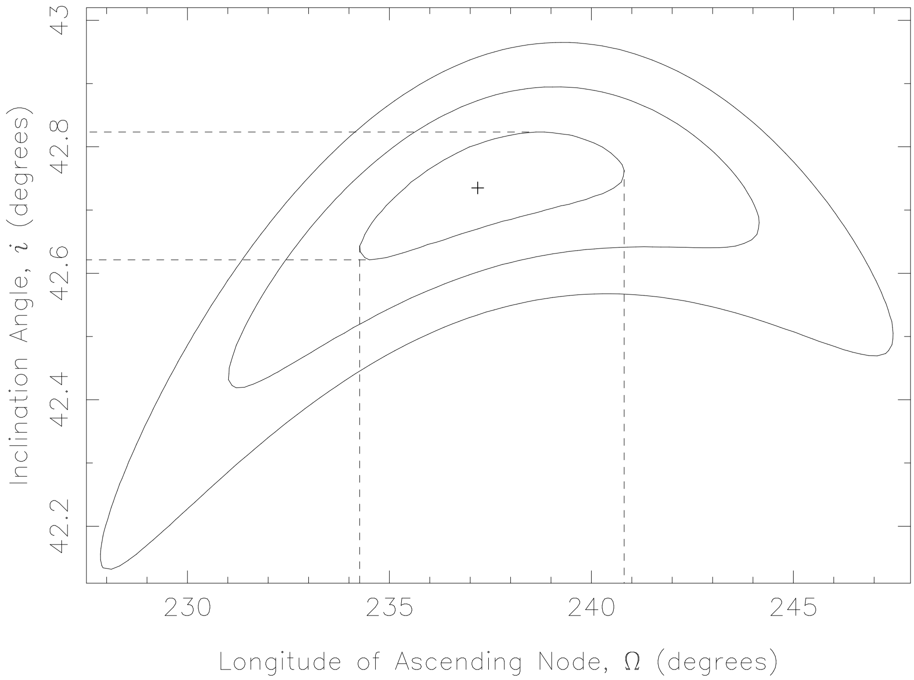

Figure 3.3: Contour map of $\Delta\chi^2(\Omega, i)$ in the vicinity of the global minimum. Moving outward from the global minimum, marked with a '+' (plus) sign, the contour lines map $\Delta\chi^2$ equal to 1, 4 and 9. Projections of the $\Delta\chi^2 = 1$ contour onto the i and Ω axis provide the 1σ confidence intervals for each parameter.

In addition to providing best-fit model parameters, `tempo` also outputs a table of arrival time residuals, given by $R_i = (\phi(\tau_i) \bmod 1)$. These may be investigated for obvious departures from the timing model or, as discussed in Section 3.3.1, non-Gaussian statistical behaviour. One commonly found systematic error is due to poor polarimetric calibration, which primarily manifests itself in our data as a variation of TOA with parallactic angle, ψ_I (see Figure 3.4). It was expected that the formation of the invariant profile, $\langle S_{\rm inv}(\phi_k)\rangle$, would eliminate most polarimetric corruption of the arrival time estimates. However, $S_{\rm inv}$ remains invariant only under transformation by a system with linear response and, in late January 2000, it was discovered that a failure in the FFD was resulting in less than optimal two-bit sampling of the baseband signal. The resulting non-linear distortion of the polarimetric profile cannot be treated by formation of the invariant profile and is non-invertible. However, the functional form of the residual parallactic angle dependence may be approximated using a polynomial expression. The TOA data from observations made between 17 March and 27 October 1999 were corrected by removing the polynomial,

$$R_1(\psi_I) = (-5.815\times10^{-3}\psi_I - 3.042\times10^{-4}\psi_I^2 + 7.571\times10^{-7}\psi_I^3 + 1.870\times10^{-8}\psi_I^4)\,\mu\mathrm{s},$$

where ψ_I is the parallactic angle in degrees, and $R_1(\psi_I)$ (shown in Figure 3.4) is found by a least-squares fit to the arrival time residuals.

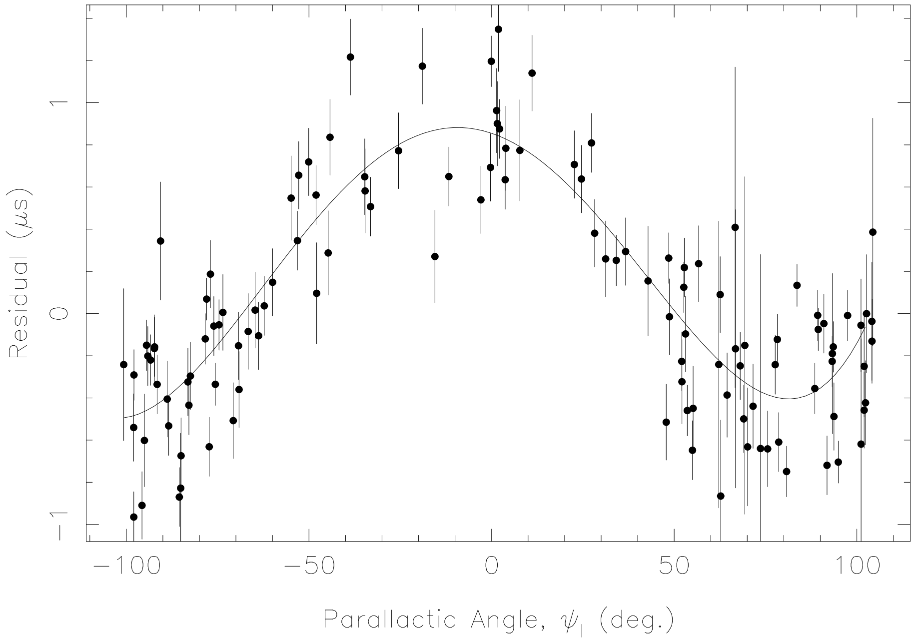

Figure 3.4: Corrupted arrival time residuals as a function of parallactic angle, ψ. Data were obtained between 17 March and 27 October, 1999, using the CPSR 20 MHz bandpass centered at 1413 MHz, with a faulty digitizer board (FFD). Each arrival time estimate is derived from an hour-long integration of the invariant profile and is plotted with its 1σ error bar. The solid line is the best-fit polynomial, $R_1(\psi_I)$, used to remove the systematic trend from the arrival time data.

A replacement FFD was installed in CPSR and tested during the mid-March 2000 observing run. Since this repair, online monitoring software has been used to maintain optimal sampling thresholds at record time for all CPSR observations. This careful attention to sampling optimization has proved to be rewarding, as shown by comparison of Figures 3.4 and 3.5. However, as evident in Figure 3.5, there still remains some parallactic angle dependence of the arrival time residuals after the repair. These data were therefore also corrected by removing a second polynomial,

$$R_2(\psi_I) = (1.532 \times 10^{-3}\psi_I - 7.799 \times 10^{-5}\psi_I^2 - 2.024 \times 10^{-7}\psi_I^3 + 4.215 \times 10^{-9}\psi_I^4)\,\mu\text{s},$$

that is smaller than, but similar to, the first. Each of $R_1(\psi_I)$ and $R_2(\psi_I)$ include a constant offset that is not shown in the above expressions because the difference is absorbed by the `JUMP` parameters included in the model fit performed by `tempo`. A total of 4 jumps are included in the fit, as detailed in Figure 3.6. The consequences of these required jumps and some conjecture regarding the inviolability of the invariant profile and the failure to completely eliminate the systematic distortion of arrival time estimates is discussed in Section 6.1.1.

A second round of model-fitting the corrected TOAs produces the final results presented in Table 3.1. As no other model parameter is covariant with ψ_I, it is expected that this correction should serve only to reduce the residual RMS, σ_τ.

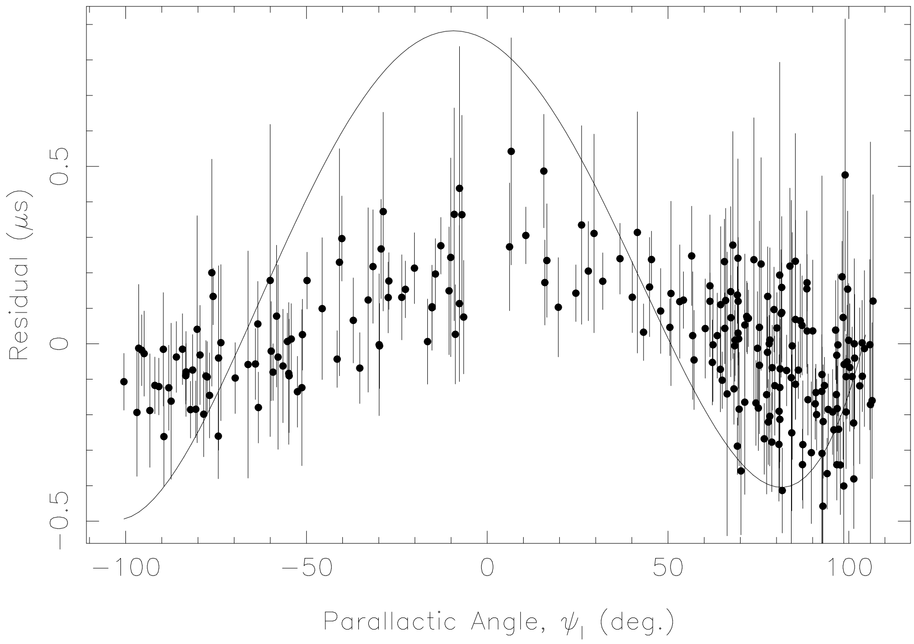

Figure 3.5: Arrival time residuals as a function of parallactic angle, ψ, after repair of the FFD board. Data were obtained using the CPSR 20 MHz bandpass centered at 1413 MHz. Each arrival time estimate is derived from an hour-long integration of the invariant profile and is plotted with its 1σ error bar. Shown only for comparison, the solid line is the polynomial, $R_1(\psi_I)$, used to remove the systematic trend from the corrupted arrival time data presented in Figure 3.4.

For the purposes of comparison, Table 3.1 includes the best-fit parameters determined using three different binary models: the Blandford & Teukolsky (1976) model (BT), the Damour & Deruelle (1986) model (DD), and the Damour, Deruelle, and Kopeikin model (DDK). When using the DD model, $\sin(i)$ is poorly constrained, and the `SINI` parameter is set using the best-fit value of i, as determined using the DDK model. In order to constrain i geometrically, the DDK model is used with the `K96` option enabled and the `XDOT` parameter is set to zero (as described above). Except for the estimates of $\dot{\omega}$, all of the binary parameters derived from the DD and DDK models agree within their 1σ uncertainties. Though the $\dot{\omega}$ values are within 1.5σ of each other, it is noted that the estimate derived using the DDK model agrees more closely with the general relativistic prediction. Indicating the validity of the DDK solution, its arrival time residual RMS, σ_τ, is approximately 25 ns ($\sim 16\%$) less than that of the DD model, and the DDK χ^2 has dropped by 300 ($\sim 30\%$) with the addition of only two degrees of freedom (N_{free}). Note that both the DD and DDK models are expected to disagree with the BT model-derived binary parameters, as the BT model does not include the effect of the Shapiro delay. Also, the estimates of second period derivative, $\ddot{P}$, are neither statistically significant nor required in order to achieve the χ^2 shown. They are included in the fit only for the purposes of discussing an upper limit to the timing noise in our data (see Section 6.1.2).

Table 3.1: Best-fit parameters determined using three binary models

Model	BT	DD	DDK
		Astrometric Parameters	
Epoch (MJD)	51194	51194	51194
P (ms)	5.757451831071979(8)	5.757451831071982(8)	5.757451831072006(8)
$\dot{P}$ (10^{-20})	5.72910(5)	5.72904(5)	5.72906(5)
$\ddot{P}$ (10^{-32})	-3.3(1.7)	-0.4(1.7)	1.2(1.7)
α (J2000.0)	$04^{\rm h}37^{\rm m}15\overset{\rm s}{.}7865126(8)$	$04^{\rm h}37^{\rm m}15\overset{\rm s}{.}7865144(8)$	$04^{\rm h}37^{\rm m}15\overset{\rm s}{.}7865147(7)$
δ (J2000.0)	$-47°15'08\overset{''}{.}46160(1)$	$-47°15'08\overset{''}{.}46160(1)$	$-47°15'08\overset{''}{.}46158(1)$
μ_α (mas yr^{-1})	121.446(6)	121.435(6)	121.438(6)
μ_δ (mas yr^{-1})	-71.447(8)	-71.449(8)	-71.436(8)
π (mas)	7.46(14)	7.39(14)	7.17(14)
		Binary Parameters	
$P_{\rm b}$ (days)	5.741044(3)	5.741043(3)	5.741046(3)
x (s)	3.366693430(8)	3.3666914(9)	3.36669155(14)
e (10^{-5})	1.9199(5)	1.9182(5)	1.9186(5)
T_0 (MJD)	51194.6343(3)	51194.623(3)	51194.6238(8)
ω (°)	1.850(14)	1.17(16)	1.19(5)
Ω (°)	...	...	238(4)†
i (°)	...	...	42.75(9)†
sin(i)	...	0.67(11)	...
m_c (M$_\odot$)	...	0.26(17)	0.237(18)
$\dot{P}_{\rm b}$ (10^{-12})	3.56(20)	3.80(20)	3.64(20)
$\dot{x}$ (10^{-12})	0.07847(19)	0.07894(20)	...
$\dot{\omega}$ (°yr^{-1})	0.005(10)	0.002(10)	0.016(10)
		Derived Parameters*	
μ (mas yr^{-1})	140.903(7)	140.895(7)	140.891(7)
ϕ_μ (°)	120.468(3)	120.471(3)	120.466(3)
m_p (M$_\odot$)	...	1.8(2.1)	1.60(20)
d_π (pc)	134(2)	135(2)	139(3)
d_β (pc)	149(8)	159(8)	152(8)
β (10^{-20}s^{-1})	647(12)	652(12)	673(13)
$\dot{P}^{\rm int}$ (10^{-20})	2.01(7)	1.97(7)	1.86(8)
		Goodness of Fit*	
σ_τ (ns)	166	151	125
χ^2	1156	957	656
$N_{\rm free}$	596	594	596

$*$ parameter(s) not included in fit

† uncertainty determined using χ^2 map

The symbols used for each parameter are defined both in the main text and in Appendix B. Number(s) shown in parentheses represent the formal uncertainty in the last digit(s) quoted.

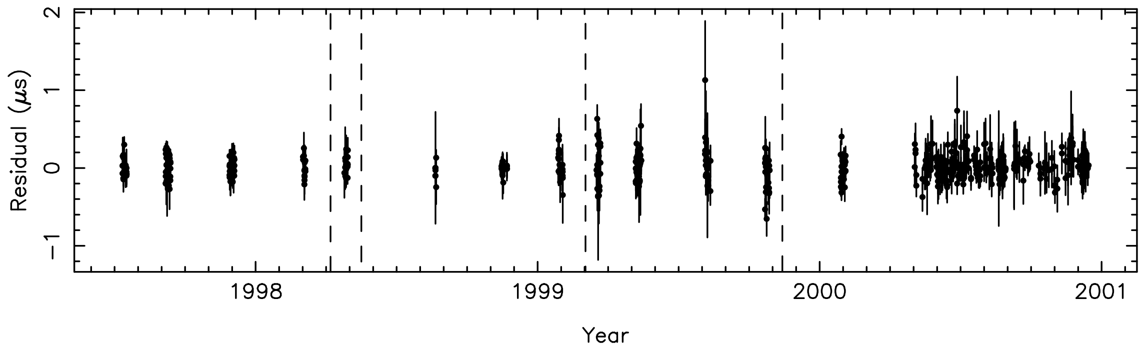

Figure 3.6: Best-fit arrival time residuals by epoch, as calculated using the DDK model. Four jumps (represented by vertical, dashed lines) are included in the fit, separating five sets of arrival time data. From left to right, the first and second sets of data were taken using the S2 with analog (S2-A) and digital (S2-D) filters, respectively. The remaining data were recorded using the CPSR. The fourth and fifth datasets were corrected for parallactic angle dependence using the polynomials, $R_1(\psi_I)$ and $R_2(\psi_I)$, respectively.

3.3.1 Analysis of Measurement Error

The model parameter estimates returned by the χ^2 minimization technique implemented by `tempo` are valid maximum likelihood estimators if and only if the arrival time measurement errors are normally distributed (Press et al. 1992, Section 15.6). The validity of the formal errors, as calculated using the covariance matrix produced during the minimization procedure, is also dependent upon the condition of random error. Departures from random, Gaussian experimental error may be detected by examination of the statistical properties of the post-fit arrival time residuals.

Following Taylor & Weisberg (1989), the normalized post-fit residual is defined as the post-fit residual divided by its estimated uncertainty. The histogram of normalized post-fit residuals presented in the plot on the left in Figure 3.7 reasonably approximates the Gaussian bell-curve shape, indicating normal measurement errors. A second test is provided by creating a new set of mean residuals, each formed by averaging n consecutive post-fit residuals, and calculating the RMS in the new set as a function of n. Data with normally distributed measurement errors will result in RMS $\propto n^{-1/2}$, as indicated by the line with slope equal to -0.5 in the plot on the right in Figure 3.7. The departure from this line beginning at RMS < 80 ns indicates non-Gaussian correlations between adjacent arrival time measurements, most likely due to systematic errors. The sources of systematic error might range from poor polarimetric response, resulting in correlations on the timescale of a day, to errors in the clock corrections and planetary ephemeris, which might result in correlations on the timescale of months or years. For instance, `tempo` currently does not include corrections for the Earth's polar motion. As this experiment is currently pushing the limits of high-precision pulsar timing, it is not surprising that systematic errors should dominate at the < 100 ns level.

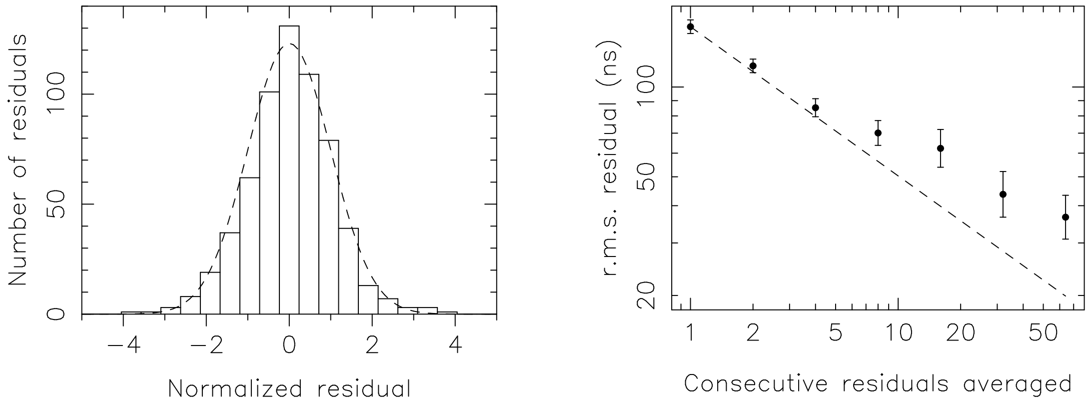

Figure 3.7: Statistical tests of measurement errors. The histogram on the left plots the approximately Gaussian distribution (shown with a dashed line) of normalized post-fit arrival time residuals. On the right, arrival time residual RMS is plotted versus the number of consecutive post-fit residuals averaged. The dashed line, with a slope of $-1/2$, indicates the behaviour expected from data with normally distributed measurement errors.

3.3.2 Discussion

It is expected that, on account of the accretion episode during which it was spun up to a millisecond pulsar, PSR J0437−4715's spin axis should be aligned with its orbital angular momentum. The orbital inclination angle, i, should therefore be equal to ζ, the angle between the pulsar spin axis and the line of sight (see Section 1.3). Under this assumption, the value of i presented in Table 3.1 compares well with the value of ζ estimated by polarimetric observations (Manchester & Johnston 1995) and by modeling the pulsed X-radiation light curve (Pavlov & Zavlin 1997). The estimation of i conflicts with the value of $\zeta \simeq 20°$ derived through the use of a relativistic rotating vector model that includes a polar cap populated by multiple, drifting emission regions which contribute to the average profile's conal components (Gil & Krawczyk 1997). However, nearly aligned magnetic and spin axes would allow continuous viewing of the neutron star polar cap region, which is thought to be the hot spot from which the thermal component of the X-radiation is emitted. Therefore, the Gil & Krawczyk (1997) result is difficult to reconcile with observations of the strongly modulated X-ray and Extreme Ultra-violet light curves (Danner, Kulkarni & Thorsett 1994; Edelstein, Foster & Bowyer 1995; Halpern, Martin & Marshall 1996; Zavlin et al. 2002), which imply that the polar cap rotates out of view with each turn of the pulsar. The assumption that $i \simeq \zeta$ obviates any apparent need to devise complicated emission models, such as the squeezed polar cap model (Chen, Ruderman & Zhu 1998), in order to resolve any seeming paradox.

In addition to the kinematic contributions to $\dot{x}$ and $\dot{\omega}$ described by Kopeikin (1996), the proper motion of a pulsar also causes a quadratic Doppler shift of the observed spin (Shklovskii 1970) and orbital (Damour & Taylor 1991) period derivatives, a phenomenon known as the Shklovskii effect. Although the pulsar's space velocity, $\boldsymbol{v}$, remains constant, the component of its velocity along the line of sight, $v_r = \boldsymbol{v} \cdot \boldsymbol{K_0}$, changes as the pulsar moves across the sky. The apparent change in radial velocity, v_r, can be trivially shown to be

$$\dot{v}_r = d\mu^2, \tag{3.17}$$

where $\mu = |\boldsymbol{\mu}|$ is the composite proper motion, and d is the distance to the pulsar. Now, the first three orders of Doppler effect are as follows:

$$T^{\text{obs}} = T^{\text{int}}(1 + \frac{v_r}{c}) \tag{3.18}$$

$$\dot{T}^{\text{obs}} = \dot{T}^{\text{int}}(1 + \frac{v_r}{c}) + T^{\text{int}}\frac{\dot{v}_r}{c} \tag{3.19}$$

$$\ddot{T}^{\text{obs}} = \ddot{T}^{\text{int}}(1 + \frac{v_r}{c}) + 2\dot{T}^{\text{int}}\frac{\dot{v}_r}{c} + T^{\text{int}}\frac{\ddot{v}_r}{c}, \tag{3.20}$$

where T is the period of interest (spin, P, or orbital, P_b), and c is the speed of light. As long as the radial velocity remains unknown, both the spin and orbital periods derived by modeling will contain an undetermined (linear) Doppler shift factor, given by $1 + v_r/c$. When both the distance (such as the parallax distance, d_π) and proper motion are determined, the apparent quadratic Doppler shift factor, $\beta = \dot{v}_r/c = d\mu^2/c$ may be calculated and used to correct the observed spin and orbital period derivatives, yielding their intrinsic values. Values of both β and the intrinsic spin period derivative, $\dot{P}^{\text{int}}$, are included in Table 3.1.

When the intrinsic period derivative is expected to be negligible, the observed period derivative may be used to calculate another distance estimate (Bell & Bailes 1996), $d_\beta = c\beta/\mu^2$, where $\beta \simeq \dot{T}/T$. For PSR J0437−4715, the observed orbital period derivative, $\dot{P}_b = (3.64 \pm 0.2) \times 10^{-12}$, is much larger than that expected due to the emission of gravitational waves (as discussed in Section 3.3) or other factors such as acceleration in the Galactic potential (discussed below) and the above condition holds. Estimates of the Bell & Bailes distance, d_β, derived from both $\beta = \dot{P}_b/P_b$ and the composite proper motion, μ, are included in Table 3.1. These estimates agree with the parallax distance to within approximately 1.5 σ. The precision of d_β is anticipated to improve with time as $t^{5/2}$, and will provide an independent distance estimate with relative error of approximately 1% within the next three to four years.

Other factors, such as those arising from Galactic differential rotation and gravitational acceleration of the pulsar in the Galactic potential, contribute to the quadratic Doppler shift of observed period derivatives. The z-component of Galactic gravitational acceleration, K_z, varies as a function of height, z, above the Galactic plane. This height may be estimated using the parallax distance and the Galactic latitude. The Galactic longitude and latitude of PSR J0437−4715 are $l = 253\overset{\circ}{.}394$ and $b = -41\overset{\circ}{.}964$, respectively, so that

$$z = d_\pi \sin b \simeq -93\,\text{pc}, \tag{3.21}$$

and $K_z \simeq 2.6 \times 10^{-11}$ m s^{-2} (Bahcall 1984, Figure 7). An expression for the Galactic differential rotation component along the line of sight, based on observable quantities, was derived by Damour & Taylor (1991),

$$g_R = -\frac{\Theta_0}{R_0}\left(\cos l + \frac{\lambda}{\sin^2 l + \lambda^2}\right), \tag{3.22}$$

where R_0 and Θ_0 are the Galactocentric distance and circular velocity of the Sun, respectively, and $\lambda = (d_\pi/R_0) - \cos l$. Substituting $R_0 = 7.7$ kpc, $\Theta_0 = 222$ km s^{-1} (Damour & Taylor 1991), and the values of l and d_π for PSR J0437−4715, produces $g_R \simeq -3.1 \times 10^{-12}$ m s^{-2}. Therefore, the Galactic kinematic contribution to the quadratic Doppler shift term is

$$\beta_{\rm galactic} = \frac{g_R}{c} - \frac{K_z \sin b}{c} \simeq (-1.0 + 5.9) \times 10^{-20}\ \mathrm{s}^{-1} = 4.9 \times 10^{-20}\ \mathrm{s}^{-1}, \tag{3.23}$$

approximately 140 times smaller than that due to proper motion.

After correcting for the Shklovskii effect, the intrinsic spin period derivative, $\dot{P}^{\rm int} = \dot{P}^{\rm obs} - \beta P = (1.86 \pm 0.08) \times 10^{-20}$, may be used to provide an improved estimate of the characteristic age of the pulsar,

$$\tau_{\rm c} = \frac{P}{2\dot{P}^{\rm int}} = 4.9 \pm 0.2\,\mathrm{Gyr}. \tag{3.24}$$

An independent age estimate is provided by the cooling age of the helium white dwarf companion, $\tau_{\rm w}$. From its apparent I magnitude (Danziger, Baade & Della Valle 1993) is obtained the absolute magnitude at the parallax distance, $\mathrm{M_I} = 13.7 \pm 0.2$. Using the white dwarf cooling curves of Hansen & Phinney (1998), and the estimate of the companion mass, $m_c = 0.236 \pm 0.017$ M$_\odot$, the cooling age is approximately, $\tau_{\rm w} \sim 4.0 - 4.3$ Gyr. This may be used to limit the initial spin period of the pulsar (Hansen & Phinney 1998),

$$P_0 = P\sqrt{1 - \tau_{\rm w}/\tau_{\rm c}} \sim 1.6 - 2.6\ \mathrm{ms}. \tag{3.25}$$

Following on the derivation of Equation 3.17, it is also trivial to show that

$$\dot{\mu} = -2\mu\frac{v_r}{d} \tag{3.26}$$

and

$$\ddot{v}_r = -3v_r\mu^2. \tag{3.27}$$

Equations 3.17 and 3.27 may be applied to Equation 3.20 to produce

$$\ddot{T}^{\rm obs} = \ddot{T}^{\rm int}(1 + \frac{v_r}{c}) + \frac{\mu^2}{c}(2\dot{T}^{\rm int}d - 3T^{\rm int}v_r), \tag{3.28}$$

so that both the proper motion and radial velocity contribute to the second period derivative. For PSR J0437−4715, if one assumes a generous radial velocity of $100\,\mathrm{km\,s^{-1}}$, the proper motion contribution to the observed $\ddot{P}$ is given by $\ddot{P}_\mu \simeq -2.70 \times 10^{-33}\mathrm{s^{-1}}$. In approximately three years of timing data, the $\ddot{P}$ term arising from radial velocity will contribute a $\sim$ 100 ns (peak-to-peak) trend in the times of arrival. However, most of this trend will be absorbed in the linear and quadratic phase terms of the timing model (P and $\dot{P}$). Over ten years, the peak-to-peak difference will be over 2 μs, but the unabsorbed signature will be approximately 100 ns. Assuming negligible intrinsic $\ddot{P}$, an eventual experimental determination of $\ddot{P}$ might enable an estimate of the radial velocity of the PSR J0437−4715 system. Such a measurement would provide additional dynamical information that may prove relevant to the modeling of the PSR J0437−4715 bow-shock nebula (Mann, Romani & Fruchter 1999), for instance.

Equation 3.26 may also be applied to the produce the following vector equation:

$$\dot{\boldsymbol{\mu}} = \frac{d}{dt}(\mu\boldsymbol{\theta}) = \dot{\mu}\boldsymbol{\theta} + \mu\dot{\boldsymbol{\theta}} = -2\frac{v_r}{r}\boldsymbol{\mu} - \mu^2\boldsymbol{K_0}. \tag{3.29}$$

Here, $\boldsymbol{\theta} = \boldsymbol{\mu}/\mu$ is a unit vector in the $\boldsymbol{I_0}$–$\boldsymbol{J_0}$ plane that points in the direction of proper motion. To first order, the timing signature due to proper motion derivative is given by

$$\Delta_{\dot{\boldsymbol{\mu}}} = \frac{1}{2c}\dot{\boldsymbol{\mu}} \cdot \boldsymbol{r}(t - t_0)^2. \tag{3.30}$$

Assuming the same radial velocity of $100\,\mathrm{km\,s^{-1}}$, it can be shown that this term will have a peak-to-peak amplitude of $\sim$100 ns in approximately 30 years, yielding another independent estimate of the system's radial velocity or perhaps enabling the separation of intrinsic and kinematic $\ddot{P}$ contributions. Again, the current likelihood of such a detection seems negligible. However, it may become necessary to include the $\Delta_{\dot{\boldsymbol{\mu}}}$ term in a future timing model in order to decrease the residual timing noise.

Further discussion regarding the results of our analysis is presented in the following chapter and in the conclusion.

Chapter 4

A Test of General Relativity

This chapter was previously published as W. van Straten, M. Bailes, M.C. Britton, S.R. Kulkarni, S.B. Anderson, R.N. Manchester & J. Sarkissian, 2001, "A test of general relativity from the three-dimensional orbital geometry of a binary pulsar," *Nature* **412**, 158–160. Minor alterations have been made in order to maintain consistency of style.

Binary pulsars provide an excellent system for testing general relativity because of their intrinsic rotational stability and the precision with which radio observations can be used to determine their orbital dynamics. Measurements of the rate of orbital decay of two pulsars have been shown to be consistent with the emission of gravitational waves as predicted by general relativity (Taylor & Weisberg 1982; Stairs et al. 1998), providing the most convincing evidence for the self-consistency of the theory to date. However, independent verification of the orbital geometry in these systems was not possible. Such verification may be obtained by determining the orientation of a binary pulsar system using only classical geometric constraints, permitting an independent prediction of general relativistic effects. Here we report high-precision timing of the nearby binary millisecond pulsar PSR J0437−4715, which establish the three-dimensional structure of its orbit. We see the expected retardation of the pulse signal arising from the curvature of space-time in the vicinity of the companion object (the 'Shapiro delay'), and we determine the mass of the pulsar and its white dwarf companion. Such mass determinations contribute to our understanding of the origin and evolution of neutron stars (Thorsett & Chakrabarty 1999).

Discovered in the Parkes 70-cm survey (Johnston et al. 1993), PSR J0437−4715 remains the closest and brightest millisecond pulsar known. It is bound to a low-mass helium white dwarf companion (Bell, Bailes & Bessell 1993; Danziger, Baade & Della Valle 1993) in a nearly circular orbit. Owing to its proximity, relative motion between the binary system and the Earth significantly alters the line of sight direction to the pulsar and, consequently, the orientation of the basis vectors used in the timing model (see Figure 4.1). Although the physical orientation of the orbit in space remains constant, its parameters are measured with respect to this time-dependent basis and therefore also vary with time. Variations of the inclination angle, i, change the projection of the semi-major axis along the line of sight, $x \equiv a_{\rm p} \sin i/c$, where $a_{\rm p}$ is the semi-major axis of the pulsar orbit.

The heliocentric motion of the Earth induces a periodic variation of x known as the annual-orbital parallax (Kopeikin 1995),

$$x^{\rm obs}(t) = x^{\rm int}[1 + \frac{\cot i}{d}\ \mathbf{r}_{\oplus}(t) \cdot \mathbf{\Omega'}]. \tag{4.1}$$

The superscripts 'obs' and 'int' refer to the observed and intrinsic values, respectively, $\mathbf{r}_{\oplus}(t)$ is the position vector of the Earth with respect to the barycentre of the Solar System as a function of time, d is the distance to the pulsar, and $\mathbf{\Omega'} = \sin\Omega \mathbf{I_0} - \cos\Omega \mathbf{J_0}$ (see Figure 4.1). Similarly, the proper motion of the binary system induces secular evolution of the projected semi-major axis (Kopeikin 1996; Sandhu et al. 1997), such that:

$$\dot{x}^{\rm obs} = \dot{x}^{\rm int} - x \cot i\ \boldsymbol{\mu} \cdot \mathbf{\Omega'}; \tag{4.2}$$

where $\boldsymbol{\mu} = \mu_\alpha \mathbf{I_0} + \mu_\delta \mathbf{J_0}$ is the proper motion vector with components in right ascension, μ_α, and declination, μ_δ. An apparent transverse quadratic Doppler effect (known as the Shklovskii effect) also arises from the system's proper motion and contributes to the observed orbital period derivative (Damour & Taylor 1991):

$$\dot{P}_{\rm b}^{\rm obs} = \dot{P}_{\rm b}^{\rm int} + \beta P_{\rm b}; \tag{4.3}$$

where $\beta = \mu^2 d/c$, and $\mu = |\boldsymbol{\mu}|$.

Observations of PSR J0437−4715 were conducted from 11 July 1997 to 13 December 2000, using the Parkes 64 m radio telescope. Over 50 Terabytes of baseband data have been recorded with the S2 Recorder (Cannon et al. 1997) and the Caltech Parkes Swinburne Recorder (CPSR) (van Straten, Britton & Bailes 2000), followed by off-line reduction at Swinburne's supercomputing facilities. Average pulse profiles from hour-long integrations were fitted to a high signal-to-noise template (Taylor 1992), producing a total of 617 pulse arrival time measurements with estimated errors on the order of 100 ns.

Previously considered negligible, the annual-orbital parallax has been largely ignored in experimental arrival time analyses to date. However, our initial estimates of its peak-to-peak amplitude for PSR J0437−4715 ($\sim$ 400 ns) demonstrated that it would be clearly detectable. As can be seen in Equation 4.1, $x^{\rm obs}$ varies with a period of one year and phase determined by $\mathbf{\Omega'}$. Its inclusion in our timing model therefore provides a geometric constraint on Ω. We also note that the value of $\dot{x}^{\rm obs} = (7.88 \pm 0.01) \times 10^{-14}$ observed in our preliminary studies is many orders of magnitude larger than the intrinsic $\dot{x}$ expected as a result of the emission of gravitational waves, $\dot{x}^{\rm GR} = -1.6 \times 10^{-21}$. Neglecting $\dot{x}^{\rm int}$, the relationship between i and Ω defined by Equation 4.2 is parameterized by the well determined physical parameters x, $\dot{x}$ and $\boldsymbol{\mu}$. Also, because $\boldsymbol{\mu}$ is fortuitously nearly anti-parallel to $\mathbf{\Omega'}$,

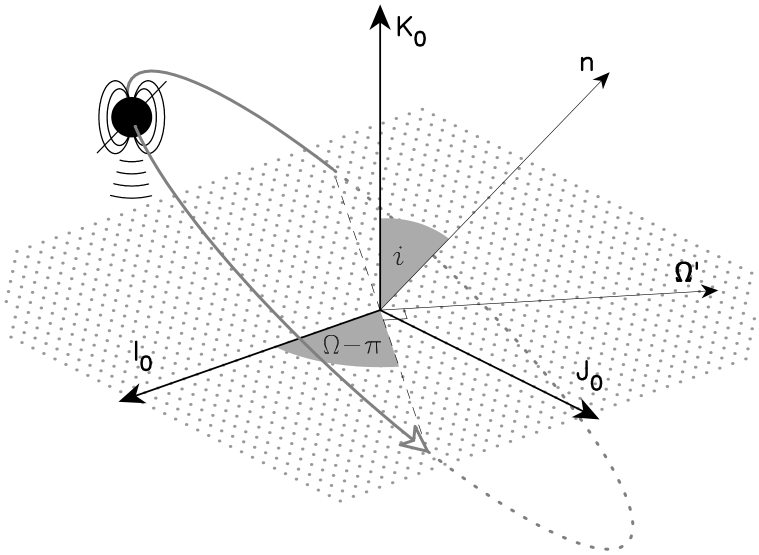

Figure 4.1: The three-dimensional orientation of the pulsar orbit is determined using a classical geometric model. With the centre of mass of the binary system at the origin, the basis vectors, $\mathbf{I_0}$, $\mathbf{J_0}$ and $\mathbf{K_0}$, define east, north, and the line of sight from Earth, respectively. The orientation of the normal vector, $\mathbf{n}$, is defined with respect to this basis by the longitude of the ascending node, Ω, and the inclination angle, i. The plane of the sky, or $\mathbf{I_0}$–$\mathbf{J_0}$ plane, (shown stippled) intersects the orbital plane at the "line of nodes" (dashed line). Below the $\mathbf{I_0}$–$\mathbf{J_0}$ plane, the orbital path has been drawn with a dotted line. The unit vector, $\mathbf{\Omega'}$, lies in the $\mathbf{I_0}$–$\mathbf{J_0}$ plane and is perpendicular to the line of nodes. The pulsar is shown at superior conjunction, where radio pulses emitted toward Earth experience the greatest time delay due to the gravitating mass of the companion on the opposite side of the centre of mass.

$\delta i/\delta\Omega$ is close to zero, and incorporation of Equation 4.2 in our timing model provides a highly significant constraint on the inclination angle.

The orbital inclination parameterizes the shape of the Shapiro delay, that is, the delay due to the curvature of space-time about the companion. In highly inclined orbits, seen more edge-on from Earth, the companion passes closer to the line of sight between the pulsar and the observatory, and the effect is intensified. As the relative positions of the pulsar and companion change with binary phase, the Shapiro delay also varies and, in systems with small orbital eccentricity, is given by:

$$\Delta_{\rm S} = -2r\ln[1 - s\cos(\phi - \phi_0)]. \tag{4.4}$$

Here, $s \equiv \sin i$ and $r \equiv Gm_c/c^3$ are the shape and range, respectively, ϕ is the orbital phase in radians, and ϕ_0 is the phase of superior conjunction, where the pulsar is on the opposite side of the companion from Earth (as shown in Figure 4.1). For small inclinations, the orbit is seen more face-on from Earth, and $\Delta_{\rm S}$ becomes nearly sinusoidal in form.

In the PSR J0437−4715 system, the Shapiro effect is six orders of magnitude smaller than the classical Roemer delay, the time required for light to travel across the pulsar orbit. In nearly circular orbits, the Roemer delay also varies sinusoidally with binary phase. Consequently, when modeling less inclined binary systems with small eccentricity, the Shapiro delay can be readily absorbed in the Roemer delay by variation of the classical orbital parameters, such as x. For this reason, a previous attempt at measuring the Shapiro effect in the PSR J1713+0747 system (Camilo, Foster & Wolszczan 1994) yielded only weak, one-sided limits on its shape and range.

In contrast, we have significantly constrained the shape independently of general relativity, enabling calculation of the component of Δ_S that remains un-absorbed by the Roemer delay. The theoretical signature is plotted in Figure 4 against post-fit residuals obtained after fitting the arrival time data to a model that omits the Shapiro effect. To our knowledge, this verification of the predicted space-time distortion near the companion is the first such confirmation (outside our Solar System) in which the orbital inclination was determined independently of general relativity.

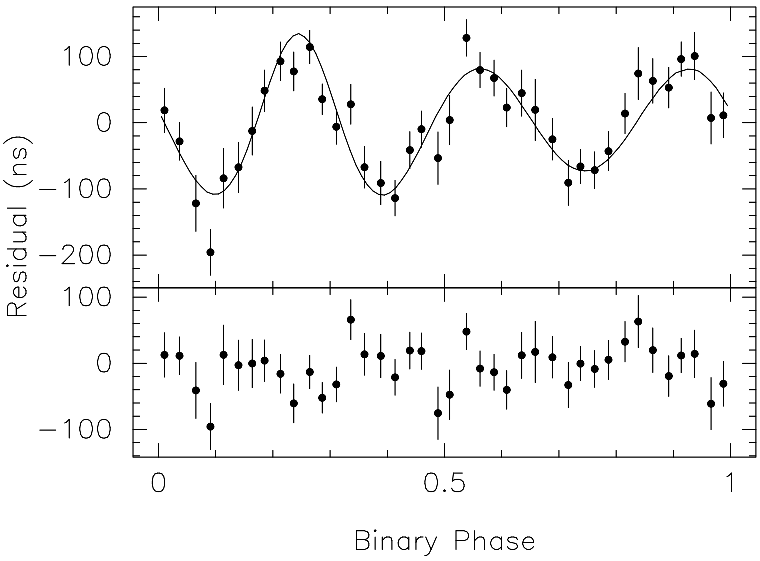

Figure 4.2: Arrival time residuals confirm the predicted space-time distortion induced by the pulsar companion. The unabsorbed remnant of Shapiro delay is much smaller than the theoretical total delay, which for PSR J0437−4715 has a peak-to-peak amplitude of about 3.8 μs. In the top panel, the solid line models the expected delay resulting from a companion with a mass of 0.236 $M_\odot$, at the geometrically-determined orbital inclination. Measured arrival time residuals, averaged in 40 binary phase bins and plotted with their 1σ errors, clearly exhibit the predicted signature. In the bottom panel, the same residuals with the model removed have an RMS residual of only 35 ns and a reduced χ^2 of 1.13.

The range of the Shapiro delay provides an estimate of the companion mass, $m_c = 0.236 \pm 0.017\ M_\odot$, where $M_\odot$ is the mass of the sun. Through the mass function (Thorsett & Chakrabarty 1999), $f(M)$, we then obtain a measurement of the pulsar mass $m_p = 1.58 \pm 0.18\ M_\odot$. Slightly heavier than the proposed average neutron star mass (Thorsett & Chakrabarty 1999), $m_p^{\rm avg} = 1.35 \pm 0.04\ M_\odot$, this value of m_p suggests an evolutionary scenario that includes an extended period of mass and angular momentum transfer. Such accretion is believed to be necessary for a neutron star to attain a spin period of the order of a millisecond (Taam & van den Heuvel 1986). It is also expected that, during accretion, the pulsar spin and orbital angular momentum vectors are aligned. Under this assumption, the measured inclination angle of $i = 42\overset{\circ}{.}75 \pm 0\overset{\circ}{.}09$ does not support the conjecture that pulsar radiation may be preferentially beamed in the equatorial plane (Backer 1998).

Using the general relativistic prediction of the rate of orbital precession, the total system mass, M, can also be calculated from the observed value of $\dot{\omega}$. From M, $f(M)$, and i, we obtain a second consistent estimate of the companion mass, $m_c' = 0.23 \pm 0.14\,\mathrm{M}_\odot$, the precision of which is expected to increase with time as $t^{3/2}$, surpassing that of the r-derived value in approximately 30 years.

The complete list of physical parameters modeled in our analysis is included in Table 4.1. Most notably, the pulsar position, parallax distance, $d_\pi = 139 \pm 3$ pc, and proper motion, $\mu = 140.892 \pm 0.006$ mas yr^{-1}, are known to accuracies unsurpassed in astrometry. Although closer, d_π lies within the 1.5 σ error of an earlier measurement by Sandhu et al. (1997), 178 ± 26 pc. The parallax distance and proper motion estimates can be used to calculate β and the intrinsic spin period derivative, $\dot{P}^{\mathrm{int}} = \dot{P}^{\mathrm{obs}} - \beta P = (1.86 \pm 0.08) \times 10^{-20}$, providing an improved characteristic age of the pulsar, $\tau_{\mathrm{c}} = P/(2\dot{P}^{\mathrm{int}}) = 4.9$ Gyr. Another distance estimate may be calculated using the observed μ and $\dot{P}_{\mathrm{b}}$ by solving Equation 4.3 for d, after noting the relative negligibility of any intrinsic contribution (Bell & Bailes 1996). The precision of the derived value, $d_{\mathrm{B}} = 150 \pm 9$ pc, is anticipated to improve as $t^{5/2}$, providing an independent distance estimate with relative error of about 1% within the next three to four years.

With a post-fit RMS residual of merely 130 ns over 40 months, the accuracy of our analysis has enabled the detection of annual-orbital parallax. This has yielded a three-dimensional description of a pulsar binary system and a new geometric verification of the general relativistic Shapiro delay. Only the Space Interferometry Mission (SIM) is expected to localize celestial objects with precision similar to that obtained for PSR J0437−4715 (including parallax). By the time SIM is launched in 2010, the precision of this pulsar's astrometric and orbital parameters will be vastly improved. Observations of the companion of PSR J0437−4715 using SIM will provide an independent validation and a tie between the SIM frame and the solar-system dynamic reference frame.

We also expect that continued observation and study of this pulsar will ultimately have an important impact in cosmology. Various statistical procedures have been applied to the unmodeled residuals of PSR B1855+09 (McHugh et al. 1996, and references therein) in an effort to place a rigorous upper limit on Ω_g, the fractional energy density per logarithmic frequency interval of the primordial gravitational wave background. As the timing baseline for PSR J0437−4715 increases, our experiment will probe more deeply into the low frequencies of the cosmic gravitational wave spectrum, where, owing to its steep power-law dependence (McHugh et al. 1996), the most stringent restriction on Ω_g can be made.

Table 4.1: PSR J0437−4715 physical parameters

Right ascension, α (J2000)	$04^{\mathrm{h}}37^{\mathrm{m}}15\overset{\mathrm{s}}{.}7865145(7)$
Declination, δ (J2000)	$-47^\circ 15' 08\overset{\prime\prime}{.}461584(8)$
μ_α (mas yr^{-1})	121.438(6)
μ_δ (mas yr^{-1})	-71.438(7)
Annual parallax, π (mas)	7.19(14)
Pulse period, P (ms)	5.757451831072007(8)
Reference epoch (MJD)	51194.0
Period derivative, $\dot{P}$ (10^{-20}) ..	5.72906(5)
Orbital period, P_{b} (days)	5.741046(3)
x (s)	3.36669157(14)
Orbital eccentricity, e	0.000019186(5)
Epoch of periastron, T_0 (MJD)	51194.6239(8)
Longitude of periastron, ω (°) .	1.20(5)
Longitude of ascension, Ω (°) .	238(4)
Orbital inclination, i (°)	42.75(9)
Companion mass, m_c ($\mathrm{M}_\odot$) ...	0.236(17)
$\dot{P}_{\mathrm{b}}$(10^{-12})	3.64(20)
$\dot{\omega}$ (°yr^{-1})	0.016(10)

Best-fit physical parameters and their formal 1σ errors were derived from arrival time data by minimizing an objective function, χ^2, as implemented in TEMPO (http://pulsar.princeton.edu/tempo). Our timing model is based on the relativistic binary model (Damour & Deruelle 1986) and incorporates additional geometric constraints derived by Kopeikin (Kopeikin 1995; Kopeikin 1996). Indicative of the solution's validity, χ^2 was reduced by 30% with the addition of only one new parameter, Ω. To determine the 1σ confidence intervals of Ω and i, we mapped projections of the $\Delta\chi^2 \equiv \chi^2(\Omega, i) - \chi^2_{\mathrm{min}} = 1$ contour, where $\chi^2(\Omega, i)$ is the value of χ^2 minimized by variation of the remaining model parameters, given constant Ω and i. Parenthesized numbers represent uncertainty in the last digits quoted, and epochs are specified using the Modified Julian Day (MJD).

Chapter 5

Instrumental Calibration

The polarimetric calibration techniques proposed and used to date have fallen short of completely correcting the systematic distortions of the mean total intensity pulse profile. Therefore, the arrival time estimates presented in the previous chapters were derived using the invariant profile proposed by Britton (2000). Though the total intensity profile contains more power and has greater S/N than the invariant profile, it was shown to be more susceptible to the instrumental artifacts arising from poor polarimetric response (Britton et al. 2000). However, as apparent in Figure 3.5, the invariant profile has failed to provide arrival time estimates that are entirely free of systematic error. This outstanding problem prompted the development of a new method of polarimetric calibration, presented in Section 5.2. Owing to the level setting technique described in Section 2.4.1, it was also necessary to develop a new method of calibrating the flux of the baseband observations.

5.1 Flux Determination

The original algorithm used for flux calibration was developed for FPTM data. When observing with FPTM, the attenuation levels and sampling thresholds are set only once at the beginning of a calibration (CAL) observation. These levels are maintained throughout both the CAL and the following pulsar (PSR) observations. Therefore, the scale for converting between the temperature in Jy and the flux counts in each bin of the integrated CAL and PSR profiles remains constant. This flux scale is determined in a separate observation of the CAL over a background source of known intensity (for example, Hydra A is used at Parkes).

However, when baseband recording, regular sampling threshold adjustments were made throughout each observation in order to maintain linearity of the system response. This is not to say that the correlator does not suffer from the same quantization errors as a baseband recorder; only, in the latter case, greater attention has been paid toward minimizing signal distortion. The sampling thresholds are altered between and during the CAL and PSR observations and, as they are not recorded, no absolute flux scale applies to both observations.

Instead, it is assumed that the system temperature, $T_{\rm sys}$, remains constant between CAL and PSR observations. The ratio between $T_{\rm sys}$ and the flux of the signal will remain constant while sampling thresholds are chosen to optimize linearity of system response. Therefore, the off-pulse baseline of the average CAL and PSR profiles provides the absolute flux scale by which the observations may be related and by which the pulsar flux may be calibrated.

In future experiments, the sampling thresholds used by the baseband recording system may be documented at record time. However, certain digitizer cards, such as the CPSR-II sampling board installed at Parkes in 2002, use non-linear attenuators for gain control. In such systems, it is non-trivial to relate fluxes that have been measured using different attenuator settings, and it is safer to rely on an external source, such as the system temperature, for flux calibration.

5.2 Polarimetric Response

Previously published as W. van Straten, 2002, "Radio Astronomical Polarimetry and Phase-Coherent Matrix Convolution," *Astrophysical Journal*, **568**, 436–442, this section contains minor stylistic alterations.

A new phase-coherent technique for the calibration of polarimetric data is presented. Similar to the one-dimensional form of convolution, data are multiplied by the response function in the frequency domain. Therefore, the system response may be corrected with arbitrarily high spectral resolution, effectively treating the problem of bandwidth depolarization, and the original temporal resolution of the data may be retained. The method is therefore particularly useful in the study of radio pulsars, where high time resolution and polarization purity are essential requirements of high-precision timing. The technique is applied to full-polarization baseband recordings of the nearby millisecond pulsar, PSR J0437−4715.

In radio polarimetry, two orthogonal senses of polarization are received and propagated through separate signal paths. Each signal therefore experiences a different series of amplification, attenuation, mixing, and filtering before sampling or detection is performed. Whereas efforts are made to match the components of the observatory equipment, each will realistically have a unique frequency response to the input signal. Even a simple mismatch in signal path length will result in a relative phase difference between the two polarizations that varies linearly with frequency.

In fact, any physically realizable system will transform the radiation in a manner that depends on frequency. Where variations across the smallest bandwidth available may be considered negligible, post-detection calibration and correction techniques may be used to invert the transformation and recover the original polarimetric state. However, the transformation may vary significantly across the band, causing the polarization vector to combine destructively when integrated in frequency. This phenomenon is known as "bandwidth depolarization" of the signal, and results in irreversible decimation of the degree of polarization.

It is therefore desirable to perform polarimetric corrections at sufficiently high spectral resolution, which is available only at the cost of temporal resolution unless phase coherence is maintained. Conventional post-detection correction techniques therefore prove insufficient when high time resolution is also a necessity. For example, certain pulsar experiments require high time resolution in order to resolve key features in the average pulse profile. It has also been shown that insufficient time resolution can also lead to depolarization (Gangadhara et al. 1999). These considerations motivate the development of a method for phase-coherent polarimetric transformation. Further impetus is provided by the growing number of baseband recording systems at observatories around the world, the enhanced flexibility made available through use of off-line data reduction software, and the increasing computational power of affordable facilities.

A method has previously been presented for the phase-coherent correction of interstellar dispersion smearing. Convolution is performed by multiplying the spectrum of baseband data with the inverted frequency response of the interstellar medium (ISM), as modeled by the cold plasma dispersion relation (Hankins & Rickett 1975). The current development extends the concept of convolution to multiplication of the vector spectrum by the inverse of the frequency response matrix. The term "matrix convolution" is used to distinguish this operation from two-dimensional convolution, such as would be performed on an image. Whereas the frequency response matrix may be composed of various factors, such as those arising from the ISM and ionosphere, this chapter will be restricted to considering only the instrumental response.

Following a brief review of matrix convolution and its relationship to the transformation properties of radiation, a technique is proposed by which the instrumental frequency response matrix may be determined and used to calibrate phase-coherent baseband data. As a preliminary illustration, the method is applied to full-polarization observations of the millisecond pulsar, PSR J0437−4715, from two different receiver systems. The results agree well with previously published polarimetry for this pulsar (Navarro et al. 1997).

5.2.1 Matrix Convolution

Consider a linear system with impulse response, $j(t)$. Presented with an input signal, $e(t)$, the output of this system is given by the convolution, $e'(t) = j(t) * e(t)$. In the two-dimensional case, each output signal is given by a linear combination of the input signals,

$$e'_1(t) = j_{11}(t) * e_1(t) + j_{12}(t) * e_2(t), \tag{5.1}$$

$$e'_2(t) = j_{21}(t) * e_1(t) + j_{22}(t) * e_2(t). \tag{5.2}$$

Now let $e_1(t)$ and $e_2(t)$ be the complex-valued analytic signals associated with two real time series, providing the instantaneous amplitudes and phases of two orthogonal senses of polarization. By defining the analytic vector, $\boldsymbol{e}(t)$, with elements $e_1(t)$ and $e_2(t)$, and the 2×2 impulse response matrix, $\mathbf{j}(t)$, with elements $j_{mn}(t)$, we may express the propagation of a transverse electromagnetic wave by the matrix equation,

$$\boldsymbol{e'}(t) = \mathbf{j}(t) * \boldsymbol{e}(t). \tag{5.3}$$

By the convolution theorem, Equation 5.3 is equivalent to

$$\boldsymbol{E'}(\nu) = \mathbf{J}(\nu)\boldsymbol{E}(\nu), \tag{5.4}$$

where $\mathbf{J}(\nu)$ is the frequency response matrix with elements $J_{mn}(\nu)$, and $\boldsymbol{E}(\nu)$ is the vector spectrum. In the case of monochromatic light, or under the assumption that $\mathbf{J}(\nu)$ is constant over all frequencies, matrix convolution reduces to simple matrix multiplication in the time domain, as traditionally represented using the Jones matrix. However, because these conditions are not physically realizable, the Jones matrix finds its most meaningful interpretation in the frequency domain.

The average auto- and cross-power spectra are summarized by the average power spectrum matrix, defined by the vector direct product, $\bar{\mathbf{P}}(\nu) = \langle \boldsymbol{E}(\nu) \otimes \boldsymbol{E}^\dagger(\nu) \rangle$, where $\boldsymbol{E}^\dagger$ is the Hermitian transpose of $\boldsymbol{E}$ and the angular brackets denote time averaging. More explicitly:

$$\bar{\mathbf{P}}(\nu) = \begin{pmatrix} \langle E_1(\nu)E_1^*(\nu)\rangle & \langle E_1(\nu)E_2^*(\nu)\rangle \\ \langle E_2(\nu)E_1^*(\nu)\rangle & \langle E_2(\nu)E_2^*(\nu)\rangle \end{pmatrix}. \tag{5.5}$$

Each component of the average power spectrum matrix, $\bar{P}_{mn}(\nu)$, is the Fourier transform pair of the average correlation function, $\bar{\rho}_{mn}(\tau)$ (Papoulis 1965). Therefore, $\bar{\mathbf{P}}(\nu)$ may be related to the commonly used coherency matrix,

$$\boldsymbol{\rho} = \langle \boldsymbol{E}(t) \otimes \boldsymbol{E}^\dagger(t) \rangle = \bar{\boldsymbol{\rho}}(0) = \frac{1}{2\pi} \int_{\nu_0 - \Delta\nu}^{\nu_0 + \Delta\nu} \bar{\mathbf{P}}(\nu) d\nu, \tag{5.6}$$

where ν_0 is the centre frequency and $2\Delta\nu$ is the bandwidth of the observation. The average power spectrum matrix may therefore be interpreted as the coherency spectral density matrix and, in the limit $\Delta\nu \to 0$, $\boldsymbol{\rho} = \bar{\mathbf{P}}(\nu_0)/2\pi$.

Using Equations 5.4 and 5.5 it is easily shown that a two-dimensional linear system transforms the average power spectrum as

$$\bar{\mathbf{P}}'(\nu) = \mathbf{J}(\nu)\bar{\mathbf{P}}(\nu)\mathbf{J}^\dagger(\nu). \tag{5.7}$$

This matrix equation is a congruence transformation, and forms the basis on which the frequency response of the system will be related to the input (source) and output (measured) coherency spectrum. For brevity in the remainder of this chapter, all symbolic values are assumed to be a function of frequency, ν.

5.2.2 Isomorphic Representations

The subject of radio astronomical polarimetry received its most rigorous and elegant treatment with the two separate developments of Britton (2000) and Hamaker (2000). Whereas Britton illuminates the isomorphism between the transformation properties of radiation and those of the Lorentz group, Hamaker illustrates and utilizes the similarity with the multiplicative quaternion group. The salient features of both formalisms provide a sound foundation for the current development, and merit a brief review.

Any complex 2×2 matrix, $\mathbf{J}$, may be expressed as

$$\mathbf{J} = J_0\mathbf{I} + \boldsymbol{J} \cdot \boldsymbol{\sigma}, \tag{5.8}$$

where J_0 and $\boldsymbol{J} = (J_1, J_2, J_3)$ are complex, $\mathbf{I}$ is the 2×2 identity matrix, and $\boldsymbol{\sigma}$ is a 3-vector whose components are the Pauli spin matrices. The 4-vector, $[J_0, \boldsymbol{J}]$, may be treated using the same algebraic rules as those used for quaternions. In the remainder of this chapter, the equivalent quaternion and 2×2 matrix forms (as related by Equation 5.8) will be interchanged freely.

If $\mathbf{J}$ is Hermitian, then the components of $[J_0, \boldsymbol{J}]$ are real. The average power spectrum and coherency matrices are Hermitian and, when decomposed in this manner, $2[S_0, \boldsymbol{S}]$ may be interpreted as the mean Stokes parameters, where $2S_0$ is the total intensity and $2\boldsymbol{S}$ is the polarization vector. By writing $\bar{\mathbf{P}} = [\bar{S}_0, \bar{\boldsymbol{S}}]$, it is more easily seen that the integration of Equation 5.6 leads to bandwidth depolarization when the orientation of $\bar{\boldsymbol{S}}$ varies with ν.

An arbitrary 2×2 matrix may also be represented by the polar decomposition,

$$\mathbf{J} = J\, \mathbf{B}_{\hat{\boldsymbol{m}}}(\beta)\mathbf{R}_{\hat{\boldsymbol{n}}}(\phi), \tag{5.9}$$

where $J = (\det \mathbf{J})^{1/2}$,

$$\mathbf{B}_{\hat{\boldsymbol{m}}}(\beta) = \exp(\boldsymbol{\sigma}\cdot\hat{\boldsymbol{m}}\beta) = [\cosh\beta, \sinh\beta\, \hat{\boldsymbol{m}}], \tag{5.10}$$

$$\mathbf{R}_{\hat{\boldsymbol{n}}}(\phi) = \exp(i\, \boldsymbol{\sigma}\cdot \hat{\boldsymbol{n}}\phi) = [\cos\phi, i\sin\phi\, \hat{\boldsymbol{n}}], \tag{5.11}$$

and $\hat{\boldsymbol{m}}$ and $\hat{\boldsymbol{n}}$ are real-valued unit 3-vectors. The matrix, $\mathbf{R}_{\hat{\boldsymbol{n}}}(\phi)$, is unitary and, beginning with Equation 5.7, it can be shown to preserve the degree of polarization and rotate $\boldsymbol{S}$ about the axis, $\hat{\boldsymbol{n}}$, by an angle 2ϕ. Similarly, the Hermitian matrix, $\mathbf{B}_{\hat{\boldsymbol{m}}}(\beta)$, can be shown to perform a Lorentz boost on the 4-vector, $[S_0, \boldsymbol{S}]$, along the axis, $\hat{\boldsymbol{m}}$, by a velocity parameter, 2β (Britton 2000).

As both $\mathbf{B}_{\hat{\boldsymbol{m}}}(\beta)$ and $\mathbf{R}_{\hat{\boldsymbol{n}}}(\phi)$ are unimodular, the congruence transformation (Equation 5.7) preserves the determinant up to a multiplicative constant, $|J|^2$, ie. $\det\bar{\mathbf{P}}' = |J|^2 \det\bar{\mathbf{P}}$. Britton notes that $\det\bar{\mathbf{P}} = \bar{S}_0^2 - |\bar{\boldsymbol{S}}|^2 = \bar{S}_{\rm inv}^2$ is simply the Lorentz invariant, which he calls the polarimetric invariant interval. He also proposes that a mean pulsar profile formed using the invariant interval may be used for high-precision pulsar timing. Whereas the boost component of the system response distorts the total intensity profile in a time-dependent manner, the invariant interval remains stable, providing a superior basis for arrival time estimates and a robust alternative to polarimetric calibration. However, the invariant interval is not preserved in the presence of bandwidth depolarization, further motivating the current development.

5.2.3 Determination of the System Response

In principle, any method by which the frequency response matrix may be derived with sufficiently high resolution could be adapted for use with the matrix convolution approach. A number of different parameterizations and techniques have previously been presented for the calibration of single-dish radio astronomical instrumental polarization (Stinebring et al. 1984; Turlo et al. 1985; Xilouris 1991; Britton 2000). The current treatment follows the parameterization chosen by Hamaker (2000), including polar decomposition of the system response followed by application of the congruence transformation. This approach offers a number of significant advantages. For instance, in the derivation of the solution, it is unnecessary to make any small-angle approximations and, when compared to the manipulations of 4×4 Mueller matrices, the equivalent quaternion and 2×2 Jones matrix representations greatly simplify the required algebra. More importantly, Equations 5.7 and 5.9 are specific to no particular basis, permitting the application of the formalism to a variety of feed designs by proper choice of the basis matrices, $\boldsymbol{\sigma}$. Perhaps most importantly, as shown by Hamaker and discussed below, the polar decomposition enables the determination of the boost component of the system response using only an observation of an unpolarized source. This simplification has beneficial impact on experiments where only the total intensity or fractional degree of polarization are of concern.

Consider the reception of unpolarized radiation, which has an input average power spectrum matrix, $\bar{\mathbf{P}}_L = \mathbf{I}\ T_0/2$, where $\mathbf{I}$ is the identity matrix and T_0 is the total intensity. Beginning with Equations 5.7 and 5.9, the output average power spectrum can be trivially shown to be

$$\bar{\mathbf{P}}'_L = \mathbf{B}_{\hat{\boldsymbol{m}}}(\beta)^2\ |J|^2 T_0/2. \tag{5.12}$$

Notice that the phase of J is lost in the detection of the average power spectrum. For this reason, the current technique is insensitive to absolute phase terms arising in the frequency response of the system, and may be used to determine only the relative phase differences between its components. The scalar factors, $|J|^2$ and T_0, are easily determined in a separate flux calibration procedure that will not be considered presently. Therefore, $\mathbf{B}_{\hat{\boldsymbol{m}}}(\beta)$ may be found by taking the positive Hermitian square root of the measured average power spectrum matrix of an unpolarized source (see Section 5.2.6).

This simple result merits closer inspection. The system response may be corrected by inverting Equation 5.4, that is, by calculating $\boldsymbol{E} = \mathbf{J}^{-1}\boldsymbol{E'}$. Notice that, under the polar decomposition chosen in Equation 5.9, the boost transformation is the first to be inverted. That is, regardless of the unknown rotation, the boost solution may be used to completely invert the distortion of total intensity, S_0. This consequence of the polar decomposition has considerable impact in the field of high-precision pulsar timing, where the average total intensity profile is typically used to determine the pulse time of arrival. Polarimetric distortions to the total intensity can significantly alter the shape of this profile and systematically alter arrival time estimates, especially as a function of parallactic angle, or with fluctuations of ionospheric total electron content. With the boost component thus determined, the resulting distortions to total intensity can, in principle, be completely corrected.

It remains to solve for the rotation component of $\mathbf{J}$, which may be determined using observations of calibrators with known polarization. Given the known boost, $\mathbf{B}_{\hat{\boldsymbol{m}}}(\beta)$, input polarization state, $\bar{\mathbf{P}}_n$, and measured output state, $\bar{\mathbf{P}}'_n$, Equation 5.7 is solved for the rotation, $\mathbf{R}_{\hat{\boldsymbol{n}}}(\phi)$. Considering the equivalent three-dimensional Euclidian rotation, $\mathbf{R}_{\hat{\boldsymbol{n}}}{}^{(3)}(2\phi)$, of the polarization vector, $\boldsymbol{S}$, it is easily seen that, given a single pair of input, $\boldsymbol{S_1}$, and output, $\boldsymbol{S_1}'$, polarization vectors, the rotations that solve $\boldsymbol{S_1}' = \mathbf{R}_{\hat{\boldsymbol{n}}}{}^{(3)}(2\phi)\boldsymbol{S_1}$, where $|\boldsymbol{S_1}'| = |\boldsymbol{S_1}|$, form an infinite set of rotations with axes confined only to a plane. Therefore, an observation of a second, non-collinear calibrator source is required in order to uniquely determine the system response rotation.

Many receivers are equipped with a linearly polarized noise diode that may be used to inject a calibrator signal into the feed horn. This noise diode may be switched using a wide-band, amplitude-modulated square-wave. The “off” or “low” fraction of the wave consists of only the system plus sky temperature, which shall be assumed to be unpolarized. The “on” or “high” fraction of the wave contains additional linearly polarized radiation, described in quaternion form by

$$\bar{\mathbf{P}}_H = [1, (\cos 2\Psi, \sin 2\Psi, 0)]\; C_0/2, \tag{5.13}$$

where C_0 is the flux and Ψ is the position angle of the calibrator diode. A single linear noise diode provides only one known input calibrator state. Unless another calibrator is available, the technique must be modified to solve for a reduced representation of the system response. For the calibration described in this chapter, $\mathbf{R}_{\hat{\boldsymbol{n}}}(\phi)$ was decomposed into two rotations: $\mathbf{R}_{\hat{\boldsymbol{v}}}(\Delta\Psi)$, allowing imperfect alignment of the noise diode; followed by $\mathbf{R}_{\hat{\boldsymbol{q}}}(\Phi_I)$, allowing a differential path length between the two linear polarizations (see Section 5.2.6). It is important to distinguish $\Delta\Psi$ and Φ_I from the actual parameters of the receiver, as the polar decomposition does not model the order in which the transformations physically occur.

5.2.4 Calibrator Observations

When observing the artificial calibrator, it is important that the noise diode is switched on a time-scale much shorter than the interval over which the digitization thresholds are reset, in order that $\bar{\mathbf{P}}_H$ may be differentiated from the baseline, $\bar{\mathbf{P}}_L$. However, the calibrator period must also be long enough to provide distinct on-pulse and off-pulse time samples in the synthesized filterbank. Given the sampling interval, t_s, of the baseband recorder, the calibrator period, T_C, should be at least $T_C \geq n_b t_s N$, where N is the number of channels in the synthetic filterbank and n_b is the desired number of phase bins in the integrated calibrator profile. In order to achieve clear separation of on-pulse and off-pulse states, $n_b = 64$ was chosen. It was also found that a filterbank with $N = 2048$ channels sufficiently resolved the features of the frequency response.

For each hour-long observation of PSR J0437−4715, the pulsed calibrator was recorded for 4.5 minutes, ensuring sufficient signal-to-noise in each channel of the synthetic filterbank. Data were reduced off-line using `psrdisp`, a software package developed to process pulsar baseband data, described in the following section. After forming a synthetic filterbank, the Stokes parameters in each channel were detected and folded at the pulsed calibrator period. High and low state polarimetric passbands were formed from the average on- and off-pulse Stokes parameters of the calibrator profile in each channel. These passbands were median filtered to remove spurious radio-frequency interference, and interpolated to the required frequency resolution, as dictated by the parameters of the coherent dedispersion kernel. From this high frequency-resolution polarimetric representation of the calibrator, the frequency response matrix was computed as described in Section 5.2.6. Figure 5.1 plots representative examples of the determined frequency response parameters at 660 MHz and 1247 MHz. The inverse of the frequency response matrix was used in the convolution kernel when reducing the pulsar observations, as described in the next section.

5.2.5 Pulsar Observations

Baseband data from dual-polarization observations of the nearby, binary millisecond pulsar, PSR J0437−4715, were recorded during 26-28 June 2001 using the 64 m dish at the Parkes Observatory. As a test of phase-coherent calibration in the pathological case (refer to Figure 5.2), the 50 cm receiver was used to record 3.6 hours of data at 660 MHz. A total of 7 hours was also recorded at 1247 MHz, using the centre element of the Multibeam receiver. The radio and intermediate frequency signals were quadrature downconverted, band-limited to 20 MHz, two-bit sampled, and recorded using the Caltech-Parkes-Swinburne Recorder (CPSR) (van Straten, Britton & Bailes 2000). The digitized data were processed off-line at Swinburne University's supercomputing facilities using `psrdisp`, a flexible software package that implements a number of baseband data reduction options.

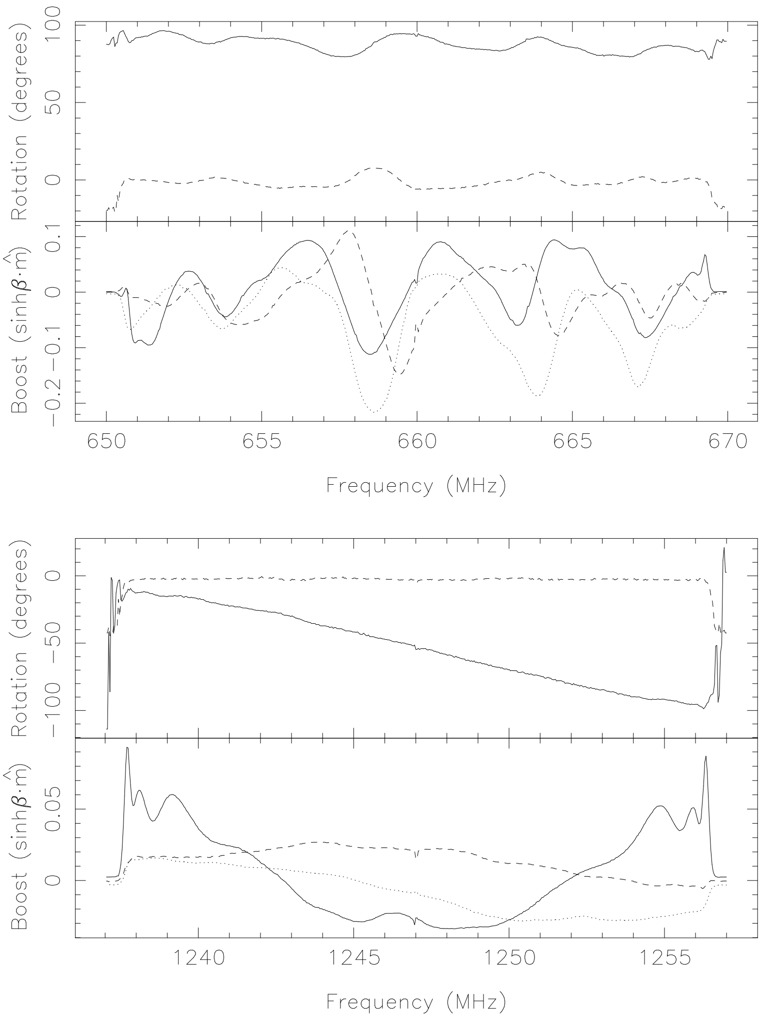

Figure 5.1: Frequency response at 50 cm (top) and 20 cm (bottom). For each band, the upper panel plots the rotation angles, $\Delta\Psi$ (dashed line) and Φ_I (solid line), and the lower panel plots the boost components along $\hat{q}$ (solid line), $\hat{u}$ (dotted line), and $\hat{v}$ (dashed line). A signal path length mismatch between the two polarizations from the Multibeam (20 cm) receiver results in a linear differential phase (Φ_I) gradient across the bandpass.

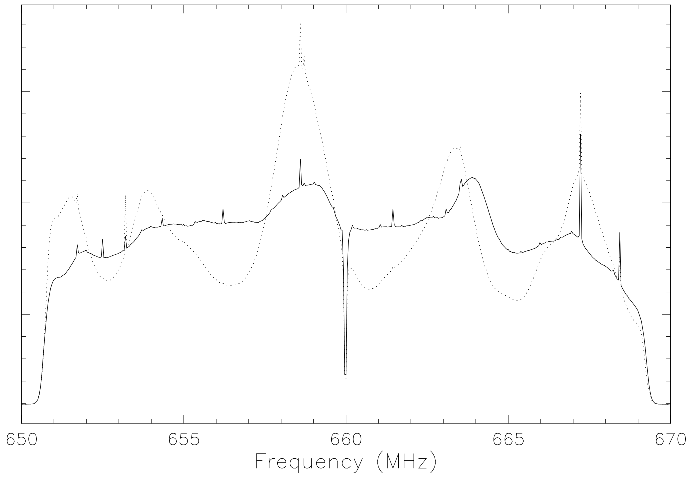

Figure 5.2: Average passbands from the two linear polarizations at 660 MHz, plotted on an uncalibrated linear scale. The gain in E_y (dotted line) varies with frequency by as much as 3 dB, evidencing the faulty condition of the 50 cm receiver.

Four channels of two-bit quantized data were corrected using the dynamic level-setting technique (Jenet & Anderson 1998) and combined to form the analytic vector, $\boldsymbol{e}(t_i)$. This vector was convolved while synthesizing a 16-channel coherent filterbank (Jenet et al. 1997). In each channel, the Stokes 4-vector, $[S_0, \boldsymbol{S}](\nu_k, t_n)$, was detected and integrated as a function of pulse phase, given by t_n modulo the predicted topocentric period. Pulse period and absolute phase were calculated using a polynomial generated by the `tempo` software package.

Each 1 GB segment of baseband data (representing approximately 53.7 seconds) was processed in this manner, producing average pulse profiles with 4096 phase bins, or a resultant time resolution of approximately 1.4 μs. Each archive was later corrected for parallactic angle rotation of the receiver feeds before further integrating in time to produce hour-long average profiles. These were flux calibrated using observations of Hydra A, which was assumed to have a flux density of approximately 85 Jy at 660 MHz and 48 Jy at 1247 MHz. The flux calibrated archives were then integrated in time and frequency, producing the mean pulse profiles presented in Figure 5.3. In these plots, the linearly polarized component, L, is given by $L^2 = Q^2 + U^2$ and the position angle, ψ, where $\tan 2\psi = U/Q$, has been plotted twice, at $\psi \pm \pi/2$. Comparison with the uncalibrated profiles in Figure 5.4 indicates significant restoration of the polarized component at both frequencies. The calibrated average profiles also agree satisfactorily with previously published polarization data for PSR J0437−4715 (Navarro et al. 1997).

Discussion

Prior to its reception, the radiation from a pulsar must propagate through the magnetized plasma of the ISM, resulting in Faraday rotation of the position angle.

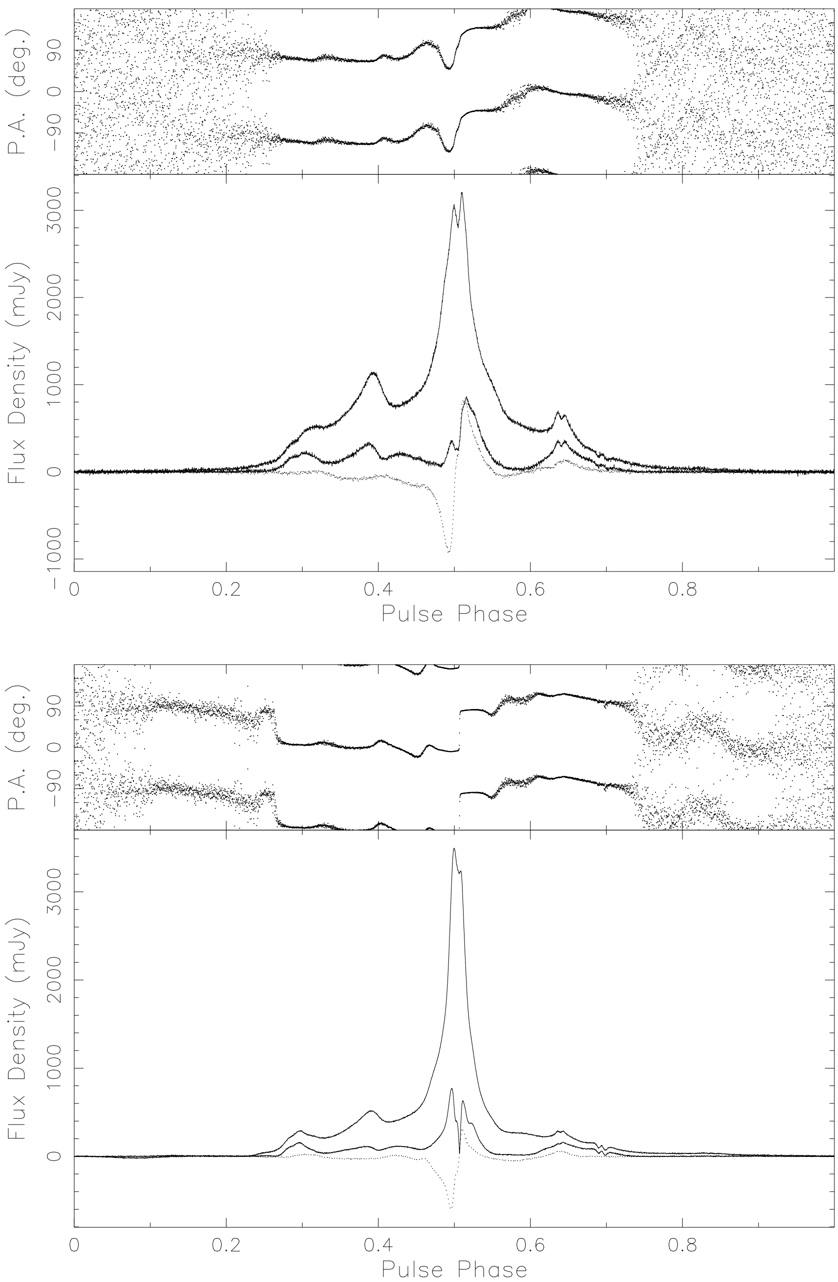

Figure 5.3: Average polarimetric pulse profiles of PSR J0437−4715 at 660 MHz (top) and 1247 MHz (bottom). The bottom panel of each plot displays the total intensity, Stokes I (upper solid line), the linearly polarized component, L (lower solid line), and the circularly polarized component, Stokes V (dotted line). The position angle, ψ, in the upper panel of each plot is shown without respect to any absolute frame of reference.

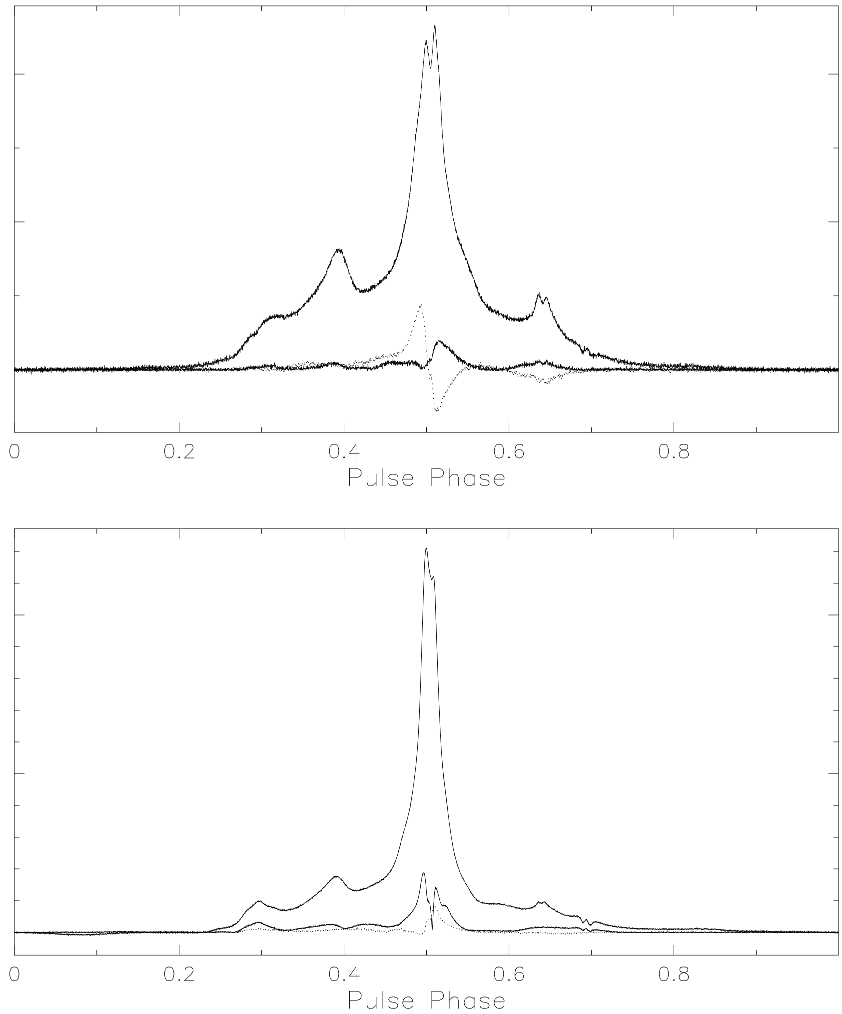

Figure 5.4: Uncalibrated average polarimetric pulse profiles of PSR J0437−4715 at 660 MHz (top) and 1247 MHz (bottom). Severe differential gain variation in the 50 cm bandpass (see Figure 5.2) has decimated the linearly polarized component at 660 MHz (top plot, lower solid line), whereas the differential phase gradient across the 20 cm bandpass (see Figure 5.1) has nearly eliminated the circularly polarized component at 1247 MHz (bottom plot, dotted line).

The change in position angle is given by $\Delta\psi = RM\lambda^2$, where RM is the rotation measure and λ is the wavelength of the radiation. Therefore, one motivation for a pulsar polarimetry experiment is the determination of the RM along the line of sight to the pulsar. Combined with a dispersion measure estimate, the RM can provide information about the galactic magnetic field strength and direction. When the RM is very small, as it is for PSR J0437−4715, $\Delta\psi$ is not detectable across a single 20 MHz bandpass. Therefore, two observations widely separated in frequency are required in order to obtain an estimate. However, as there exists an unknown feed offset between 50 cm and Multibeam receivers that remains uncalibrated in the current treatment, no estimation of rotation measure is presently offered.

For pulsars with known RM, matrix convolution enables phase-coherent Faraday rotation correction by addition of $\Delta\psi$ to $\Delta\Psi$ in Equation 5.14. This approach would further treat the problem of bandwidth depolarization, especially for sources with large rotation measures observed at lower frequencies.

As phase-coherent calibration corrects the undetected voltages, any measurements derived from these data will also be implicitly calibrated. This includes not only the coherency products but also other statistical values such as the higher order moments, modulation index, and polarization covariance. The method may therefore find application in experiments which aim to describe pulse shape fluctuations (Jenet, Anderson & Prince 2001a) or variations of the galactic magnetic field along the line of sight (Melrose & Macquart 1998), for example.

Although matrix convolution may in principle be used to completely correct baseband data, a full solution of the system response is lacking in the current treatment. Perhaps a technique may be developed which combines the use of pulsars (Stinebring et al. 1984; Xilouris 1991) with high-resolution determination of the frequency response matrix. This approach would include tracking a bright, strongly polarized pulsar over a wide range of parallactic angles, followed by fitting a model of the instrumental response to the measured Stokes parameters. As it is non-trivial to model the effects of phenomena that may change over the course of such a calibration, such as fluctuations in ionospheric total electron content, it may prove more feasible to install a second artificial noise diode in the receiver feed horn. Oriented with a position angle offset from the first by approximately 45°, it would provide a more readily available and reliable means of regularly solving for $\mathbf{R}_{\hat{\boldsymbol{n}}}(\phi)$. Alternatively, a single noise diode could be mechanically rotated with respect to the feeds. Consideration of these options may benefit future feed horn design.

The observations of PSR J0437−4715 presented in the previous section serve to illustrate the strength the matrix convolution technique, highlighting its ability to recover data which has been severely corrupted by the observatory instrumentation. Perhaps the most rigorous test of the methodology will be derived from the unsurpassed timing accuracy of PSR J0437−4715 (van Straten et al. 2001). Calibration errors translate into systematic timing errors, and any deficiency in the characterization of the system response would manifest itself in the arrival time residuals of this remarkable pulsar.

5.2.6 Solution of System Response

The instrumental frequency response matrix used in calibrating the data presented in this chapter was parameterized by

$$\mathbf{J} = \mathbf{B}_{\hat{\boldsymbol{m}}}(\beta)\mathbf{R}_{\hat{\boldsymbol{q}}}(\Phi_I)\mathbf{R}_{\hat{\boldsymbol{v}}}(\Delta\Psi). \tag{5.14}$$

The boost component may be solved most easily using the quaternion form of Equation 5.12,

$$[\bar{L}'_0, \bar{\boldsymbol{L}}'] = \exp(2\,\boldsymbol{\sigma}\boldsymbol{\cdot}\,\hat{\boldsymbol{m}}\beta)|J|^2T_0 = [\cosh(2\beta), \sinh(2\beta)\hat{\boldsymbol{m}}]\;|J|^2T_0, \tag{5.15}$$

where $[\bar{L}'_0, \bar{\boldsymbol{L}}']$ are the measured off-pulse Stokes parameters, producing

$$\beta = \frac{1}{2}\tanh^{-1}\left(\frac{|\bar{\boldsymbol{L}}'|}{\bar{L}'_0}\right) \qquad \text{and} \qquad \hat{\boldsymbol{m}} = \frac{\bar{\boldsymbol{L}}'}{|\bar{\boldsymbol{L}}'|}. \tag{5.16}$$

The two rotations, $\mathbf{R}_{\hat{\boldsymbol{q}}}(\Phi_I)$ and $\mathbf{R}_{\hat{\boldsymbol{v}}}(\Delta\Psi)$, may be determined by considering the equivalent three-dimensional Euclidian rotations, $\mathbf{R}_{\hat{\boldsymbol{q}}}{}^{(3)}(2\Phi_I)$ and $\mathbf{R}_{\hat{\boldsymbol{v}}}{}^{(3)}(2\Delta\Psi)$, of the input polarization vector. Given that the noise diodes installed in the receivers at the Parkes radio-telescope have a position angle nearly equal to 45°, the input Stokes parameters are $[1, \bar{\boldsymbol{H}}]C_0$, where $\bar{\boldsymbol{H}} = (0, 1, 0)$ (cf. Equation 5.13). Therefore, Φ_I and $\Delta\Psi$ may be found by solving

$$\bar{\boldsymbol{H}}'' = \mathbf{R}_{\hat{\boldsymbol{q}}}{}^{(3)}(2\Phi_I)\mathbf{R}_{\hat{\boldsymbol{v}}}{}^{(3)}(2\Delta\Psi)\bar{\boldsymbol{H}}, \tag{5.17}$$

where $\bar{\boldsymbol{H}}''$ is the normalized polarization vector after the observed Stokes parameters have been corrected for the boost. It is given by

$$[\bar{H}_0, \bar{\boldsymbol{H}}]'' = \mathbf{B}_{\hat{\boldsymbol{m}}}(\beta)^{\dagger}\bar{\mathbf{P}}'_H\mathbf{B}_{\hat{\boldsymbol{m}}}(\beta)/(|J|^2C_0), \tag{5.18}$$

where $\bar{\mathbf{P}}'_H$ are the observed Stokes parameters. From Equation 5.17,

$$\Phi_I = \frac{1}{2}\tan^{-1}\left(\frac{-H''_3}{H''_2}\right) \qquad \text{and} \qquad \Delta\Psi = \frac{1}{2}\tan^{-1}\left(\frac{H''_1}{H''_2/\cos(2\Phi_I)}\right). \tag{5.19}$$

Notice that $|J|^2$, T_0, and C_0 cancel out in each of Equations 5.16 and 5.19, obviating the need to solve for these parameters at this stage. The vector components of the boost quaternion, $(B_1, B_2, B_3) = \sinh\beta\,\hat{\boldsymbol{m}}$, Φ_I and $\Delta\Psi$, are plotted as a function of frequency in Figure 5.1.

5.2.7 Performing Matrix Convolution

It is assumed that the reader has some familiarity with the more common, one-dimensional form of cyclical convolution as it is performed in the frequency domain using the Fast Fourier Transform (FFT) (Press et al. 1992, §13.1). In the two-dimensional vector case, there are simply two unique processes sampled at the same time interval, say $p(t_i)$ and $q(t_i)$. A one-dimensional, N-point, forward FFT is performed separately on each of p and q, forming two spectra, $P(\nu_k)$ and $Q(\nu_k)$, $0 \leq k < N$. Corresponding elements from each of the spectra are treated as the components of a column 2-vector, $\boldsymbol{E}(\nu_k) = (P(\nu_k), Q(\nu_k))$, and multiplied by the inverse of the frequency response matrix, forming $\boldsymbol{E}'(\nu_k) = \mathbf{J}^{-1}(\nu_k)\boldsymbol{E}(\nu_k)$ (cf. Equation 5.4). The components of the result, $P'(\nu_k)$ and $Q'(\nu_k)$, are once again treated as unique spectra, and separately transformed back into the time domain using the one-dimensional backward FFT.

In the case of the pulsar data presented in this chapter, $p(t_i)$ and $q(t_i)$ are the signals from the two linear receptors in the feed, and $\mathbf{J}(\nu_k)$ consists of the instrumental frequency response matrix, as determined in Section 5.2.6, multiplied by the dedispersion kernel, $H(\nu_k)$ (Hankins & Rickett 1975). When synthesizing an M-channel coherent filterbank, $H(\nu_k)$ is divided in frequency into M distinct dedispersion kernels, each tuned to the centre frequency of the resulting filterbank channel.

Chapter 6

Discussion

This chapter will review some of the outstanding problems that remain to be addressed before further improvements can be made to the timing accuracy of the PSR J0437−4715 dataset. Some of these topics will lead quite naturally into a discussion of possible research directions and conjecture regarding the next generation of radio instrumentation and methodology.

6.1 Outstanding Problems

The primary challenges to future advancement are divided into three categories: instrumental errors, physical considerations, and radio frequency interference.

6.1.1 Instrumental Errors

As mentioned in Section 3.1, the arrival time estimates on which the results presented in this thesis are based were derived using the invariant profile proposed by Britton (2000). However, in Section 5.2.2, it is shown that the invariant interval is not preserved when the system response varies significantly across the observing band, as is commonly the case. Bandwidth depolarization may be one of the reasons that use of the invariant profile has failed to completely eliminate systematic errors related to pulse polarization. There may be a solution to this problem. As shown in Section 5.2.3, the boost component of the system response may be completely determined using an observation of an unpolarized source and used to invert the polarimetric distortion to the total intensity, or Stokes I. It therefore seems likely that the matrix convolution technique may find application in the high-precision timing of PSR J0437−4715, stimulating a return to TOA estimates based on the average total intensity profile, with its higher signal-to-noise ratio.

Bandwidth depolarization may not be the main source of invariant profile corruption. During the development and testing of the matrix convolution technique, careful attention was paid to the finer details of the average polarimetric profile. It was found that the profile baseline in recent CPSR observations is contaminated at the $\sim 1\%$ level, as shown in Figure 6.3. The artifact is not readily attributed to any linear behaviour of the system and is believed to be related to the "dip" observed by Jenet et al. (1998). As the invariant profile calculation depends directly upon proper baseline removal, it is suspected that the formation of $\langle S_{\rm inv}(\phi_k)\rangle$ suffers from this artifact, consequently affecting arrival time estimates derived from $\langle S_{\rm inv}(\phi_k)\rangle$. As an extreme example, one day of severely corrupted data, recorded on January 30, 2000, is presented in Figure 6.1. Although the source of the error remains unexplained, it should be noted that these data were recorded before the repair of the faulty FFD and during a period of system testing. The affected data are readily apparent in the arrival time residuals centred at MJD 51573.5 in Figure 6.2.

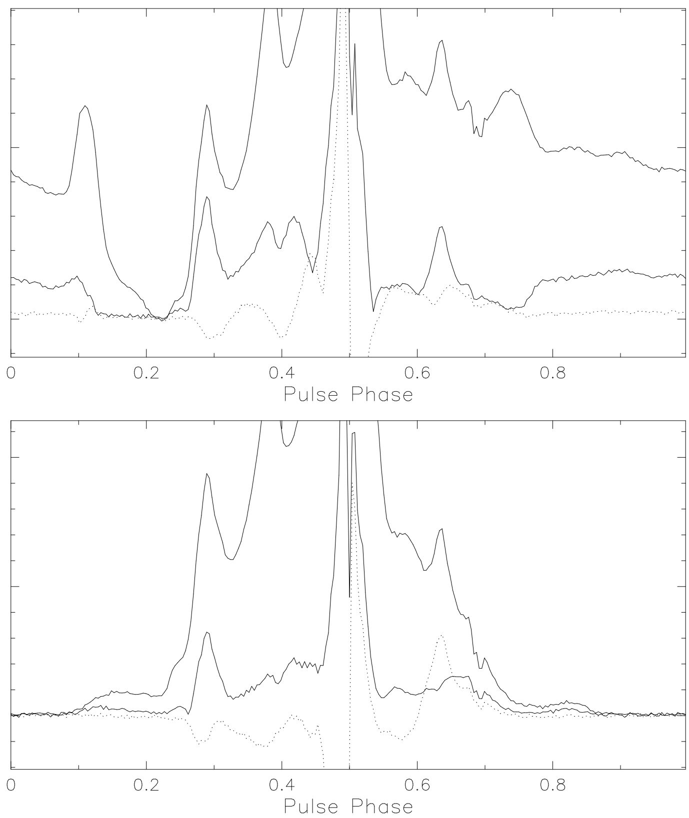

Figure 6.1: Extremely non-linear pulse profile corruption. Each panel displays a magnified view of the profile near the baseline, plotting the total intensity, Stokes I (upper solid line), the linearly polarized component, L (lower solid line), and the circularly polarized component, Stokes V (dotted line). In the upper panel, the average profile observed on January 30, 2000 is severely corrupted by an unexplained instrumental artifact. In the lower panel, data recorded one day later more accurately reflect the average profile shape.

The pulse profile is not often as significantly distorted as that shown in the upper panel of Figure 6.1. However, there typically remains an approximately 1% distortion that is most evident in the profile baseline, as shown in Figure 6.3. The extent to which the invariant profile and the majority of the arrival time estimates

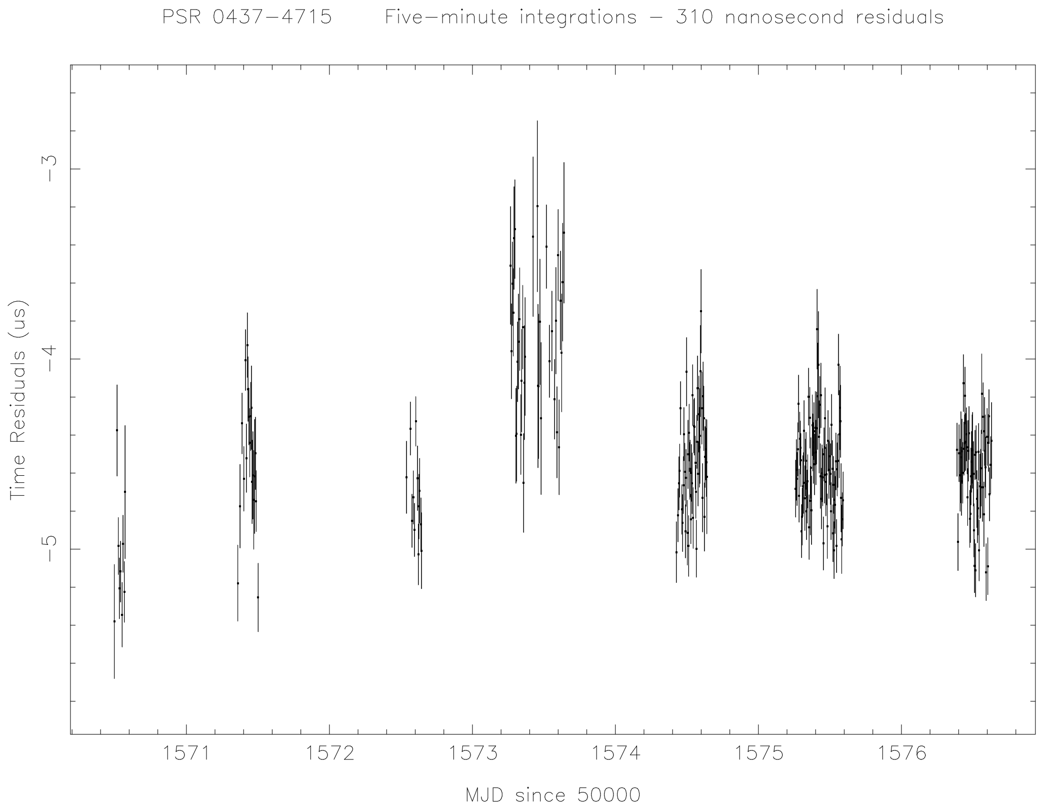

Figure 6.2: Severely corrupted data stand out in arrival time residuals. Each arrival time estimate was derived from an uncalibrated, five-minute integration of the total intensity. Data recorded on January 30, 2000 (MJD 51573.5) are severely corrupted by an unexplained instrumental artifact (see Figure 6.1).

presented in this work are affected is not fully understood, and investigation of the process(es) and/or instrumental component(s) responsible for this non-linearity is of critical importance.

In addition to the investigation of these non-linear effects, the continued use of dual-sideband down-conversion systems may also require further consideration. As the ideal Hilbert transform is not physically realizable, both amplitude and phase alignment errors in practical quadrature filters result in distortions of the analytic signal. In practice, it is difficult to align analog circuits with an accuracy much better than 1% (Hahn 1996), and imperfect image rejection between the in-phase and quadrature components may currently corrupt our CPSR data at an undetermined level.

6.1.2 Physical Considerations

Regardless of the precision with which the observing system may be understood and calibrated, this precision timing experiment may eventually be limited both by the intrinsic evolution of the pulsar and by propagation effects in the ISM.

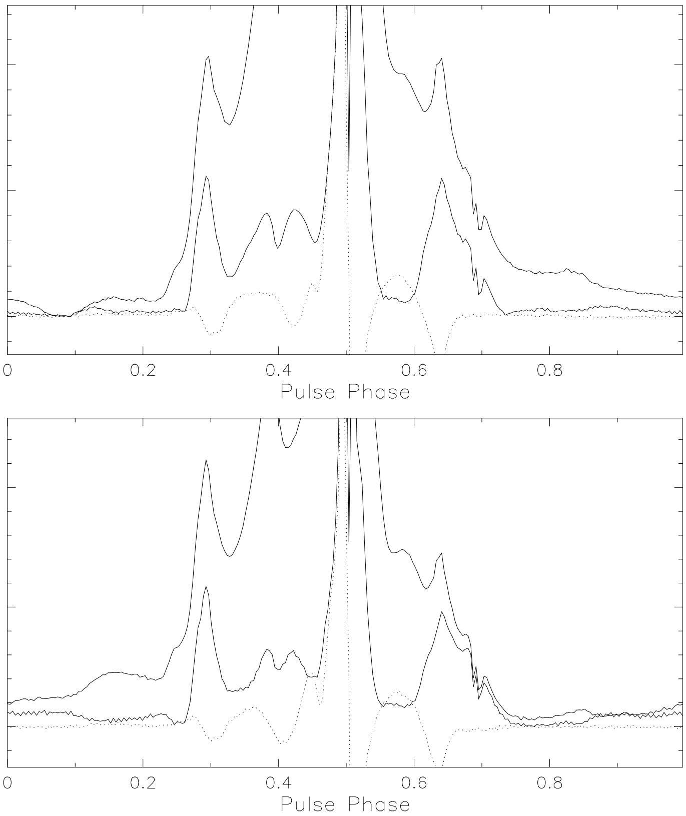

Figure 6.3: Pulse profile corruption in two 20 cm observations. As in Figure 6.1, each panel displays a magnified view of the pulse profile near the baseline, plotting the total intensity, Stokes I (upper solid line), the linearly polarized component, L (lower solid line), and the circularly polarized component, Stokes V (dotted line). The upper and lower panels display the average pulse profile as observed using the Multibeam receiver with a centre frequency of 1247 MHz, and 1510 MHz, respectively. The frequency dependence of the pulse profile distortion may provide clues to its origin.

Precision pulsar timing is founded on the premise that the shape of the integrated pulse profile, when averaged over a sufficiently large number of pulses, does not vary with time (Helfand, Manchester & Taylor 1975; Rankin & Rathnasree 1995). Kramer et al. (1999) question this assumption, and present evidence for smooth variations (on timescales of a few hours) in the average pulse profiles of a number of millisecond pulsars. However, it should be noted that their observations were made with the Effelsberg 100 m radio telescope. As with any altitude-azimuth mounted primary reflector, the orientation of the Effelsberg receiver feed rotates with respect to the Galactic reference frame as the Earth turns beneath the sky. This variation of parallactic angle has been shown to lead to systematic distortions of the integrated pulse profile (see Figure 3.4), an effect that is not corrected by simply calibrating the differential gain and phase of the instrument, as done by Kramer et al. (1999). Therefore, their findings are most likely based on an instrumental artifact.

The average pulse profile may also vary as a result of the precession of the neutron star, which alters the latitude of the line of sight through its magnetic field. Evidence has recently been presented for the free precession of pulsars (Stairs, Lyne & Shemar 2000; Shabanova, Lyne & Urama 2001), which has been interpreted as a result of the misalignment between the spin axis and the neutron star axis of symmetry (Link & Epstein 2001). However, this phenomenon has been observed only in young pulsars, and there is currently no reason to believe that PSR J0437−4715 is freely precessing on any measurable timescale that would contribute to the residual RMS of this timing dataset. Geodetic precession of the spin axis may also arise due to general-relativistic spin-orbit coupling, an effect that has been well-studied in the PSR B1913+16 system (Weisberg, Romani & Taylor 1989; Kramer 1998; Weisberg & Taylor 2002). The rate of precession is given by (Barker & O'Connell 1975, Equation 4)

$$\Omega_p = \frac{3}{2} T_\odot^{5/3} n^{5/3} (1-e^2)^{-1} \, (m_c + m/3) \, M^{-1/3}, \tag{6.1}$$

where the reduced mass, $m = m_p m_c / M$, and all other orbital parameters are defined in Section 3.3. For PSR J0437−4715, $\Omega_p \sim 10^{-3}\,\mathrm{deg\,yr^{-1}}$, and the contribution of precession to mean pulse profile shape variation is considered to be negligible.

Nevertheless, pulsars are known to exhibit a number of pulse shape variation phenomena (e.g. nulling, mode-changing, and drifting sub-pulses) and a detailed study of the long-term stability of PSR J0437−4715's average pulse profile would prove useful in future work.

Pulsars have also been shown to deviate from the smooth, deterministic spin-down behaviour expected due to the loss of rotational energy. For instance, the pulsar glitch phenomenon, a sharp increase in spin frequency followed by a slow, exponential decay (or relaxation) back to the regular spin-down, has been observed in a number of pulsars (see Lyne, Shemar & Smith (2000) for a recent, comprehensive review). Arrival time data may also be affected by pulsar timing noise (Cordes & Helfand 1980; Cordes & Downs 1985), an undetermined stochastic process intrinsic to the pulsar that manifests itself as random fluctuations of the spin-down parameters. Following Arzoumanian et al. (1994), we calculate an upper limit to the timing noise in our dataset using the stability parameter,

$$\Delta(t) < \log\left(\frac{2\sigma_{\ddot\nu} t^3}{6\nu}\right) \tag{6.2}$$

where $\nu = 1/P \sim 173.6\,\mathrm{s^{-1}}$ is the rotational frequency, and $\sigma_{\ddot\nu} \sim 4.8\times10^{-28}\,s^{-3}$ is the formal uncertainty in the second frequency derivative, as determined from the data in Table 3.1. Substituting these values and $t = 10^8\,\mathrm{s}$ into Equation 6.2 yields $\Delta_8 < -6$, less than that of all 139 pulsars presented in Figure 1 of Arzoumanian et al. (1994). Another indication of the low level of timing noise in our dataset is presented in Figure 6.4.

Systematic timing errors might also arise from variations of the dispersion measure along the line of sight to the pulsar (Foster & Cordes 1990). Referring to Figure 4a of Backer et al. (1993), an upper limit to the DM gradient for PSR J0437−4715 is $\sim 10^{-3}\,\mathrm{pc\,cm^{-3}\,yr^{-1}}$. Using arrival time data from observations made at only a single frequency, most of the effect of a slowly varying DM would be absorbed in the polynomial description of pulse phase (see Equation 3.4). However, Figure 4b of Backer et al. (1993) predicts that the RMS DM may be as high as $\sim 2\times10^{-4}\,\mathrm{pc\,cm^{-3}}$, corresponding to an RMS arrival time residual of $\sim$400 ns at 1420 MHz. Therefore, DM variations may currently contribute to perturbations of arrival time estimates in our dataset, and regular monitoring of DM may be beneficial to the long-term timing of this pulsar. The new dual-band, 10/50 cm receiver, soon to be commissioned at Parkes, may prove quite useful in this regard.

The observing frequency used for the majority of the data presented in this thesis (1413 MHz) was chosen largely based on practical considerations. The almost permanent availability of the Parkes Multibeam receiver made it the obvious choice for frequent observations. Also, by keeping the Hi emission line within the chosen bandpass, a quick confirmation of correct down-conversion wiring and system configuration could be made during the recording. However, a more optimal observing frequency may improve the quality of future data. For instance, the flux density of most pulsars varies with frequency according to a simple power law, $S \propto \nu^{\alpha}$, where the average value of the spectral index, α, is $\langle\alpha\rangle = 1.8 \pm 0.2$ (Maron et al. 2000) and the spectral index of PSR J0437−4715 is about -1.5 (Johnston et al. 1993).

Although greater flux density motivates the observation of pulsars at lower frequencies, a number of other factors must be considered. For instance, the intrinsic width of the pulse profile is greater at lower frequencies (Rankin 1983b, see also Figure 5.3), background noise due to non-thermal Galactic radio emission is higher, and propagation effects (such as RM and DM variations in the ionosphere) become increasingly important. Also, the refractive properties of inhomogeneities in the ISM result in multipath propagation of the pulsar signal and irreversible scatter broadening of the pulse profile. Under the assumption of a power-law (Kolmogorov) turbulence spectra, the timescale of broadening is expected to vary with frequency as $\nu^{-4.4}$ (Lee & Jokipii 1975). The optimal choice of observing frequency should be carefully considered for future precision timing work.

6.1.3 Radio Frequency Interference

It is undeniable that the popularity of the internet and the accelerating growth of related industries drive the development of the computing technologies utilized for the reduction of large datasets in modern research projects. For instance, advances in the computational power of desktop workstations are currently revolutionizing the manner in which baseband data are handled. The recording speed and capacity of magnetic tape storage media are not growing as quickly as that of the internal hard-drive or the computational power of the commercially-available central processing unit (CPU). In order to circumvent cumbersome volumes of digital tapes and their transport, new baseband systems currently under development or construction are bringing the workstation cluster to the telescope. Elimination of the magnetic tape bottle-neck allows baseband processing systems to more closely follow the enhancements of CPU and data communication technologies, enabling the recording and reduction of larger bandwidths as well as the implementation of increasingly complicated algorithms.

Ironically, this same expansion is cause for growing concern in the radio astronomy community. The demand for commercial spectrum allocation encroaches on that of the scientific and amateur communities, and the number of sources of radio frequency interference (RFI) continues to rise. RFI can be characterized as either narrow-band (such as the transmission from a terrestrial radio station) or broad-band (such as the footprint of a telemetry satellite). A number of convenient algorithms, such as the median filter, exist for the excision of narrow-band interference and may be trivially added to the suite of data reduction routines in the near future. However, the removal of broad-band interference is a much more challenging and computationally intensive task, as demonstrated by the work of Bell et al. (2001). Even after fiber-optic networks are firmly established as the high-bandwidth communication medium of choice, personal computers and other high-speed electronics will continue to shine in the spectrum of interest to radio astronomers. Therefore, research in this area will prove increasingly important as technology advances.

6.2 Possible Future Directions

Technological advancements not only necessitate better calibration and RFI excision techniques, but also stimulate new science. For instance, a number of novel statistical methods applicable to baseband data have been developed and recently presented by Jenet, Anderson & Prince (2001a, 2001b). Their ensemble averaging techniques enable the study of pulsars previously too weak for single-pulse detection, and have opened a new window into the characterization of pulsar emission. Using observations of PSR J0437−4715, the closest and brightest millisecond pulsar, it should prove interesting to calculate, at high time resolution, some of the statistical measures used by Jenet, Anderson & Prince as well as other higher order moments, such as the polarization covariance (Melrose & Macquart 1998).

In Section 2.4.4, it is argued that the cross products of the coherency matrix, ρ_{12} and ρ_{21}, are generally much smaller than the total intensity, and therefore are not significantly distorted by the scattered power that afflicts ρ_{11} and ρ_{22}. This argument is qualitatively based on the studies of quantization artifacts in the total intensity (Cooper 1970; Jenet & Anderson 1998). However, no quantitative study of the effects of digitization on the full polarimetric representation of electromagnetic radiation has been published to date. Such a study might prove relevant to the precision polarimetry of pulsars and therefore also to high-precision timing.

It seems probable that the mathematical bridges built by Britton (2000) and Hamaker (2000) will promote the development of new, sophisticated formal descriptions of radio polarimetry and advanced calibration techniques. For instance, the Hamaker formalism may find application in the polarimetric description of an array of Luneberg lenses, a design currently under consideration as an implementation of the Square Kilometer Array (SKA). The SKA will provide approximately 300 times greater collecting area than that of Parkes, greatly improving the S/N of pulsar observations and, consequently, the accuracy of arrival time estimates. Accurate polarimetric characterization of the SKA will be required in order to reap the benefits of increased sensitivity in pulsar timing experiments.

As the capacity for recording and transmitting large amounts of data improves with time, it may not benefit every experimental design to observe using greater bandwidths. For instance, every observing system is bound by the ideal operating range of the receiver feed horn. The RFI environment at the observatory might also prohibit expansion into one or more regions of the available radio spectrum. In addition, greater dynamic range may also be required in order to sample the signal from brighter pulsars such as PSR J0437−4715 (see Appendix A). Under these circumstances, it may prove more beneficial to increase the number of bits per sample used during analog to digital conversion. The decrease in non-linear digitization distortions to the average pulse profile would translate into a lower systematic contribution to the arrival time residuals.

The astrometric parameters presented in Table 3.1 are measured in the celestial reference frame defined by the JPL DE200 planetary ephemeris, which is oriented with respect to the Earth's annual orbit. In contrast, astrometric measurements made by Very Long Baseline Interferometry (VLBI) are determined in the International Earth Rotation Service (IERS) reference frame based on the Earth's diurnal spin. By observation of the most distant radio sources, mostly quasars, the IERS frame is defined with respect to the quasi-inertial extragalactic reference frame. Although both reference frames provide a high degree of self-consistency, the transformation between the two frames is known much less accurately. Precise knowledge of the frame tie would aid in the comparison of astrometric estimates from independent experiments and in the navigation of interplanetary craft.

Pulsars provide a natural radio source with which to constrain the tie between Earth-orbit and Earth-rotation oriented reference frames. Both timing and VLBI observations of PSR B1937+21 have been utilized to provide a preliminary comparison with the Folkner et al. (1994) frame tie (Dewey et al. 1996; Bartel et al. 1996). However, the complete three-dimensional rotation between the frames cannot be determined using the position and proper motion estimates of a single source. PSR J0437−4715 is well-separated from PSR B1937+21 on the sky, and it is expected that the unprecedented accuracy of the astrometric parameters presented in this thesis will contribute toward a full, precision determination of the frame tie between the extragalactic and planetary reference systems.

It has also been suggested that, by providing superior long-term frequency stability, an array of millisecond pulsars might possibly be used to complement the atomic standard of terrestrial time. Clock stability may be characterized using a number of analytical techniques. As the model-fitting procedure of pulsar timing removes any quadratic form from the arrival time data, the stability measure most applicable to pulsars is based on spectral estimates derived by fitting cubic polynomials to sequences of clock differences (timing residuals, in this case). Matsakis et al. (1997) define an appropriate dimensionless fractional instability, $\sigma_z(\tau)$, which may be used to compare pulsars with each other and atomic timescales.

As a preliminary estimate of the quality of the PSR J0437−4715 timing data, $\sigma_z(t)$ was computed using the post-fit arrival time residuals from the DDK model. The program, `sigmaz`, freely available from the Princeton pulsar group[1], was used to calculate the values of $\sigma_z(t)$, presented in Figure 6.4. Comparison of Figure 6.4 with Figure 9 of Kaspi, Taylor & Ryba (1994) indicates that PSR J0437−4715 exhibits a timing stability approximately five times better than that of PSR B1855+09. If the trend in Figure 6.4 continues into longer timing baselines without exhibiting any red noise, the superior timing stability of PSR J0437−4715 may have significant cosmological implications relating to the hypothetical background of stochastic gravitational waves.

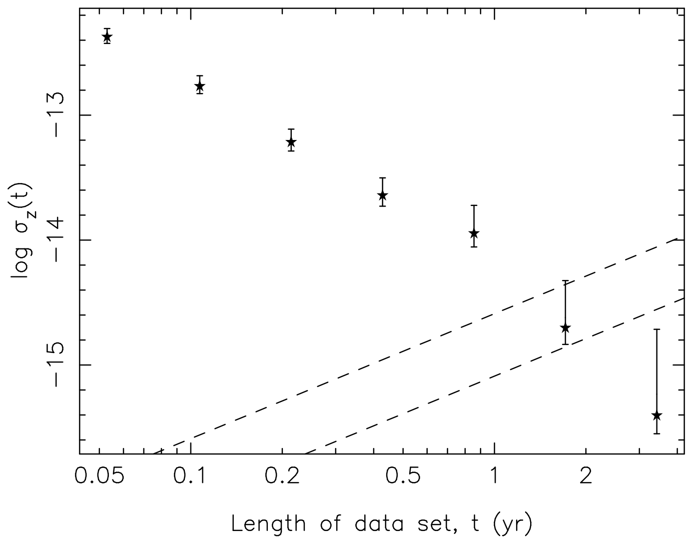

Figure 6.4: Fractional instabilities, $\sigma_z(t)$, of PSR J0437−4715. As in Kaspi, Taylor & Ryba (1994), the upper and lower dotted lines correspond to the theoretical GWB spectrum (Equation 6.3) with normalized energy density $\Omega_g h^2 = 10^{-7}$ and 10^{-8}, respectively.

Similar to the cosmic microwave background, which was accidentally discovered in 1965 by Arno Penzias and Robert Wilson (Penzias & Wilson 1965), a background of stochastic gravitational radiation might possibly echo throughout the universe as

[1]See `http://pulsar.princeton.edu/ftp/pub/tmp/sigmaz`.

a remnant of the big bang. In theory, this gravitational wave background (GWB) would perturb the metric between any given pulsar and the Earth, inducing slight variations in the measured period of the pulsar. The possibility of detecting gravitational waves through the use of pulsar timing was first proposed and developed by Sazhin (1978), who considered the influence of a close binary system along the line of sight between the pulsar and Earth; and also by Detweiler (1979), who treated the Earth and pulsar as free masses with a separation that may be monitored using the pulsar clock. In addition to deriving the additional timing noise contributed by a stochastic background of gravitational radiation, Detweiler also considered the timing signature induced by a more exotic class of supermassive black hole interactions. He also showed that measured values of pulsar timing noise, σ_τ, may be used to place an upper limit on the energy density of the GWB.

Two experimental treatments, published at the same time, were soon to follow. Romani & Taylor (1983) apply Detweiler's GWB result to the timing residuals of PSR B1237+25, whereas Hellings & Downs (1983) introduce the concept of a pulsar timing array by forming the cross correlations of timing residuals from pairs of pulsars. Both papers report similar results, demonstrating that the energy density of gravitational waves with frequency less than 10^{-8} Hz is less than $\sim 10^{-4}$ times the critical density required to close the universe.

Mashhoon (1982) pursues an alternative description of the GWB phenomenon and its effect on pulsar timing that is similar to the twinkling of stars in the Earth's atmosphere. In his treatment, electromagnetic waves are scattered by curvature irregularities in the turbulent spacetime metric of a partially coherent background of stochastic gravitational radiation. Arguing that Detweiler's analysis limits the energy density within only a small interval of the GWB spectrum, Mashhoon claims that his formulation of the resulting timing noise should be sensitive to that part of the GWB spectrum dominated by wavelengths, $\lambda_g > L$, where L is the distance between the Earth and the pulsar. However, this claim is incorrect, as the period of such waves, $P_g = \lambda_g/c$, is far greater than the duration, T, of any current pulsar timing experiment, and the polynomial fit for the pulse period and its derivatives absorbs any signature of gravitational waves with period greater than $T/2$.

Despite this one shortcoming, Mashhoon's phenomenology provided the theoretical basis used by Bertotti, Carr & Rees (1983) to derive a correct expression for the timing noise due to a GWB with a spectral energy density of the form, $\rho_g(\omega) = \rho_0\omega^n$. In this paper it is also demonstrated that, in a binary pulsar system, any discrepancy between the observed and predicted values of the orbital period derivative may be used to provide an upper limit to the energy of the GWB in the interval, $T^{-1} < \lambda_g < L$.

The theoretical intensity and spectral properties of the GWB has since been characterized using models based on the gravitational interactions and oscillations of cosmic strings (Hogan & Rees 1984; Vachaspati & Vilenkin 1985). Based on these models, the GWB contribution to the power spectrum of the timing residuals is predicted to be (Blandford, Narayan & Romani 1984)

$$P_g(f) = \frac{H_0^2}{8\pi^4}\Omega_g f^{-5}, \tag{6.3}$$

where H_0 is the Hubble constant and Ω_g is the fractional energy density per logarithmic frequency interval of the GWB in units of the closure density. Note that Ω_g is expected to be roughly independent of frequency and approximately $\Omega_g \simeq 10^{-7}$ (Vachaspati & Vilenkin 1985).

Following these theoretical predictions, Stinebring et al. (1990) utilized a rigorous method for estimating the spectral content of red noise in the timing residuals of PSR B1937+21 and PSR B1855+09 to place an upper limit of $\Omega_g h^2 \lesssim 4 \times 10^{-7}$ (95% confidence), where $h = H_0/(100\,\mathrm{km\,s^{-1}\,Mpc^{-1}})$. The same method was later employed by Kaspi, Taylor & Ryba (1994) to derive a 95% confidence upper limit of $\Omega_g h^2 \lesssim 6 \times 10^{-8}$. Thorsett & Dewey (1996) reexamine the results of Kaspi, Taylor & Ryba (1994), using an analysis based on the Neyman–Pearson lemma, to place a ten times more stringent limit on $\Omega_g h^2$ and suggest that the corresponding limit on the cosmic string mass per unit length conflicts with a number of string-based theories. However, their result is debated by McHugh et al. (1996), who utilize a Bayesian approach to derive a rigorous limit on $\Omega_g h^2$ that is ten times weaker than the Thorsett & Dewey (1996) result. At a recent meeting of the American Astronomical Society, Lommen & Backer (2001) report $\Omega_g h^2 \lesssim 2 \times 10^{-9}$ based on the findings from millisecond pulsar timing array data.

As evidenced by the various approaches that have been presented thus far, the rigorous limitation of the GWB energy density is a problem that requires careful attention to the statistical and theoretical assumptions made. A detailed investigation of the applicability of the PSR J0437−4715 dataset is yet to be undertaken.

6.3 Conclusion

This thesis presents the first complete determination of the three-dimensional orientation of a pulsar binary system, a new test of general relativity, the most accurate astrometric measurements made to date, and a new, phase-coherent method of polarimetric calibration. Precision timing analysis necessitated the development of an improved timing model that may be applied to other nearby, binary pulsar systems. The neutron star and white dwarf mass determinations will contribute to the population available for use in statistical analyses (Thorsett & Chakrabarty 1999), and the precision astrometric parameters may eventually be used in the full determination of the transformation between the extragalactic and planetary reference frames.

With a post-fit RMS residual of 130 ns over 40 months and fractional instabilities much smaller than those of the best published data, our dataset represents the state of the art in pulsar timing. Its unsurpassed timing stability strongly indicates that continued observation of PSR J0437−4715 may have a significant impact in cosmology. The pulsar is an excellent candidate for inclusion in a pulsar timing array and may eventually contribute to the direct detection of gravitational radiation.

References

Alcock C., Farhi E., Olinto A., 1986, ApJ, 310, 261

Alpar M. A., Cheng A. F., Ruderman M. A., Shaham J., 1982, Nature, 300, 728

Arons J., 1981, ApJ, 248, 1099

Arzoumanian Z., Nice D. J., Taylor J. H., Thorsett S. E., 1994, ApJ, 422, 671

Baade W., Zwicky F., 1934, Proc. Nat. Acad. Sci., 20, 254

Backer D. C., Kulkarni S. R., Heiles C., Davis M. M., Goss W. M., 1982, Nature, 300, 615

Backer D. C., Hama S., Van Hook S., Foster R. S., 1993, ApJ, 404, 636

Backer D. C., Dexter M. R., Zepka A., D. N., Wertheimer D. J., Ray P. S., Foster R. S., 1997, PASP, 109, 61

Backer D. C., 1998, ApJ, 493, 873

Bahcall J. H., 1984, ApJ, 287, 926

Bailes M., Reynolds J. E., Manchester R. N., Norris R. P., Kesteven M. J., 1990, Nature, 343, 240

Bailyn C. D., 1993, ApJ, 411, L83

Barker B. M., O'Connell R. F., 1975, ApJ, 199, L25

Bartel N., Chandler J. F., I. R. M., Shapiro I. I., Pan R., Capallo R. J., 1996, AJ, 112, 1690

Baym G., Pethick C. J., Sutherland P., 1971, ApJ, 170, 299

Becker W., Trümper J., 1993, Nature, 365, 528

Belczynski K., Bulik T., Kluźniak W., 2002, ApJ, 567, L63

Bell J. F., Bailes M., 1996, ApJ, 456, L33

Bell J. F., Bailes M., Bessell M. S., 1993, Nature, 364, 603

Bell J. F., Bailes M., Manchester R. N., Weisberg J. M., Lyne A. G., 1995, ApJ, 440, L81

Bell J. F. et al., 2001, Publications of the Astronomical Society of Australia, 18, 105

Bertotti B., Carr B. J., Rees M. J., 1983, MNRAS, 203, 945

Bhattacharya D., van den Heuvel E. P. J., 1991, Phys. Rep., 203, 1

Blandford R., Teukolsky S. A., 1976, ApJ, 205, 580

Blandford R. D., Narayan R., Romani R. W., 1984, J. Astrophys. Astr., 5, 369

Blasi P., Epstein R. I., Olinto A. V., 2000, ApJ, 533, L123

Bracewell R., 1986, The Fourier Transform and its Applications. McGraw-Hill, New York, Second, Revised edition

Britton M. C., van Straten W., Bailes M., Toscano M., Manchester R. N., 2000, in Kramer M., Wex N., Wielebinski R., eds, Pulsar Astronomy - 2000 and Beyond, IAU Colloquium 177. Astronomical Society of the Pacific, San Francisco, p. 73

Britton M. C., 2000, ApJ, 532, 1240

Camilo F., Foster R. S., Wolszczan A., 1994, ApJ, 437, L39

Cannon W. H. et al., 1997, Vistas Astron., 41, 297

Caraveo P. A., 1993, ApJ, 415, L111

Chandrasekhar S., 1931, ApJ, 74, 81

Chen K., Ruderman M., Zhu T., 1998, ApJ, 493, 397

Cheng A. F., Ruderman M. A., 1980, ApJ, 235, 576

Cooper B. F. C., 1970, Aust. J. Phys., 23, 521

Cordes J. M., Downs G. S., 1985, ApJS, 59, 343

Cordes J. M., Helfand D. J., 1980, ApJ, 239, 640

Damour T., Deruelle N., 1986, Ann. Inst. H. Poincaré (Physique Théorique), 44, 263

Damour T., Taylor J. H., 1991, ApJ, 366, 501

Danner R., Kulkarni S. R., Thorsett S. E., 1994, ApJ, 436, L153

Danziger I. J., Baade D., Della Valle M., 1993, A&A, 276, 382

Daugherty J. K., Harding A. K., 1982, ApJ, 273, 761

de Gouveia Dal Pino E. M., Lazarian A., 2000, ApJ, 536, L31

Deich W. T. S., Kulkarni S. R., 1996, in van Paradijs J., van del Heuvel E. P. J., Kuulkers E., eds, Compact Stars in Binaries: IAU Symposium 165. Kluwer, Dordrecht, p. 279

Detweiler S., 1979, ApJ, 234, 1100

Dewey R. J., Ojeda M. R., Gwinn C. R., Jones D. L., Davis M. M., 1996, AJ, 111, 315

Eddington A. S., 1919, The Observatory, 42, 119

Edelstein J., Foster R. S., Bowyer S., 1995, ApJ, 454, 442+

Edwards R. T., Bailes M., van Straten W., Britton M. C., 2001, MNRAS, 326, 358

Folkner W. M., Charlot P., Finger M. H., Williams J. G., Sovers O. J., Newhall X., Standish E. M., 1994, A&A, 287, 279

Foster R. S., Cordes J. M., 1990, ApJ, 364, 123

Fruchter A. S., 1995. *The bow shock of the nearest millisecond pulsar*, *http://icarus.stsci.edu/~fruchter/nebula/nebula.html*

Gaensler B. M., Arons J., Kaspi V. M., Pivovaroff M. J., Kawai N., Tamura K., 2002, ApJ, 569, 878

Gangadhara R. T., Xilouris K. M., von Hoensbroech A., Kramer M., Jessner A., Wielebinski R., 1999, A&A, 342, 474

Gil J., Krawczyk A., 1997, MNRAS, 285, 561

Gold T., 1968, Nature, 218, 731

Goldreich P., Julian W. H., 1969, ApJ, 157, 869

Gropp W., Lusk E., Doss N., Skjellum A., 1996, Parallel Computing, 22(6), 789

Gwinn C. R., Taylor J. H., Weisberg J. M., Rawley L. A., 1986, AJ, 91, 338

Hahn S. L., 1996, Hilbert Transforms in Signal Processing. Artech House, London

Halpern J. P., Martin C., Marshall H. L., 1996, ApJ, 462, 908

Hamaker J. P., 2000, A&AS, 143, 515

Hankins T. H., Boriakoff V., 1978, Nature, 276, 45

Hankins T. H., Rickett B. J., 1975, in Methods in Computational Physics Volume 14 — Radio Astronomy. Academic Press, New York, p. 55

Hankins T. H., Stinebring D. R., Rawley L. A., 1987, ApJ, 315, 149

Hankins T. H., 1971, ApJ, 169, 487

Hansen B. M. S., Phinney E. S., 1998, MNRAS, 294, 557

Helfand D. J., Manchester R. N., Taylor J. H., 1975, ApJ, 198, 661

Hellings R. W., Downs G. S., 1983, ApJ, 265, L39

Hewish A., Bell S. J., Pilkington J. D. H., Scott P. F., Collins R. A., 1968, Nature, 217, 709

Hibschman J. A., Arons J., 2001, ApJ, 560, 871

Hogan C. J., Rees M. J., 1984, Nature, 311, 109

Hulse R. A., Taylor J. H., 1975, ApJ, 195, L51

Itoh N., 1970, Prog. Theor. Phys., 44, 291

Jenet F. A., Anderson S. B., 1998, PASP, 110, 1467

Jenet F. A., Anderson S. B., Prince T. A., 2001, ApJ, 546, 394

Jenet F. A., Anderson S. B., Prince T. A., 2001, ApJ, 558, 302

Jenet F. A., Cook W. R., Prince T. A., Unwin S. C., 1997, PASP, 109, 707

Jenet F., Anderson S., Kaspi V., Prince T., Unwin S., 1998, ApJ, 498, 365

Johnston S. et al., 1993, Nature, 361, 613

Kaspi V. M., Taylor J. H., Ryba M., 1994, ApJ, 428, 713

Kopeikin S. M., 1995, ApJ, 439, L5

Kopeikin S. M., 1996, ApJ, 467, L93

Kouwenhoven M. L. A., Voûte J. L. L., 2001, A&A, 378, 700

Kramer M., Xilouris K. M., Camilo F., Nice D., Lange C., Backer D. C., Doroshenko O., 1999, ApJ, 520, 324

Kramer M., Wex N., Wielebinski R., eds, Pulsar Astronomy - 2000 and Beyond, IAU Colloquium 177, Astronomical Society of the Pacific, San Francisco, 2000

Kramer M., 1998, ApJ, 509, 856

Kraus J. D., 1986, Radio Astronomy. Cygnus–Quasar Books, Powell, Ohio

Kulkarni S. R., Hester J. J., 1988, Nature, 335, 801

Lattimer J. M., Prakash M., 2001, ApJ, 550, 426

Lee L. C., Jokipii J. R., 1975, ApJ, 201, 532

Link B., Epstein R. I., 2001, ApJ, 556, 392

Lommen A. N., Backer D. C., 2001, ApJ, 562, 297

Lyne A. G., Manchester R. N., 1988, MNRAS, 234, 477

Lyne A. G., Shemar S. L., Smith F. G., 2000, MNRAS, 315, 534

Manchester R. N., Johnston S., 1995, ApJ, 441, L65

Manchester R. N., Peters W. L., 1972, ApJ, 173, 221

Manchester R. N., Taylor J. H., 1977, Pulsars. Freeman, San Francisco

Manchester R. N. et al., 1996, MNRAS, 279, 1235

Manchester R. N., Taylor J. H., Van Y.-Y., 1974, ApJ, 189, L119

Mann E. C., Romani R. W., Fruchter A. S., 1999, BAAS, 195, 41.01

Maron O., Kijak J., Kramer M., Wielebinski R., 2000, in Kramer M., Wex N., Wielebinski R., eds, Pulsar Astronomy - 2000 and Beyond, IAU Colloquium 177. Astronomical Society of the Pacific, San Francisco, p. 227

Mashhoon B., 1982, MNRAS, 199, 659

Matsakis D. N., Taylor J. H., Eubanks T. M., Marshall T., 1997, A&A, 326, 924

McHugh M. P., Zalamansky G., Vernotte F., Lantz E., 1996, Phys. Rev. D, 54, 5993

Melrose D. B., Macquart J.-P., 1998, ApJ, 505, 921

Melrose D. B., 1992, in Hankins T. H., Rankin J. M., Gil J. A., eds, The Magnetospheric Structure and Emission Mechanisms of Radio Pulsars, IAU Colloquium 128. Pedagogical University Press, Zielona Góra, Poland, p. 306

Navarro J., Manchester R. N., Sandhu J. S., Kulkarni S. R., Bailes M., 1997, ApJ, 486, 1019

Navarro J., 1994, PhD thesis, California Institute of Technology

Papoulis A., 1965, Probability, Random Variables, and Stochastic Processes. McGraw-Hill, Sydney

Pavlov G. G., Zavlin V. E., 1997, ApJ, 490, L91

Penzias A. A., Wilson R. W., 1965, ApJ, 142, 419

Pound R. V., Rebka, Jr. G. A., 1960, Phys. Rev. Lett., 4, 337

Press W. H., Teukolsky S. A., Vetterling W. T., Flannery B. P., 1992, Numerical Recipes: The Art of Scientific Computing, 2^{nd} edition. Cambridge University Press, Cambridge

Radhakrishnan V., Cooke D. J., 1969, Astrophys. Lett., 3, 225

Rankin J. M., Rathnasree N., 1995, ApJ, 452, 814

Rankin J. M., 1983a, ApJ, 274, 333

Rankin J. M., 1983b, ApJ, 274, 359

Reitman I., 1984, Ghostbusters. Black Rhino, Columbia Pictures and Delphi Productions, New York

Reynolds J., 2001. *private communication*

Reynolds J., 2003, Parkes RadioTelescope Users Guide. Australia Telescope National Facility

Romani R. W., Taylor J. H., 1983, ApJ, 265, L35

Ruderman M. A., Sutherland P. G., 1975, ApJ, 196, 51

Ryba M. F., Taylor J. H., 1991, ApJ, 371, 739

Sandhu J. S., Bailes M., Manchester R. N., Navarro J., Kulkarni S. R., Anderson S. B., 1997, ApJ, 478, L95

Sazhin M. V., 1978, Sov. Astron., 22, 36

Shabanova T. V., Lyne A. G., Urama J. O., 2001, ApJ, 552, 321

Shapiro I., Pettengill G. H., Ash M. E., Stone M. L., Smith W. B., Ingalls R. P., Brockelman R. A., 1968, Phys. Rev. Lett., 20, 1265

Shapiro I. I., 1964, Phys. Rev. Lett., 13, 789

Shklovskii I. S., 1970, Sov. Astron., 13, 562

Shrauner J. A., 1997, PhD thesis, Princeton University

Smarr L. L., Blandford R., 1976, ApJ, 207, 574

Stairs I. H., Arzoumanian Z., Camilo F., Lyne A. G., Nice D. J., Taylor J. H., Thorsett S. E., Wolszczan A., 1998, ApJ, 505, 352

Stairs I. H., Splaver E. M., Thorsett S. E., Nice D. J., Taylor J. H., 2000, MNRAS, 314, 459, (astro-ph/9912272)

Stairs I. H., Lyne A. G., Shemar S. L., 2000, Nature, 406, 484

Stairs I. H., 1998, PhD thesis, Princeton University

Standish E. M., 1990, A&A, 233, 252

Stinebring D. R., Cordes J. M., 1983, Nature, 306, 349

Stinebring D. R., Cordes J. M., Rankin J. M., Weisberg J. M., Boriakoff V., 1984, ApJS, 55, 247

Stinebring D. R., Ryba M. F., Taylor J. H., Romani R. W., 1990, Phys. Rev. Lett., 65, 285

Sturrock P. A., 1971, ApJ, 164, 529

Taam R. E., van den Heuvel E. P. J., 1986, ApJ, 305, 235

Tauris T. M., Bailes M., 1996, A&A, 315

Taylor J. H., Cordes J. M., 1993, ApJ, 411, 674

Taylor J. H., Weisberg J. M., 1982, ApJ, 253, 908

Taylor J. H., Weisberg J. M., 1989, ApJ, 345, 434

Taylor J. H., 1991, Proc. I. E. E. E., 79, 1054

Taylor J. H., 1992, Philos. Trans. Roy. Soc. London A, 341, 117

Thorsett S. E., Chakrabarty D., 1999, ApJ, 512, 288

Thorsett S. E., Dewey R. J., 1996, Phys. Rev. D, 53, 3468

Thorsett S. E., Stinebring D. R., 1990, ApJ, 361, 644

Turlo Z., Forkert T., Sieber W., Wilson W., 1985, A&A, 142, 181

Vachaspati T., Vilenkin A., 1985, Phys. Rev. B, 31, 3052

van Straten W., Britton M., Bailes M., 2000, in Kramer M., Wex N., Wielebinski R., eds, Pulsar Astronomy - 2000 and Beyond, IAU Colloquium 177. Astronomical Society of the Pacific, San Francisco, p. 283

van Straten W., Bailes M., Britton M., Kulkarni S. R., Anderson S. B., Manchester R. N., Sarkissian J., 2001, Nature, 412, 158

Weisberg J. M., Taylor J. H., 2002, ApJ, 576, 942

Weisberg J. M., Romani R. W., Taylor J. H., 1989, ApJ, 347, 1030

Wietfeldt R., Straten W. V., Rizzo D. D., Bartel N., Cannon W., Novikov A., 1998, A&AS, 131, 549

Wolszczan A., Frail D. A., 1992, Nature, 355, 145

Wolszczan A., 1991, Nature, 350, 688

Xilouris K. M., Kramer M., Jessner A., von Hoensbroech A., Lorimer D., Wielebinski R., Wolszczan A., Camilo F., 1998, ApJ, 501, 286

Xilouris K. M., 1991, A&A, 248, 323

Young M. D., Manchester R. N., Johnston S., 1999, Nature, 400, 848

Zavlin V. E., Pavlov G. G., Sanwal D., Manchester R. N., Trümper J., Halpern J. P., Becker W., 2002, ApJ, 569, 894

Appendix A

Dynamic Range Requirements

When considering the dynamic range required in order to minimize distortions during analog-to-digital conversion, the parameter of interest is the instantaneous signal-to-noise ratio, $S/N_{\rm inst}$. As shown in Figure 5 of Jenet & Anderson (1998) and Figure 3 of Kouwenhoven & Voûte (2001), the response of a two-bit digitizer remains linear up to $S/N \sim 1$. When $S/N_{\rm inst}$ exceeds this limit, the resulting distortions to the pulsar signal will become greater than $\sim 1\%$. For a Nyquist-sampled, band-limited signal, $S/N_{\rm inst}$ may be derived from Equation 2.6 by substituting an integration length equal to the sampling interval, i.e. $t_{\rm obs} = 1/(2\Delta\nu)$. Therefore, for a dual-polarization receiver,

$$S/N_{\rm inst} = K \frac{S_{\rm inst}}{T_{\rm sys}}. \tag{A.1}$$

Here, $S_{\rm inst}$ is the instantaneous flux and the sensitivity, K, of the antenna may be estimated using Equation 2.7. For the Parkes 64 m dish, $A_0 = \pi r^2 \sim 3200\,{\rm m}^2$ and $\eta_A \sim 0.7$ (Reynolds 2003) yield $K \sim 0.8\,{\rm K\,Jy^{-1}}$. However, due to ohmic losses in the system, the value for the Multibeam receiver is closer to $0.67\,{\rm K\,Jy^{-1}}$ (Reynolds 2003).

At 20 cm, the mean pulse profile of PSR J0437−4715 peaks at approximately 5.6 Jy and the average S/N is about 0.16. However, single pulses have been observed with peak flux densities as high as ∼200 Jy (Jenet et al. 1998), corresponding to $S/N_{\rm inst} \sim 5.7$. Clearly, it is of interest to estimate the frequency with which the instantaneous flux of PSR J0437−4715 exceeds the acceptable limits for two-bit sampling.

In a 12.4 minute observation, Jenet et al. (1998) observe a distribution of pulse energies described by

$$\log_{10}(N) = a + bS_{\rm peak}, \tag{A.2}$$

where N is the number of pulses, $a = 4.51 \pm 0.01$, $b = -0.0262 \pm 0.0002\,{\rm Jy^{-1}}$, and $S_{\rm peak}$ is the peak flux density. The fractional number of pulses with flux density greater than S may be calculated from the integral,

$$f(S) = \frac{1}{N_{\rm tot}} \int_S^\infty N(s)\, ds = -\frac{A}{BN_{\rm tot}} \exp(BS) \tag{A.3}$$

where $A = 10^a$, $B = \ln(10)b$, and $N_{tot} \sim 1.29 \times 10^5$ is the total number of pulses observed.

Substituting $K \sim 0.67\,{\rm K\,Jy^{-1}}$, and $T_{\rm sys} \sim 23.5$K (Reynolds 2003) into Equation A.1, the instantaneous flux corresponding to $S/N_{\rm inst} \sim 1$ is $S_{\rm max} \sim 35\,$Jy. As the dispersion smearing in our 20 cm observations is approximately equal to the width of the main pulse peak ($\sim 140\,\mu$s), this value may in turn be substituted into Equation A.3 to estimate that approximately 50% of the observed pulses will have an instantaneous flux density exceeding the operating range of a two-bit digitizer. The deleterious effects of quantization on these pulses requires detailed study in future work.

Appendix B

Nomenclature

The following glossary defines the various mathematical symbols and acronyms used throughout the thesis. Boldface characters denote matrix quantities and boldface italicized characters denote vector quantities.

$\dot{x}$	First derivative of x with respect to time
$\ddot{x}$	Second derivative of x with respect to time
z^*	Complex conjugate of z
$\breve{x}$	Discreet, or digitized, form of analog process, x
$\otimes$	Direct product
$\langle x \rangle$	Expectation value of x, or time-average of $x(t)$
$\mathbf{E}^\dagger$	Hermitian transpose of $\mathbf{E}$, or $(\mathbf{E}^*)^{\mathrm{T}}$
$\mathbf{B}_{\hat{\boldsymbol{m}}}(\beta)$	Boost operator
$\mathbf{R}_{\hat{\boldsymbol{n}}}(\phi)$	Rotation operator
α	Right ascension
β	Quadratic Doppler shift
δ	Declination
μ_α	Proper motion in right ascension, $\mu_\alpha \equiv \dot{\alpha}\cos\delta$
μ_δ	Proper motion in declination, $\mu_\delta \equiv \dot{\delta}$
$\boldsymbol{\mu}$	Proper motion vector, $\boldsymbol{\mu} = (\mu_\alpha, \mu_\delta)$
μ	Composite proper motion, $\mu = \lvert\boldsymbol{\mu}\rvert$
ν	Frequency (typically radio, also pulsar spin)
ϕ_μ	Celestial position angle of proper motion vector
ψ	Position angle of linearly polarized radiation
π	Trigonometric Parallax
$\boldsymbol{\rho}$	Coherency matrix
σ	Noise level; standard deviation
σ_τ	Arrival time residual RMS
$\boldsymbol{\sigma}$	3-vector with components equal to the Pauli spin matrices
τ_{c}	Characteristic age ($\equiv P/2\dot{P}$)
ω	Orbital longitude of periastron

Ω	Orbital longitude of ascending node
a	Orbital semi-major axis
ACF	Auto-correlation function
b	Galactic latitude
BSBC	Binary system barycentre
c	Speed of light ($\sim 3.00 \times 10^8$ m s^{-1})
d_π	Parallax distance
d_β	Bell-Bailes distance
CPSR	Caltech Parkes Swinburne (Baseband) Recorder
DM	Dispersion measure
DSP	Digital signal processing
e	Orbital eccentricity
$f(M)$	Keplerian mass function
FFT	Fast Fourier Transform (algorithm)
FPTM	Fast Pulsar Timing Machine (Caltech autocorrelation spectrometer)
GR	General relativity
i	Orbital inclination angle
i	$\sqrt{-1}$
ISM	Interstellar medium
Jy	Unit: Jansky (electric spectral flux density: 10^{-26} W m^{-2} Hz^{-1})
l	Galactic longitude
lt s	Unit: Light seconds (distance; $c \times 1$ s)
$M_\odot$	Unit: Solar mass (mass; $\sim 1.99 \times 10^{30}$ kg)
m_c	Mass of pulsar companion
m_p	Mass of pulsar
MJD	Modified Julian Day (JD - 2,400,000.5)
MSP	Millisecond pulsar
$N_{\rm free}$	Number of degrees of freedom in a model fit
P	Pulse (spin) period
P_b	Orbital period
pc	Unit: parsec (distance; $\sim 3.09 \times 10^{16}$ m)
PSD	Power spectral density
PSR	Naming prefix for pulsars
RF	Radio frequency
RM	Rotation measure
RVM	Rotating vector model
S/N	Signal to noise ratio
SSBC	Solar system barycentre
T_0	Orbital epoch of periastron
TOA	(Pulse) Time Of Arrival
UHECR	Ultra high energy cosmic ray
VLBI	Very long baseline interferometry
x	Projected semi-major axis, $x \equiv a \sin i$

Publications

The following publications report on results derived from or supplemented by the work presented in this thesis.

Ord, S., Bailes, M. and van Straten, W. 2002, A neutral hydrogen distance limit to the relativistic binary PSR J1141-6545. *Mon. Not. R. Astr. Soc.*, **337**, 409–412

Kramer, M., Johnston, S., and van Straten, W. 2002, High-resolution single-pulse studies of the Vela pulsar. *Mon. Not. R. Astr. Soc.*, **334**, 523–532

van Straten, W. 2001, Radio astronomical polarimetry and phase-coherent matrix convolution. *Astrophys. J.*, **568**, 436–442

Edwards, R.T., van Straten, W. and Bailes, M. 2001, A search for submillisecond pulsars. *Astrophys. J.*, **560**, 365–370

van Straten, W., Bailes, M., Britton, M.C., Kulkarni, S.R., Anderson, S.B., Manchester, R.N. and Sarkissian, J. 2001, A test of general relativity from the three-dimensional orbital geometry of a binary pulsar. *Nature*, **412**, 158–160

Edwards, R.T., Bailes, M., van Straten, W. and Britton, M.C. 2001, The Swinburne intermediate-latitude pulsar survey. *Mon. Not. R. Astr. Soc.*, **326**, 358–374

Johnston, S., van Straten, W., Kramer, M. and Bailes, M. 2001, High time resolution observations of the Vela pulsar. *Astrophys. J.*, **549**, L101–L104

van Straten, W., Britton, M.C, Bailes, M., Anderson, S.B. and Kulkarni, S. 2000, Pulsar applications of the Caltech Parkes Swinburne baseband processing system. in *Pulsar Astronomy – 2000 and Beyond*, (eds. M. Kramer, N. Wex, and N. Wielebinski) IAU Colloq. 177, ASP Conference Series, **202**, 283–284

Britton, M.C., van Straten, W., Bailes, M., Toscano, M. and Manchester, R.N. 2000, High precision timing of PSR J0437-4715. in *Pulsar Astronomy – 2000 and Beyond*, (eds. M. Kramer, N. Wex, and N. Wielebinski) IAU Colloq. 177, ASP Conference Series, **202**, 73–74